



HAL
open science

Effective kinetics driven by dynamic concentration gradients under coupled transport and reaction

Charlotte Le Traon, Tomás Aquino, Camille Bouchez, Kate Maher, Tanguy Le Borgne

► **To cite this version:**

Charlotte Le Traon, Tomás Aquino, Camille Bouchez, Kate Maher, Tanguy Le Borgne. Effective kinetics driven by dynamic concentration gradients under coupled transport and reaction. *Geochimica et Cosmochimica Acta*, 2021, 306, pp.189-209. 10.1016/j.gca.2021.04.033 . insu-03225145

HAL Id: insu-03225145

<https://insu.hal.science/insu-03225145>

Submitted on 12 May 2021

HAL is a multi-disciplinary open access archive for the deposit and dissemination of scientific research documents, whether they are published or not. The documents may come from teaching and research institutions in France or abroad, or from public or private research centers.

L'archive ouverte pluridisciplinaire **HAL**, est destinée au dépôt et à la diffusion de documents scientifiques de niveau recherche, publiés ou non, émanant des établissements d'enseignement et de recherche français ou étrangers, des laboratoires publics ou privés.

Journal Pre-proofs

Effective kinetics driven by dynamic concentration gradients under coupled transport and reaction

Charlotte Le Traon, Tomás Aquino, Camille Bouchez, Kate Maher, Tanguy Le Borgne

PII: S0016-7037(21)00258-1
DOI: <https://doi.org/10.1016/j.gca.2021.04.033>
Reference: GCA 12179

To appear in: *Geochimica et Cosmochimica Acta*

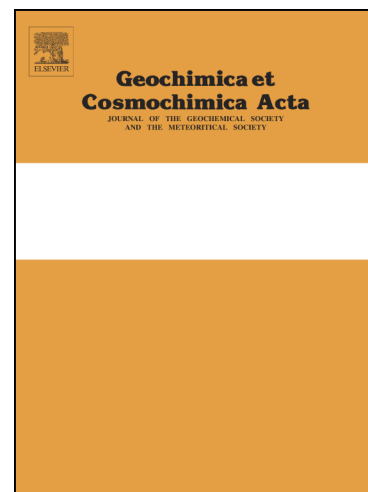
Received Date: 21 October 2020

Accepted Date: 26 April 2021

Please cite this article as: Traon, C.L., Aquino, T., Bouchez, C., Maher, K., Borgne, T.L., Effective kinetics driven by dynamic concentration gradients under coupled transport and reaction, *Geochimica et Cosmochimica Acta* (2021), doi: <https://doi.org/10.1016/j.gca.2021.04.033>

This is a PDF file of an article that has undergone enhancements after acceptance, such as the addition of a cover page and metadata, and formatting for readability, but it is not yet the definitive version of record. This version will undergo additional copyediting, typesetting and review before it is published in its final form, but we are providing this version to give early visibility of the article. Please note that, during the production process, errors may be discovered which could affect the content, and all legal disclaimers that apply to the journal pertain.

© 2021 Published by Elsevier Ltd.



Effective kinetics driven by dynamic concentration gradients under coupled transport and reaction

Charlotte Le Traon^{*1}, Tomás Aquino¹, Camille Bouchez¹, Kate Maher², and
Tanguy Le Borgne¹

¹Université de Rennes 1, CNRS, Géosciences Rennes UMR 6118, 35042 Rennes, France

²Department of Geological and Environmental Sciences, Braun Hall #118, 450 Serra Mall, Stanford University,
Stanford, CA, 94305, USA

March 31, 2021

Abstract

Biogeochemical reaction kinetics are generally established from batch reactors where concentrations are uniform. In natural systems, many biogeochemical processes are characterized by spatially and temporally variable concentration gradients that often occur at scales which are not resolved by field measurements or biogeochemical and reactive transport models. Yet, it is not clear how these sub-scale chemical gradients affect reaction kinetics compared to batch kinetics. Here we investigate this question by studying the paradigmatic case of localized pulses of solute reacting with a solid or a dissolved species in excess. We consider non-linear biogeochemical reactions, representative of mineral dissolution, adsorption and redox reactions, which we quantify using simplified power-law kinetics. The combined effect of diffusion and reaction leads to effective kinetics that differ quantitatively and qualitatively from the batch kinetics. Depending on the nonlinearity (reaction order) of the local kinetics, these effects lead to either enhancement or decrease of the overall reaction rate, and result in a rich variety of reaction dynamics. We derive analytical results for the effective kinetics, which are validated by comparison to direct numerical simulations for a broad range of Damköhler numbers and reaction order. Our findings provide new insights into the interpretation of imperfectly mixed lab experiments, the effective kinetics of field systems characterized by intermittent reactant release and the integration of sub-scale concentration gradients in reactive transport models.

1 Introduction

The kinetics of biogeochemical reactions are used to predict a range of processes, including the weathering of rock, the transport and degradation of contaminants, and the nutrient cycling that sustains subsurface microbial life. Given the importance of transport processes in governing the removal and supply of products and reactants and the necessity to consider a variety of spatial and temporal scales, reactive transport models are increasingly used to predict processes occurring in the subsurface (e.g., see reviews by Van Cappellen and Gaillard, 2018; Steefel et al., 2005; Li et al., 2017; Maher and Navarre-Sitchler, 2019; Maher and Mayer, 2019). A host of other studies rely

^{*}Corresponding author: charlotte.letraon@univ-rennes1.fr

36 on conceptual frameworks that integrate reactive transport principles, with applications ranging
37 from interpretation of global elemental cycles (Lasaga et al., 1994), to catchment elemental fluxes
38 over synoptic (e.g. Kirchner and Neal, 2013) or geologic timescales (e.g. Maher and Chamberlain,
39 2014), to nutrient cycling at microsites (e.g. Keiluweit et al., 2016). In all cases, biogeochemical
40 kinetics have to be represented at an appropriate temporal and spatial scale. However, kinetic
41 models are generally derived from well-mixed batch experiments in the lab. Yet, reaction kinetics
42 can differ by orders of magnitude from homogeneous batch reactors to heterogeneous field systems
43 (White and Brantley, 2003; Meile and Tuncay, 2006; Maher et al., 2006; Navarre-Sitchler and
44 Brantley, 2007; Li et al., 2008; Salehikhoo et al., 2013; Wen and Li, 2017a; Wen and Li, 2018;
45 Wang et al., 2018). Different hypotheses have been investigated to explain these discrepancies.
46 These include diffusion limitations or geometrical constraints at the pore scale that reduce access
47 of solutes to reactive surfaces compared to fully mixed systems (Molins et al., 2012; Molins et
48 al., 2014; Beckingham et al., 2016; Soulaine et al., 2017; Beckingham et al., 2017; Deng et al.,
49 2018), physical heterogeneity that induces spatially heterogeneous solute fluxes and modifies the
50 effective reactive surfaces (Atchley et al., 2013; Wen and Li, 2017a; Wen and Li, 2018; Jung and
51 Navarre-Sitchler, 2018a; Jung and Navarre-Sitchler, 2018b; Wang et al., 2018) and geochemical
52 heterogeneity, where averaging can also lead to scale effects in effective reaction kinetics (Atchley
53 et al., 2014; Salehikhoo et al., 2013). These studies highlight the role of delayed or heterogeneous
54 access to reactive surfaces at different scales. A complementary question that has received less
55 attention is: what is the impact of heterogeneous and time evolving concentration landscapes on
56 reaction kinetics, when access to reactive surfaces or to other dissolved reactants is not limited?

57 Concentration gradients are created by spatially heterogeneous or transient release of solutes.
58 They can be sustained by stretching induced by flow, whether at pore scale (Heyman et al., 2020)
59 or at Darcy scale (Le Borgne et al., 2017), and are ultimately destroyed by diffusion. In the case
60 of linear kinetics, heterogeneity in concentration fields does not impact the effective kinetics when
61 access to reactive surfaces or other reactants is not limited. However, for non-linear kinetics that
62 imply the local reaction rate is a non-linear function of local solute concentrations, the average
63 reaction rate over a non-homogeneous concentration field is expected to differ from the local
64 kinetics (Battiato et al., 2009; Battiato and Tartakovsky, 2011; Hubert et al., 2020). Such non-
65 linear reaction kinetics play a central role in a broad range of biogeochemical reactions, including
66 dissolution, redox and sorption reactions (Serrano, 2001; Serrano, 2003; Guo et al., 2015). Yet,
67 it is not known how different types of non-linear kinetics may lead to either enhanced or reduced
68 effective kinetics when considering heterogeneous solute plumes.

69 Many physical, climatic, and biological processes result in localized and intermittent release
70 of solutes that generate temporally and spatially variable concentration fields in subsurface en-
71 vironments (Fig. 1). Rain events (Fig. 1.a) leach soil and induce pulses of dissolved chemical
72 compounds into groundwater (Murphy et al., 2018). River stage variations (Fig. 1.b) induce
73 pulses of oxygen-rich water in hyporheic zones and the underlying groundwater systems, lead-
74 ing to chemical disequilibrium and the degradation, fixation or release of contaminants, such as
75 organic carbon, nitrate or arsenic (Datta et al., 2009; Malzone et al., 2016; Trauth and Fleck-
76 enstein, 2017; Bandopadhyay et al., 2018). Biological activity in general (Fig. 1.c), can induce
77 pulses of chemical compounds (e.g. Hinsinger et al., 2003). For instance, roots release dissolved
78 gases and other compounds through daily cycles of respiration and exudation, and via associated
79 fungal and microbial organisms (e.g. Li et al., 2017). Finally engineered injections (Fig. 1.d)
80 create chemical disequilibrium and trigger a range of reactive pulses. This includes managed
81 aquifer recharge (Magesan et al., 1998; Urióstegui et al., 2016; Al-Yamani et al., 2019), which
82 is often performed by periodically wetting and drying the system (Dutta et al., 2015), lead-
83 ing to biogeochemical reactions such as ammonium-nitrogen reduction and pathogen removal
84 (Abel et al., 2014). Injection of concentrated carbon dioxide into the deep subsurface results

85 in density-driven instabilities, leading to localized high concentrations of reactive CO₂-rich fluid
 86 (Szulczewski et al., 2012). Collectively, reactive pulses play an important role in a broad range of
 87 engineered injections, including soil and groundwater remediation (Kitanidis and McCarty, 2012;
 88 Rolle and Le Borgne, 2019), seasonal energy storage, through heat, hydrogen or underground
 89 pumped storage hydroelectricity (Panfilov, 2010; Pujades et al., 2017; Hermans et al., 2018),
 90 geothermal dipoles (Burté et al., 2019), and injection and storage of water used for fracking
 operations (Llewellyn et al., 2015).

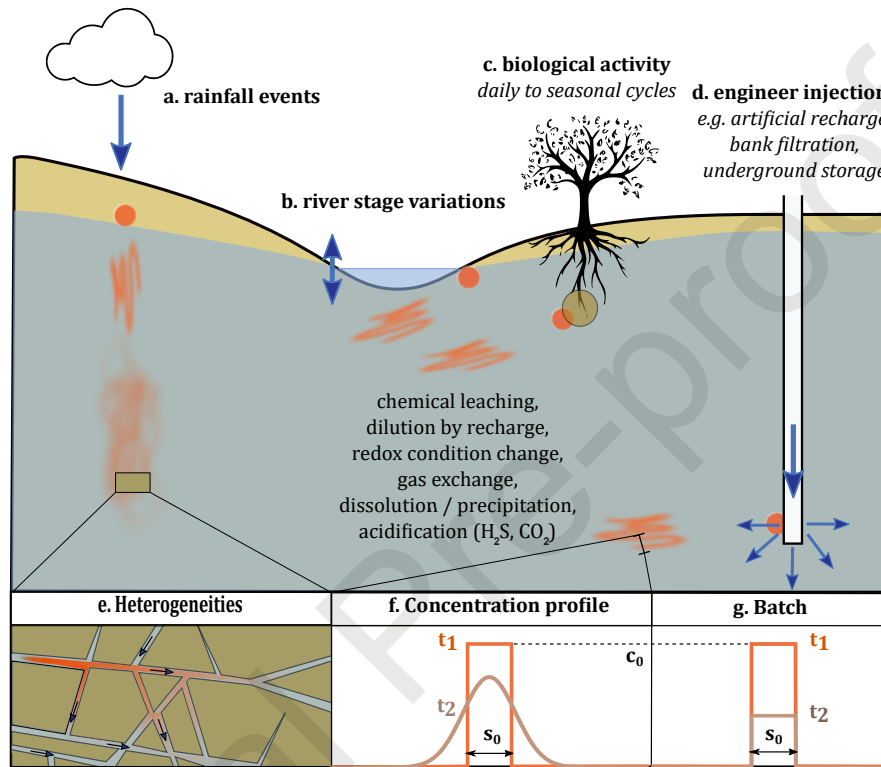


Figure 1: Conceptual representation of biogeochemical pulses in the subsurface. When released, pulses are concentrated and localized (orange dots). As they are transported in the subsurface, they are stretched by velocity gradients and form elongated lamella structures (Le Borgne et al., 2015). Solute concentrations are driven by dilution, which occurs by diffusion along the concentration gradients, and reactions either with minerals or other dissolved solutes. The arrows indicate an injection or an exchange of solute. Four types of processes generating reactive pulses are highlighted: a. soil leaching by rain, b. surface water – groundwater exchanges, c. biological activity (the brown circle represents the root zone), and d. engineered injections. In all these applications, chemical gradients can be enhanced and sustained by physical heterogeneities, as illustrated in inset e. The inset f. illustrates the considered simplified one-dimensional concentration profile that evolve under the action of diffusion and reaction. The effective kinetics of such reactive pulses are compared to batch kinetics that evolve through reaction alone under uniform concentrations (inset g.).

91 Because chemical gradients are enhanced and sustained by physical heterogeneities (Le Borgne
 92 et al., 2013; Heyman et al., 2020) (see inset of Fig. 1), they develop over a range of scales that
 93 cannot be fully resolved by field sampling approaches that average solute (e.g., screened ground-
 94 water wells) or reactive transport models. Hence, effective kinetic models that capture the effect
 95

96 of sub-scale concentration gradients are required. Macrodispersion theory, where the dispersive
97 flux is assumed to be proportional to the concentration gradient, tends to strongly underes-
98 timate concentration gradients, leading to significant errors when used in reactive transport
99 models (Gramling et al., 2002; Dentz et al., 2011a). Non-Fickian dispersion theories have suc-
100 cessfully described the asymmetry of solute plumes resulting from trapping in low velocity areas
101 (Berkowitz et al., 2006). However, this framework aims at describing spatial dispersion of solute
102 plumes and does not quantify subscale concentration gradients governed by mixing (Dentz et al.,
103 2011b). Recent mixing theories have provided a new framework to predict the full distribution
104 of concentrations and concentration gradients both at pore scale (Heyman et al., 2020) and at
105 Darcy scale (Le Borgne et al., 2013). In this framework, solute plumes are represented as en-
106 sembles of elongated lamellar structures, i.e. solute filaments elongated in one direction and
107 compressed in the other. The latter develop systematically in heterogeneous media both at the
108 pore (De Anna et al., 2014b) and Darcy (Le Borgne et al., 2014) scale. This is due to velocity
109 gradients at different scales that deform solute plumes into such filaments, whose formation and
110 merging controls mixing rates (Le Borgne et al., 2015). At the scale of a solute lamella, the effect
111 of stretching on the enhancement of concentration gradients and mixing is quantified explicitly
112 by a change of variable that leads to one-dimensional equation formally identical to a diffusion
113 equation in the direction perpendicular to the lamella (Villermaux, 2019). The full distribution
114 of concentration is then predicted from the distribution of stretching rates. While this framework
115 has been successfully used to model mixing-limited reactions (De Anna et al., 2014a; Rolle and
116 Le Borgne, 2019), its coupling with other types of reactions, such as solid-fluid reactions is an
117 outstanding challenge. The key difficulty for this is to first solve analytically the coupling of
118 diffusion transverse to solute lamella with non-linear kinetic laws.

119 Here we use analytical solutions and numerical simulations to establish the effective kinetic
120 laws that result from coupled diffusion and non-linear reactions in spatially and temporally
121 variable concentration gradients. We consider pulses of solute that react either with a homo-
122 geneously distributed solid phase or fluid phase, both in excess with respect to the transported
123 solute. Hence, there is no limitation of access to reactive surfaces or other reactants, which allow
124 use to isolate and formalize the coupling between non-homogeneous concentration distributions
125 and non-linear kinetics. Dilution of solute concentration by mixing with the background fluid
126 transfers high concentrations towards lower concentrations (Kitanidis, 1994), which may either
127 reduce or enhance the average kinetics, depending on the reaction order of the local kinetics.
128 Although mixing plays an important role in this problem, it does not act to bring reactants
129 into contact as extensively studied in the context of mixing-induced reactions, where reactions
130 are limited by the mixing of spatially segregated reactants (see recent reviews of Rolle and Le
131 Borgne, 2019; Valocchi et al., 2019). Instead, we study how changes in concentration distribu-
132 tions by mixing may lead to the emergence of effective kinetics that differ from local kinetics.
133 In complex multi-component reactions, this effect acts together with a range of other processes
134 and therefore it is difficult to understand and quantify. Therefore, although we have studied
135 a simplified reaction in order to isolate a particular phenomenon, our results are expected to
136 be relevant to a large range of geochemical systems, where this effect acts together with other
137 known mechanisms, including spatial segregation of reactants either in fluid or in solid phases.
138 In section 2, we present the reactive transport problem. In section 2.5, we define the studied
139 effective quantities. In section 3, we present the numerical and analytical results for a range
140 of Damköhler numbers and non-linear kinetics. In the section 4, we discuss the implications of
141 our findings for different types of reaction, including mineral dissolution, redox reactions and
142 sorption.

2 Reactive transport problem

2.1 Reaction kinetics

We study the reaction of a mobile aqueous species, with concentration c , which reacts with other aqueous species or with a solid surface. The latter are assumed to be in excess and homogeneously distributed, so that the reaction kinetics $r(c)$ only depends on the concentration c through the non-linear rate law:

$$r(c) = kc^\beta, \quad (1)$$

where $\beta > 0$ is the effective order of the reaction and k is the reaction rate constant, which integrates the effect of other species in excess (units $[\text{mol}^{1-\beta} L^{d(\beta-1)} T^{-1}]$, where d is the spatial dimension).

In a well-mixed batch reactor, the concentration c is homogeneous in space and depends only on time (see lower right inset of Fig. 1). The concentration decreases everywhere according to the reaction rate (1), so that the kinetic rate law describing the evolution of the mean concentration \bar{c} as a function of time t is given by

$$\frac{d}{dt}\bar{c} = -r(\bar{c}), \quad (2)$$

with $\bar{c} = M/V$, where M is the mass of reactant and V is the volume of the batch reactor.

Although it is simplified, the system isolates the effect of transient concentration gradients on upscaled kinetics. The characterization of this basic yet non-trivial system may thus guide the understanding of more complex biogeochemical systems, where this effect is coupled to other mechanisms, such as heterogeneous reactive surfaces, spatial segregation of multiple elements and mixing limitations. As discussed in section 4, it is relevant for mineral dissolution far-from-equilibrium (Hellmann and Tisserand, 2006; Maher, 2011; Guo et al., 2015), for non-linear sorption kinetics (Weber J. et al., 1991; Perry et al., 1997; Serrano, 2003) and for homogeneous redox reactions where β depends on the stoichiometric coefficients (Bethke, 1996; Bleam, 2017). We focus on $\beta \neq 1$, because dilution by mixing has no effect on linear reactions in the sense that the upscaled kinetics are the same as the local kinetics in this case. Indeed, for the linear reaction, $\beta = 1$, mass decay over time is independent of the spatial concentration distribution.

2.2 Reactive pulses

We wish to compare the batch dynamics Eq. (2), to the dynamics of the average concentration under diffusive transport for the same local reaction. Thus, we consider the reactant to be described by a non-homogeneous concentration $c(x, t)$ depending on both position x and time t (see lower middle inset of Fig.1). We assume that the concentration is independent of the other spatial coordinates y and z over a reference surface S . This assumption is taken here for simplicity of analytical derivations, and can be relaxed to consider three dimensional transport processes following the same approach. The concentration is thus assumed to obey the diffusion-reaction equation,

$$\frac{\partial c}{\partial t} - D \frac{\partial^2 c}{\partial x^2} = -r(c), \quad (3)$$

where $D[L^2T^{-1}]$ is the diffusion coefficient, which we assume to be constant. The initial condition is taken as a rectangular pulse identical to the batch conditions, but the pulse is allowed to diffuse in an infinite one-dimensional domain. At the boundaries, concentration tends to zero. Note that, in natural systems, boundaries limiting diffusive mass transfer would ultimately lead to a homogenization of the domain and a convergence to the batch reaction rates. Our results hence

182 describe the transient regimes before this happens. For a reference scale L larger than the pulse
 183 characteristic size, $L \gg \sqrt{Dt}$, the mean concentration is,

$$\bar{c} = \frac{M}{LS}. \quad (4)$$

184 The temporal evolution of the mean concentration is obtained by integrating Eq. (3) over space,

$$\frac{d}{dt}\bar{c}(t) = -\frac{k}{L} \int_{-L/2}^{L/2} dx c(x,t)^\beta. \quad (5)$$

185 Note that only the reaction term contributes directly to the change in mass, which can be shown
 186 by integration by parts. However, transport affects the shape of the concentration profile, and
 187 thus indirectly impacts the total mass and the average concentration. This one-dimensional
 188 diffusion-reaction approach is also relevant to understand the effect of plume stretching on reac-
 189 tion kinetics in heterogeneous media. Indeed, solutes transported in the subsurface tend to follow
 190 elongated lamella structures (Le Borgne et al., 2015) where concentrations vary weakly along the
 191 stretching direction and concentration gradients develop mostly in one-dimension transverse to
 192 lamellae (Fig. 1).

193 2.3 Non-dimensional units

194 In order to meaningfully compare the dynamics for different conditions, it is convenient to define
 195 non-dimensional quantities in terms of values characterizing the different physical processes at
 196 play. We define the non-dimensional position as $x_* = x/w_0$, where w_0 is the initial pulse width,
 197 the non-dimensional concentration as $c_* = c/c_0$, where c_0 is the initial concentration, and the
 198 non-dimensional average concentration as $\bar{c}_* = \bar{c}L/(c_0w_0)$. Note that the non-dimensional initial
 199 concentration and average concentration are thus $c_*(0) = \bar{c}_*(0) = 1$. Furthermore, we define
 200 non-dimensional time as t/τ_R , where

$$\tau_R = \frac{1}{kc_0^{\beta-1}} \quad (6)$$

201 is the characteristic reaction time (inverse rate) associated with the initial concentration c_0 .
 202 In the following, we drop the asterisk for notational brevity. All quantities discussed are non-
 203 dimensional in the sense discussed here unless mentioned.

204 In non-dimensional units, the kinetic equation for the batch is,

$$\frac{dc}{dt} = -c^\beta, \quad (7)$$

205 which can be solved with the initial condition $c(0) = 1$ to yield,

$$c(t) = [1 + (\beta - 1)t]^{-\frac{1}{\beta-1}}. \quad (8)$$

206 This solution holds whenever $\beta \neq 1$, that is, for nonlinear reactions. The special case of linear
 207 reactions leads to the classical $c(t) = e^{-t}$ exponential decay.

208 In order to account for the effect of dilution by mixing, we identify the time needed to
 209 homogenize the width of the initial condition as

$$\tau_D = \frac{w_0^2}{2D}, \quad (9)$$

210 corresponding to the time to homogenize a unit distance in nondimensional coordinates. The
 211 relative importance of reaction with respect to dilution is characterized by the dimensionless
 212 Damköhler number

$$\text{Da} = \tau_D / \tau_R. \quad (10)$$

213 Fast reactions relative to dilution correspond to $\text{Da} > 1$, while slow reactions correspond to
 214 $\text{Da} < 1$. In nondimensional terms, the diffusion-reaction equation becomes

$$\frac{\partial c}{\partial t} - \frac{1}{2\text{Da}} \frac{\partial^2 c}{\partial x^2} = -c^\beta. \quad (11)$$

215 Note that, in nondimensional variables, the initial condition is a rectangular pulse of unit width.
 216 The dimensionless total mass obeys

$$\frac{d}{dt} \bar{c}(t) = -\frac{1}{L} \int_{-L/2}^{L/2} dx c(x, t)^\beta. \quad (12)$$

217 All introduced parameters and their units are given in table 3 (Appendix A).

218 2.4 Numerical analysis

219 To explore the different effective reaction regimes, we first solved Eq. (11) numerically using Mat-
 220 lab's *pdepe* method, a numerical solver for one-dimensional partial differential equations (Skeel
 221 and Berzins, 1990). We use Neumann boundary conditions, i.e. no flux boundary condition, and
 222 a rectangular pulse of unit normalized width as initial condition (Fig. 1f). The domain size is
 223 chosen large enough to maintain close to zero concentrations at the domain boundaries at the end
 224 of the simulation, and the grid discretization is refined to ensure the convergence of the solver.
 225 To analyze the effective kinetics at the pulse scale, that is for averaged concentrations over the
 226 solute pulse, we study the time evolution of the average concentration $\bar{c}(t)$ and the evolution of
 227 the effective reaction rate as a function of the average concentration.

228 We compare these numerical simulations to analytical solutions that we derived using the ap-
 229 proximation discussed in the following section. Furthermore, we test these analytical predictions
 230 for one geochemically relevant example using the multi-component reactive transport model,
 231 CrunchFlow (version 1.0). Boundary and initial conditions for these simulations are described in
 232 the corresponding section. As for Matlab simulations, we use a domain large enough to ensure
 233 that the pulse does not reach the boundary and a grid discretization small enough to ensure
 234 convergence of the results.

235 2.5 Gaussian approximation for analytical derivations

236 When reactions are described by nonlinear local kinetics, transport and reaction interact in com-
 237 plex ways. Reaction impacts local concentration gradients, which in turn affect diffusive fluxes.
 238 The latter leads to changes in the spatial concentration profile, which affects reaction. These
 239 interactions are captured by the diffusion-reaction equation (11). In order to better understand
 240 the interplay between reaction dynamics and dilution, and how it leads to different average ki-
 241 netics compared to a well-mixed batch reactor, we develop an approximate analytical description
 242 of the average concentration, for a range of Damköhler numbers Da and reaction orders β .

243 In non-dimensional units, the initial condition is a rectangular pulse of unit finite width,
 244 identical with the batch conditions. Before diffusion has time to deform the pulse substantially,
 245 which is the case for times much smaller than the characteristic diffusion time τ_D , we expect

246 the dynamics to be well-approximated by the batch kinetics, so that the average concentration
 247 approximately follows Eq. (8). This corresponds to $t \ll \text{Da}$ in nondimensional terms. For
 248 non-dimensional times $t \gtrsim \text{Da}$, diffusion has appreciably deformed the initial pulse. To derive
 249 analytical solutions for this problem, we approximate the reactive solute profiles as Gaussian
 250 distributions. This approximation is expected to be highly accurate for low Da when diffusion is
 251 faster at modifying the concentration distribution than reaction. It turns out to be also accurate
 252 in intermediate and high Da ranges (Appendix C), which facilitates an analytical solutions for
 253 the effective kinetics. The concentration distribution of reactive pulses is thus approximated as,

$$c(x, t) = \frac{M(t)}{\sqrt{2\pi\sigma^2(t)}} e^{-\frac{x^2}{2\sigma^2(t)}}, \quad (13)$$

254 where the variance $\sigma^2(t)$ and mass $M(t)$ evolve in time as a function of diffusion and reaction.
 255 Note that in the absence of reaction, the solution corresponds to $M(t) = 1$, and $\sigma^2(t) \propto t/\text{Da}$.

256 Inserting Eq. (13) into Eq. (12), we obtain,

$$\frac{d}{dt} M(t) = -\frac{M(t)^\beta}{\sqrt{\beta}} [2\pi\sigma^2(t)]^{\frac{1-\beta}{2}}. \quad (14)$$

257 The Gaussian assumption allows second spatial derivatives in Eq. (11) to be estimated as,

$$\frac{\partial^2 c}{\partial x^2} = \left(-\frac{1}{\sigma^2} + \frac{x^2}{\sigma^4}\right) c, \quad (15)$$

258 hence, at $x = 0$, we have for the maximum concentration,

$$c(0, t) = \frac{M(t)}{\sqrt{2\pi\sigma^2(t)}}, \quad (16)$$

259 and for the second spatial derivative,

$$\frac{\partial^2 c}{\partial x^2} \Big|_{x=0} = -\frac{M(t)}{\sqrt{2\pi}\sigma(t)^3}. \quad (17)$$

260 Inserting Eq. (16) and (17) in Eq. (11) at $x = 0$, we obtain

$$\frac{d}{dt} \frac{M(t)}{\sqrt{2\pi\sigma^2(t)}} = -\frac{M(t)}{2\text{Da}\sqrt{2\pi}\sigma(t)^3} - \frac{M(t)^\beta}{(2\pi)^{\beta/2}\sigma(t)^\beta}. \quad (18)$$

261 As discussed in Appendix B, Eq. (14) and (18) provide two independent equations to solve for
 262 the two unknowns $M(t)$ and $\sigma(t)$. Since the average concentration is proportional to the total
 263 mass (equation (4)), the dimensionless average concentration is equal to the dimensionless mass,
 264 $\overline{c(t)} = M(t)$. The accuracy of the Gaussian approximation is discussed in Appendix C.

265 3 Results

266 First, numerical simulations for the average concentration as a function of time for different
 267 values of β are presented for broad range of Damköhler numbers and reaction orders in order
 268 to demonstrate the resulting behavior and departure of the effective kinetics from the batch
 269 systems. As expected, for $\beta = 1$, the effective kinetics are equal to the batch kinetics (Fig. 2.b).
 270 For the other cases, the results can be generalized as:

- 271 • For $\beta < 1$, the average concentration of the pulse decreases faster than in the batch reactor,
 272 and the effective reaction rate of the pulse system is globally greater than the batch reactor
 273 (Fig. 2a).
- 274 • For $\beta > 1$, the average concentration of the pulse decreases more slowly than in the batch reactor
 275 and the effective reaction rate of the pulse injected system is globally less than the
 276 batch reactor (Fig. 2c-d).

277 Qualitatively, this effect may be understood as follows. For $\beta < 1$, the reaction is more efficient
 278 when distributing a given mass in the low concentration range because of the form of the kinetics
 279 (Eq. (1)). Dilution by diffusion accelerates the transfer of mass towards lower concentration
 280 values and thus enhances the average kinetics compared to the batch case. As a result, the time
 281 at which the average concentration goes to zero (Fig. 2.a) decreases with decreasing Da as dilution
 282 accelerates the effective kinetics. The opposite effect occurs for $\beta > 1$, leading to a reduction of
 283 the effective kinetics compared to batch kinetics. For the extreme case of $\beta > 3$, dilution retards
 284 the reaction to such a level that the average concentration converges asymptotically to a nonzero
 285 value (Fig. 2.d), with the asymptotic residual concentration increasing with decreasing Da .

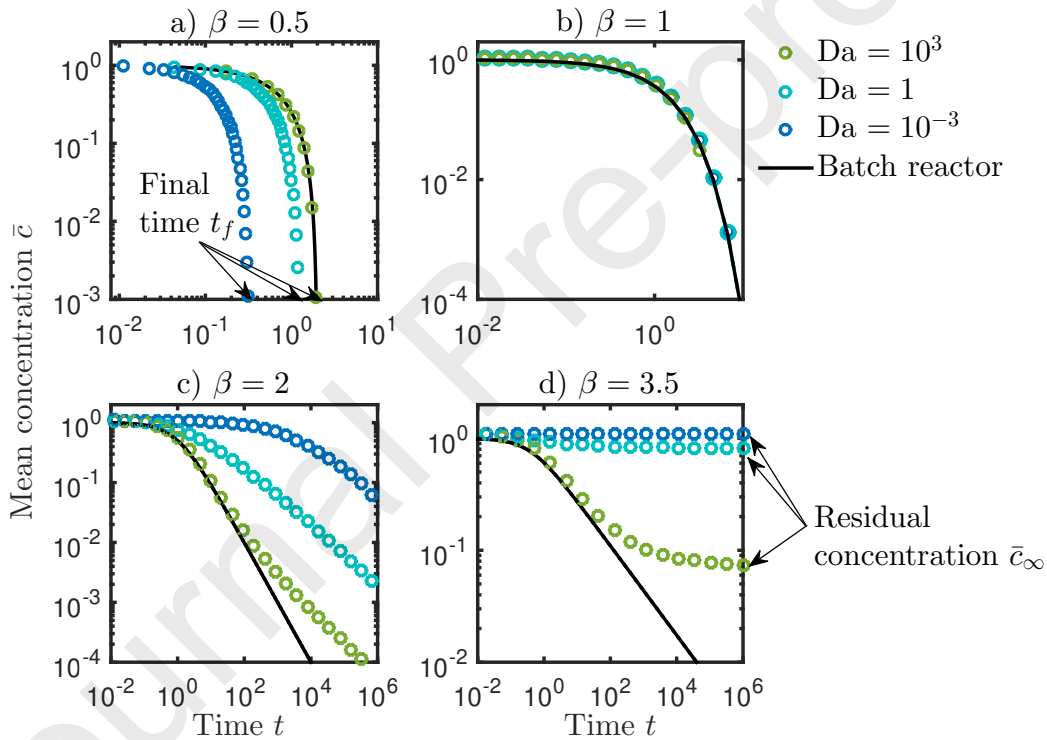


Figure 2: Average concentration in a reactive pulse as a function of time for a) $\beta = 0.5$, b) $\beta = 1$, c) $\beta = 2$ and d) $\beta = 3.5$. Numerical simulations for low, intermediate and high Da numbers (circles) are compared to batch kinetics (black solid line). The final time for full reactant consumption t_f , which occurs for $\beta < 1$, is indicated with arrows in figure a). The residual average concentration \bar{c}_∞ , which occurs for $\beta > 3$, is indicated with arrows in figure d). Note that the y-axis differs between panels to resolve the differences in concentration evolution.

286 The impact of dilution on reaction kinetics may be also understood by plotting the total
 287 reaction rate as a function of the average concentration (Fig. 3). For linear kinetics, the effective

288 kinetics are identical to the batch kinetics independent of Da (Fig. 3.b). For low Da and $\beta < 1$,
 289 the global reaction rates are always greater than the batch for a given average concentration
 290 (Fig. 3.a). For low Da and $\beta > 1$, the global reaction rates are always less than the batch for
 291 a given average concentration (Fig. 3.c and Fig. 3.d). The difference between effective reaction
 292 kinetics and batch kinetics can reach several orders of magnitude. At low Damköhler numbers
 293 (Blue dots in Fig. 3) and quasi-constant average concentration, the variation in the reaction rates
 294 is substantial (an increase for $\beta < 1$ and a decrease for $\beta > 1$). This counterintuitive regime
 295 is due to the action of diffusion, which distributes mass towards low concentration values, such
 296 that while the total reaction rate varies, the overall rate is insufficient to affect the total mass.
 297 At high Damköhler numbers (Green dots in Fig. 4) the effective rate first follows a batch-like
 298 behavior and then departs towards effective kinetics that are a function on β . In the following,
 299 we present our analytical results for the effective kinetics as a function of β .

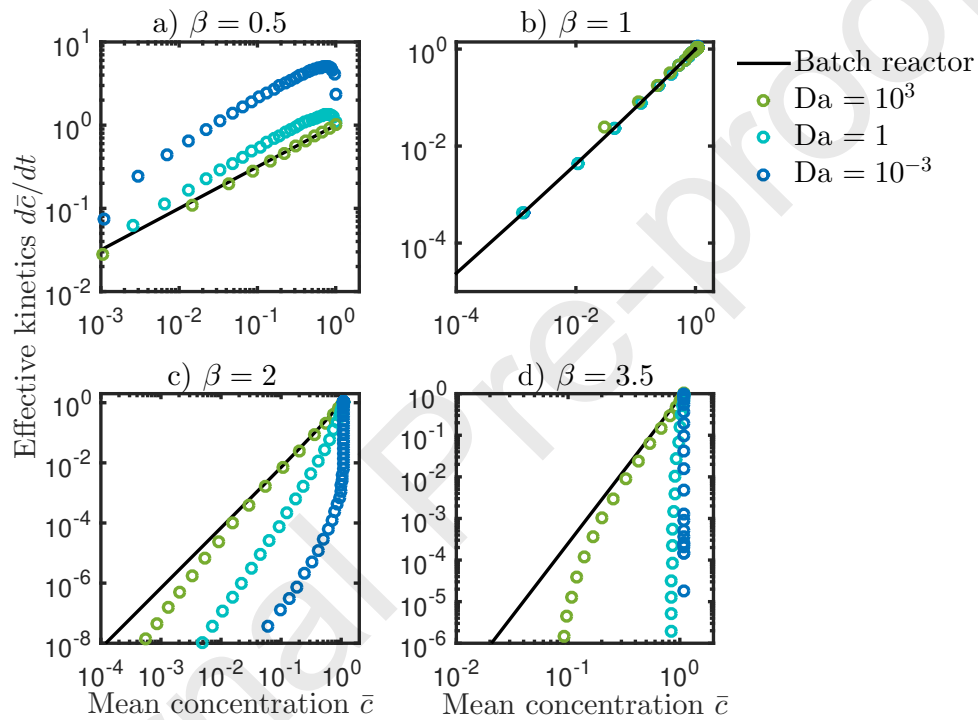


Figure 3: Effective kinetics of reactive pulses quantified as the rate of change of the mean concentration as a function of mean concentration for a) $\beta = 0.5$, b) $\beta = 1$, c) $\beta = 2$ and d) $\beta = 3.5$. Numerical simulations for low, intermediate and high Da numbers (circles) are compared to the batch reactor solution (black solid line). Note that the y-axis differs between panels to resolve the differences in concentration evolution.

300 3.1 Reaction order $\beta < 1$

301 For $\beta < 1$, the average concentration reaches zero at a finite time t_f (Fig. 4.a). For large
 302 Damköhler numbers, diffusion does not have time to induce significant dilution before $t = t_f$.
 303 Therefore, this time is identical to the time required to consume the full reactant mass in batch

304 reactions (Green dots and line in Fig. 4.a, Appendix B.2.1):

$$t_f = \frac{1}{1 - \beta}, \text{ for } Da > 1. \quad (19)$$

305 For low Damköhler numbers, using the assumption of a Gaussian concentration distribution, we
 306 obtain a solution for the evolution of the average concentration (Appendix B.1, Eq. (B.2)), in
 307 good agreement with numerical simulations (Blue dots and dashed lines in Fig. 4.a). This leads
 308 to the following estimate of t_f (Appendix B.1, Eq. (B.4)),

$$t_f \sim Da^{\frac{1-\beta}{3-\beta}}, \text{ for } Da < 1. \quad (20)$$

309 This scaling and the convergence to a constant value given by Eq. (19) at large Da are verified
 310 from numerical simulations in Fig. 4.b. The effect of dilution is thus to accelerate the effective
 311 kinetics, with a consumption time up to ten times less than predicted from the batch kinetics
 312 for $Da = 10^{-3}$.

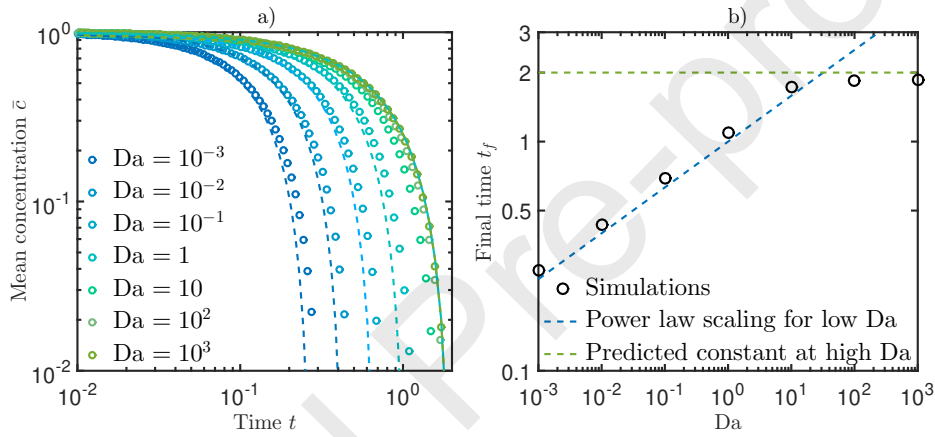


Figure 4: Effect of Damköhler on effective kinetics for $\beta = 0.5$, a) Average concentration as a function of time for several Damköhler numbers. Numerical results (dots) are compared to the analytical solutions of Eq. (B.2) (dashed lines). The batch solution is shown as a continuous line. b) Time t_f at which the mean concentration reaches zero as a function of Damköhler number. Black circles represents simulations, dashed lines represents the analytical predictions of Eq. (19) for low Damköhler numbers and Eq. (20) for high Damköhler number.

313 3.2 Reaction order $1 < \beta < 3$

314 For $1 < \beta < 3$, we predict that the departure from the batch kinetics is not only a difference in
 315 the magnitude of the reaction but also in its order. The latter is shown by the power law scaling
 316 that relates the average reaction rate to the average concentration (dashed lines in Fig. 5),
 317 with an exponent that differs from the batch reaction order. For low Damköhler numbers, our
 318 solution implies that the average concentration decays in time as a power law (Appendix B.1,
 319 Eq. (B.6)),

$$\bar{c}(t) \sim t^{-\frac{3-\beta}{2(\beta-1)}}, \quad (21)$$

320 and the effective rate r_M follows (Appendix B.1, Eq. (B.9))

$$\frac{d\bar{c}}{dt} \sim \bar{c}^{\tilde{\beta}}, \quad (22)$$

321 with the effective reaction order $\tilde{\beta}$,

$$\tilde{\beta} = \frac{1 + \beta}{3 - \beta}. \quad (23)$$

322 For high Damköhler numbers, two regimes occur (Fig. 8). The first regime, for $t < Da$, follows
 323 the batch kinetics (Appendix B.2.1). In the second regime, for $t > Da$, (Appendix B.2.2), the
 324 effective kinetics follow the same power law behavior as for low Damköhler number (Fig. 5.a)
 325 defined by Eq. (22).

326 These predictions are consistent with numerical simulations for all Damköhler numbers (Fig. 5.a)
 327 and all local reaction order β (Fig. 5.b). For low to intermediate Damköhler numbers, the ef-
 328 fective kinetics follow the predicted power law kinetics, characterized by the effective reaction
 329 order $\tilde{\beta}$ for the full range of concentrations (Fig. 5.b). For large Damköhler numbers (green dots
 330 in Fig. 5.a) the effective kinetic shows two regimes: a first regime following the batch kinetics
 331 given by Eq. (1) and a second power law regime given by Eq. (22). The difference between the
 332 effective and local reaction orders is largest for large reaction orders (Fig. 6). For $\beta = 1.5$, the
 333 effective order $\tilde{\beta} = 1.7$ is relatively close to the batch reaction order. Above $\beta = 1.5$, the effective
 334 order increases rapidly and is equal to $\tilde{\beta} = 3$ for $\beta = 2$. As β tends to 3, the deviation between
 335 the effective reaction order and the batch reaction order can become very large as the effective
 336 reaction order tends to infinity (Fig. 6).

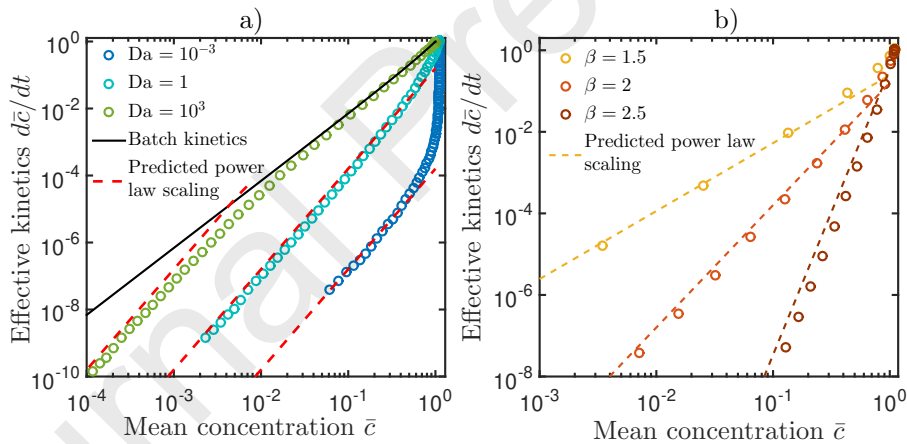


Figure 5: Effective kinetics in terms of mean concentration, a) $\beta = 2$, for Low, intermediate and high Da numbers, b) $Da = 1$ for different β in the range $1 < \beta < 3$. Numerical results (dots) are compared to analytical solutions (dashed lines). The power law behavior predicted by Eq. (22) is shown as a dashed line.

337 3.3 Reaction order $\beta \geq 3$

338 For $\beta \geq 3$, the pulse reaction is much less efficient compared to a batch reactor, in the sense that
 339 the average reaction rate is smaller than in batch conditions for a given average concentration.

340 For $\beta > 3$, dilution slows down the reaction so that the average concentration does not reach zero

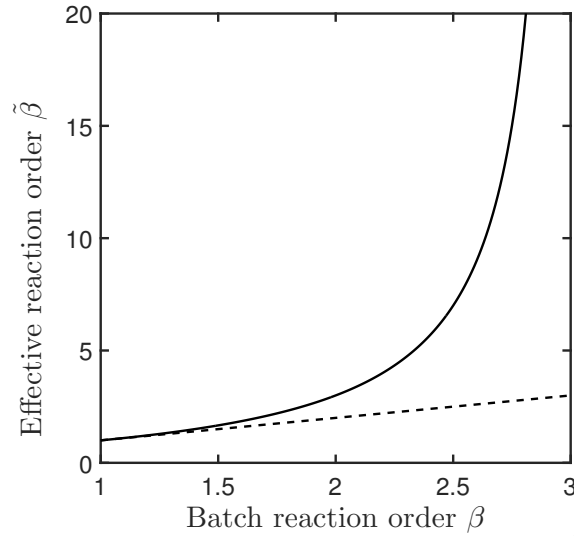


Figure 6: Effective reaction order $\tilde{\beta}$ predicted by Eq. (23) as a function of the batch reaction order for $1 < \beta < 3$ (solid line). The dashed line represents $\tilde{\beta} = \beta$.

341 but converges to an asymptotic minimum value \bar{c}_∞ (Fig. 7). For $\beta = 3$, the average concentration
 342 decays to zero logarithmically as $t \rightarrow \infty$ (Appendix B.1, Eq. (B.3)). Note that this behavior
 343 differs fundamentally from the lower reaction orders discussed above, for which the reaction rate
 is always larger than zero and there is no residual concentration, except for $Da = 0$.

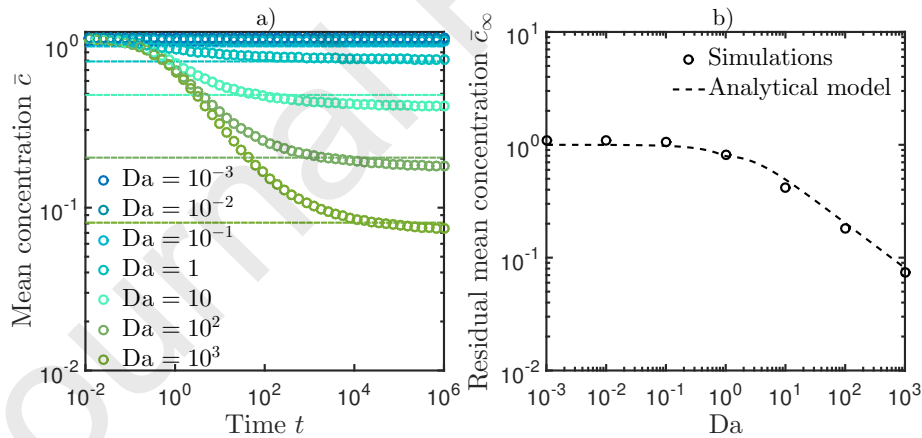


Figure 7: Effect of Damköhler on effective kinetics for $\beta = 3.5$, a) Numerical simulations (circles) as a function of time for different Damköhler number. Analytical model predictions for the asymptotic residual concentration are shown as dashed lines. b) Asymptotic residual mean concentration as a function of Damköhler number. Black circles represents simulations, the dashed black line represents the analytical model corresponding to Eq. (B.5) in Appendix B for low Damköhler numbers and to Eq. (25) for high Damköhler numbers.

344

345 For low Damköhler numbers, the solution for the evolution of the mean concentration (Ap-
 346 pendix B.1, Eq. (B.2)) leads for $\beta > 3$ to an asymptotic value \bar{c}_∞ such that (Eq. (B.5))

$$1 - \bar{c}_\infty \sim \text{Da}. \quad (24)$$

347 As Da tends to zero, the asymptotic residual mean concentration tends to one (Fig. 7), which
 348 highlights the inhibiting effect of dilution on mass evolution for $\beta > 3$.

349 For high Damköhler numbers, the asymptotic residual mean concentration occurs in the
 350 second regime, leading to an asymptotic minimum value (Appendix B.2.2, Eq. (B.21))

$$\bar{c}_\infty \sim \text{Da}^{-\frac{1}{\beta-1}}, \quad (25)$$

351 which again quantifies the inhibiting effect of dilution on reaction as Da increases. These ana-
 352 lytical results closely match numerical simulations (Fig. 7.b).

353 4 Discussion

354 Our findings demonstrate that chemical gradients alter effective reactive kinetics through the
 355 coupling of diffusion and nonlinear reactions. By investigating the evolution of reactive solute
 356 pulses, as a paradigm for chemical gradients that evolve over space and time, we have uncovered
 357 a diverse spectrum of effective kinetic dynamics that depend on (1) the reaction nonlinearity
 358 (reaction order β) and (2) the relative importance of reaction and dilution quantified by the
 359 Damköhler number Da. A central conclusion of our study is that dynamic chemical gradients
 360 not only change the magnitude of the effective kinetic coefficient but also change the nature of the
 361 non-linearity compared to the local kinetics. This result is in contrast with previous studies that
 362 have studied how diffusive limitation, physical and geochemical heterogeneities (e.g. Soulaïne
 363 et al., 2017; Wen and Li, 2017b; Deng et al., 2018), alter the effective kinetic coefficients, while
 364 keeping the same effective kinetic laws as the local kinetics. While we have focused on simplified
 365 reaction kinetics to quantify and formalize this mechanism, these dynamics are expected to
 366 impact a large range of geochemical systems where they are coupled to other processes. In the
 367 following, we discuss the relevance to common classes of biogeochemical reactions based on a
 368 synthesis of the results discussed above. Subsequently, we provide an example for a mineral
 369 dissolution reactions where rate discrepancies are commonly observed. However, the approach
 370 is also applicable to other types of reactions, including redox, precipitation, complexation and
 371 adsorption reactions, as discussed in the following section.

372 4.1 Characteristic persistence time of reactive pulses

373 To illustrate the consequences of the derived effective kinetics across a broad range of β and Da,
 374 we calculate the persistence time of reactive pulses that quantifies a characteristic time for the
 375 decay of the pulse mass under the effect of reaction. We define this time as a the time required
 376 for the pulse mass to reach a given fraction of the initial mass. To compare with the batch
 377 reactor, we divide it by the time it would take for a batch reactor to reach the same fraction of
 378 the initial mass. This normalized persistence time t_c is shown in Fig. 8 as a function of β and
 379 Da. We have taken here the fraction of the initial mass to calculate this time to be equal to 1%.
 380 Qualitatively similar results are obtained for other fractions. We have considered the full range
 381 of Damköhler numbers, from $\text{Da} = 10^{-3}$ (fast dilution compared to reaction) to $\text{Da} = 10^3$ (fast
 382 reaction compared to dilution). This covers a range of characteristic reaction times, that vary
 383 broadly depending on the type of reaction, and of transport time scales, which depend on the
 384 pulse size and species diffusion coefficient (Eq. (9)).

385 On the left-hand side of Fig. 8, for $\beta < 1$, reactants disappear on the order of ten times
 386 faster than in the batch in the low Damköhler range, which is consistent with the analytical
 387 estimate of t_f (Fig. 4). For $1 < \beta < 3$, the characteristic persistence time increases sharply
 388 with the non-linear reaction order β , reaching several orders of magnitude increase. This is
 389 due to the emergence of effective reaction orders $\tilde{\beta}$ that become much larger than the batch
 390 reaction order for increasing β (Fig. 6). Within the grey zone, for $\beta > 3$, residual mass persists
 391 indefinitely and the characteristic persistence time tends to infinity. Collectively, these findings
 392 imply that when concentration fields are heterogeneous the commonly used approach of coupling
 393 residence time to batch kinetics may underestimate/overestimate the persistence of reactants by
 394 orders of magnitude. Our main analytical findings in the different quadrants of Fig. 8 provide
 395 a framework for assessing the impact of concentration gradients on effective kinetics for a given
 396 type of reaction, as discussed below.

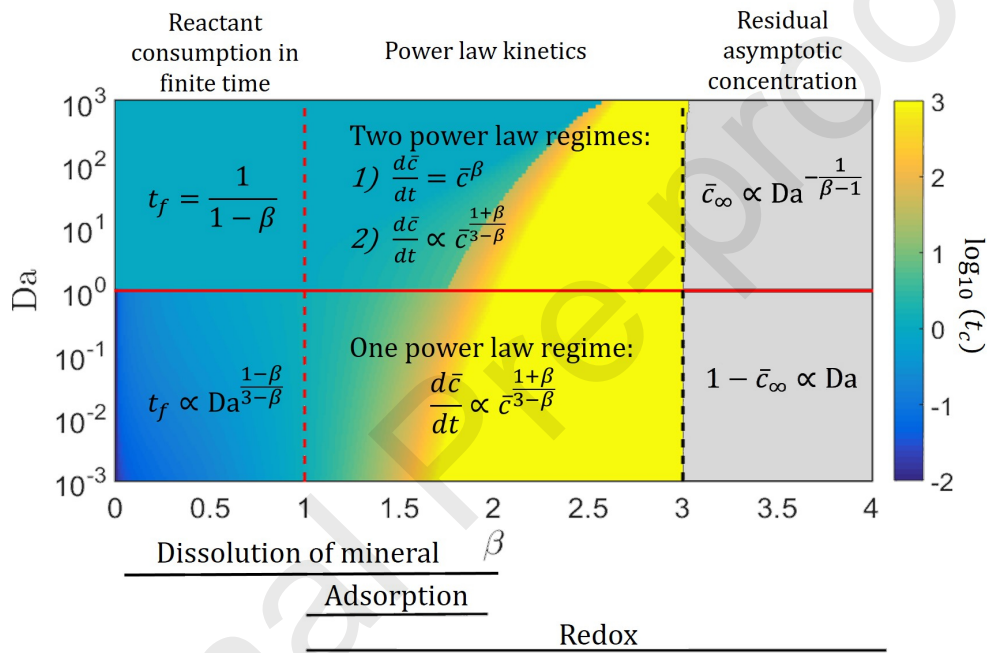


Figure 8: (Da , β) phase diagram of characteristic persistence time t_c and synthesis of main analytical results. The solid red line represents $Da = 1$. The dashed red and black lines correspond respectively to $\beta = 1$ and $\beta = 3$. The color scale represents the time t_c needed for the mean concentration to reach 1% of initial mean concentration for the reactive pulses, normalized by the same time for the batch reactor. The main reaction enhancement occurs for $\beta < 1$ and $Da < 1$ (blue area) while the effective reaction rate is strongly slowed down for $\beta > 1.5$ (yellow area). For $\beta > 3$, residual mass persists indefinitely and the characteristic persistence time may never be reached if the residual mass is larger than 1% (grey area). The typical range of effective reaction orders β for mineral dissolution, adsorption and redox reactions are indicated at the bottom.

397 4.2 Geochemical relevance of effective kinetics

398 Our results are strictly valid when the concentration of one element is spatially variable and
 399 the others are in excess in the fluid or in the mineral phase. This simplification isolates and

400 formalizes the impact of transient concentration gradients on upscaled kinetics. In complex
 401 multi-component reactive system, this effect will act together with other known mechanisms,
 402 such as geochemical and physical heterogeneities, as well as multiple reactions. Although other
 403 processes will also contribute to the effective kinetics, we argue that the new phenomena described
 404 here will likely have a major contribution as it can alter reaction rates over orders of magnitude
 405 and modify the effective orders of reaction. For single step reactions, the reaction order β with
 406 respect to a given chemical species is equal to its stoichiometric coefficient. However, most
 407 biogeochemical reactions are complex multi-step reactions such that the rate-limiting step is
 408 unknown and hence most reaction orders are determined empirically and may range from 0 to 5.

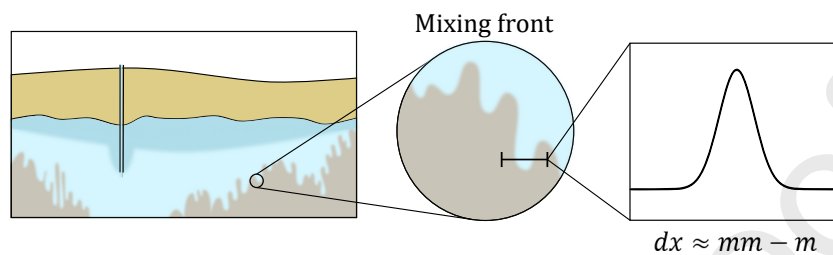
409 The lower left hand side of Fig. 8 would be typical of silicate mineral dissolution where
 410 reactions involve multiple steps that can be effectively described by an adaptation of transition
 411 state theory (Aagaard and Helgeson, 1982; Lasaga et al., 1994; Steefel and Lasaga, 1994):

$$r = k \prod_{i=1}^N a_i^n \left(1 - \frac{Q}{K_{eq}} \right)^m, \quad (26)$$

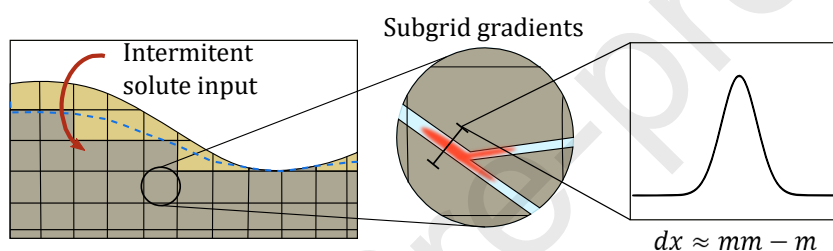
412 where r is the overall rate, k is the intrinsic kinetic constant, a_i the ion activity, N the number
 413 of species, Q the ion activity product for the mineral-water reaction, and K_{eq} the corresponding
 414 equilibrium constant. The empirical exponents n and m introduce a non-linearity of the reaction
 415 rate with respect to the species concentration (Hellmann and Tisserand, 2006). Far from equilib-
 416 rium, $Q \gg K_{eq}$ or $Q \ll K_{eq}$, and when a single species is limiting, equation (26) can be written as
 417 the simplified non-linear kinetics that we consider (equation (1)), with $\beta = n$. Effective reaction
 418 orders estimated from laboratory experiments and typically range from $\beta = 0.1$ to 2 (Plummer
 419 and Wigley, 1976; Palandri and Kharaka, 2004). Such mineral dissolution reactions are typically
 420 slow and therefore correspond to the low Da range. The upper right-hand sider region of Fig. 8
 421 may be typical of redox reactios. Metal redox reactions are typically characterized by $1 \leq \beta \leq 4$,
 422 while other redox reactions tend to have lower orders $1 \leq \beta \leq 2$ (Bethke, 1996). Redox reactions
 423 involving organic matter may have orders as high as $\beta = 5$ (Bleam, 2017). In the middle region
 424 of Fig. 8, where t_c transitions rapidly, adsorption kinetics may be particularly susceptible to
 425 the effects observed here. Adsorption reaction kinetics are generally modelled with first-order
 426 or pseudo-second-order kinetics (Rudzinski and Plazinski, 2006; Wu et al., 2009; Robati, 2013;
 427 Moussout et al., 2018), which correspond to $\beta = 1$ or $\beta = 2$, but higher reaction orders are also
 428 observed (Largitte and Pasquier, 2016).

429 The first application of our findings is for understanding the behavior of reactive solutes in
 430 field systems (Fig. 9a). As illustrated in Fig. 1, concentration gradients in natural systems can
 431 be driven by a diverse set of processes, ranging from intermittent sources to physical hetero-
 432 geneity. For a given transport time, the reaction efficiency may be much faster (for $\beta < 1$) and
 433 much slower (for $\beta > 1$) than anticipated from batch kinetics (Fig. 8). This could lead to a
 434 much deeper penetration of reactive pulses or to a much faster consumption of solutes. A sec-
 435 ond application is reactive transport modelling; to capture the effect of concentration gradients
 436 on reaction kinetics, reactive transport models should have a spatial resolution finer than the
 437 smallest scale of concentration gradients (Fig. 9b). This is not possible for catchment scale appli-
 438 cations (e.g. Li et al., 2017) but it is also challenging for modeling column experiments because
 439 chemical gradients often persist at the microscale (Heyman et al., 2020). Hence, our findings
 440 may help defining effective kinetics that quantify the impact of subscale gradients in reactive
 441 transport models. A third application is the interpretation of biogeochemical kinetics measured
 442 in experimental systems that are not well mixed, i.e. where chemical gradients persist (Fig. 9c).
 443 Geochemical reactions occurring at high temperatures and pressures, such as those associated
 444 with geologic carbon storage (e.g. DePaolo and Cole, 2013; Jun et al., 2013; Beckingham et al.,

a. Effective kinetics in field systems



b. Reactive transport modelling



c. Interpreting experimental kinetics

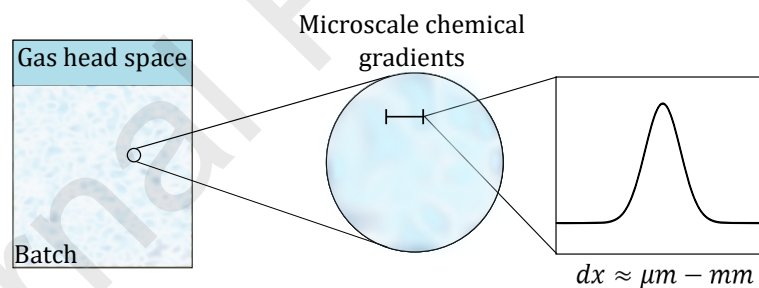


Figure 9: Illustration of different applications where unresolved chemical gradients may alter effective kinetics. a. Effective kinetics in field systems, such as CO₂ injection in the subsurface, where reactive pulses develop in mixing fronts. b. Reactive transport modeling, where subgrid chemical gradients cannot be resolved in models. c. Interpreting experimental kinetics in unmixed batches, where microscale chemical gradients can affect measured kinetics. The typical scales of expected chemical gradients for these applications is indicated as dx . Update the order of subfigures to match new order of section 5.

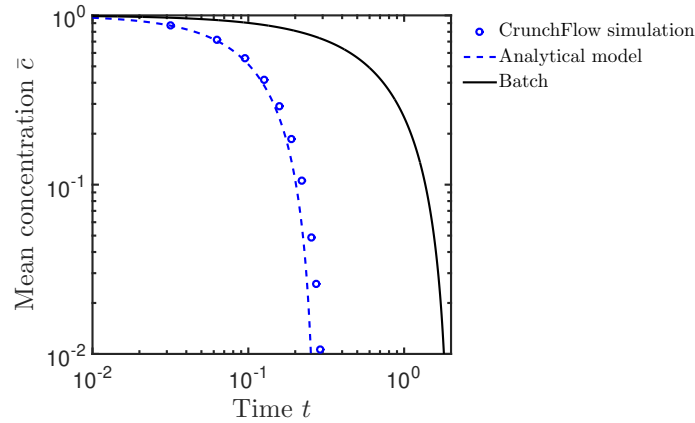
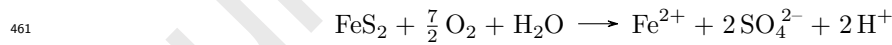


Figure 10: Simulation of pyrite dissolution by a pulse of dissolved oxygen for $Da = 10^{-3}$ ($\beta = 0.5$). Normalized mean concentration is shown as a function of normalized time, following the same definition as above. Results of the CrunchFlow simulation are shown as dots, the analytical model as a dashed line (Eq. B.2) and the batch model as a continuous line (Eq. B.11).

2016; Beckingham et al., 2017), are often studied using batch reactors, where a gas headspace of a constant volume is used to maintain a constant pressure (Giammar et al., 2005; Johnson et al., 2014). Depending on the experimental conditions, pressure vessels can be difficult to mix via rocking or internal stirring, and are often static. Hence, in the absence of mechanical mixing, chemical gradients of different origin may develop, including dissolved gas convection, transport limitations and spatially heterogeneous reaction rates.

4.3 Example of the oxidation of pyrite by a pulse of dissolved oxygen

To illustrate these effective kinetics for a specific geochemical system, we take the example of pyrite dissolution by a pulse of dissolved oxygen. The aqueous oxidation of pyrite by oxygen is an example of geochemical process studied with reactive transport models to address a range of problems, including aquifer storage and recovery (Lazareva et al., 2015), acid mine drainage (Hubbard et al., 2009), and radioactive waste migration (Malmström et al., 2000; Yang et al., 2007). Intermittent release of dissolved oxygen, due to rainfall events or river stage variations (Fig. 1.a and 1.b), or flow heterogeneities (Fig. 1.e) often lead to small-scale dissolved oxygen gradients (Xu et al., 2000; Bochet et al., 2020) that are typically not resolved by reactive transport models. The reaction of oxidation of pyrite by oxygen can be written as,



Assuming that the other species are in excess, the kinetic rate law for pyrite oxidation by oxygen may be written with respect to oxygen as (McKibben and Barnes, 1986)

$$\frac{1}{3.5} \frac{dc_{\text{O}_2}}{dt} \approx -kc_{\text{O}_2}^{0.5}, \quad (27)$$

corresponding to $\beta = 0.5$.

For the geochemical system considered here, the kinetics of subscale unresolved oxygen pulses would be faster than predicted by batch kinetics (Fig. 8). For instance, assuming a Damköhler number of 10^{-4} , resulting from a kinetic rate constant of 6.6×10^{-9} mol/m²/s (Yang et al., 2007) and a diffusion coefficient of 10^{-9} mol/m²/s (Jung and Navarre-Sitchler, 2018a), dissolved

Table 1: Initial and injection chemistry used in CrunchFlow simulations for a single pulse, pyrite dissolution

Species	Initial condition (mol/L)	Injection condition (mol/L)
Fe ²⁺	10 ⁻⁸	10 ⁻⁸
H ⁺	10 ⁻⁴	10 ⁻⁴
O _{2, aq}	10 ⁻¹¹	10 ⁻⁴
SO ₄ ²⁻	10 ⁻⁸	10 ⁻⁸
Cl ⁻	Equilibrates charge	Equilibrates charge

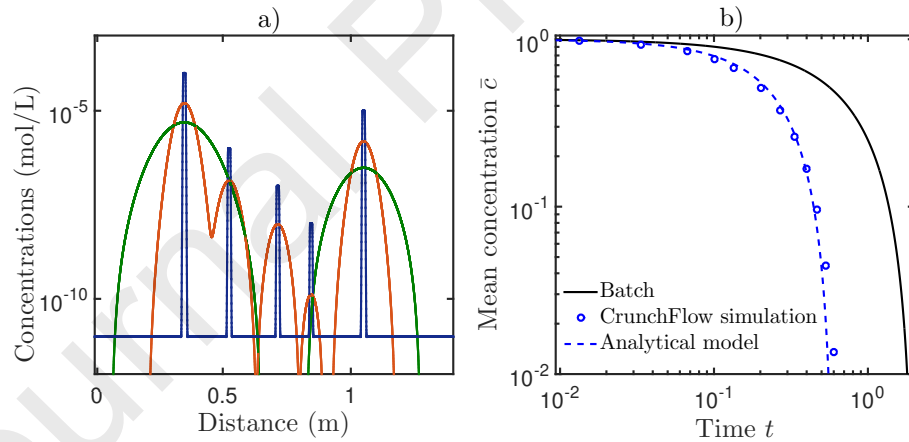
469 oxygen would be consumed 10 times faster than it would be in the well-mixed homogeneous
 470 system. The more rapid release of both Fe²⁺ and trace metals typically associated with pyrite
 471 (i.e., As, Pb, etc.) may have further implications for water quality. Although our results imply
 472 that kinetic rates used in reactive transport models of systems with sub-grid scale concentrations
 473 will be subject to additional uncertainty, our approach provides a concrete means of evaluating
 474 the range of kinetic parameters to enable robust sensitivity analysis or uncertainty quantification
 475 (e.g. Fenwick et al., 2014; Song et al., 2015).

476 We have verified that this geochemical system can be accurately modeled by our framework
 477 under the considered assumptions (Fig. 10) using the multi-component reactive transport model
 478 CrunchFlow (Steeffel et al., 2015). We first consider the case of a single pulse. The system is
 479 composed of pyrite with a porosity of 30% and dissolution kinetic constant $k = 10^{-8.31} \text{ m mol}^{-1}$
 480 s^{-1} (Yang et al., 2007). The considered solute species are O_{2, aq}, Fe²⁺, SO₄²⁻, and H⁺. For the
 481 initial condition in the domain prior to injection, the species concentrations are $c_{\text{O}_2} = 10^{-11}$
 482 mol/L, $c_{\text{Fe}^{2+}} = 10^{-8}$ mol/L, $c_{\text{SO}_4^{2-}} = 10^{-8}$ mol/L, and pH is 4. Chloride is designated as the
 483 charge balancing ion to maintain electroneutrality. In the injected pulse, concentrations are the
 484 same as in the domain except for the oxygen concentration is set as $c_0 = 10^{-4}$ mol/L (Bochet
 485 et al., 2020, Table 1). The simulations were performed at 25°C with a diffusion coefficient of 10⁻⁷
 486 m² s⁻¹ (Elberling et al., 1994), leading to Da = 10⁻³ (Table 2). The CrunchFlow simulation is
 487 in good agreement with the analytical model (Fig. 10). As predicted, the average concentration
 488 reaches zero much faster than the batch.

489 In order to evaluate the effect of a non-ideal concentration profile, we performed a CrunchFlow
 490 simulation with five irregularly spaced pulse injections of width 10⁻² m each, with different initial
 491 oxygen concentrations ($\log(c_{\text{O}_2}) = -4, -5, -6, -7, -8$) (Table 2). The initial conditions
 492 are the same as in the single pulse case (Table 1) and all the injected concentrations except
 493 oxygen are the same as in the background domain. The equivalent batch is defined with initial
 494 concentration equal to the mean of the pulse initial concentrations. The parameters are adapted
 495 to the single-pulse analytical model with an equivalent pulse width equal to the sum of the
 496 pulse widths, and an equivalent initial concentration set as the mean of injection concentrations,
 497 resulting in Da = 5 10⁻² (Table 2). In this case, the match with the analytical prediction remains
 498 excellent (Fig. 11) even though the concentration distribution is more complex than assumed in
 499 the analytical derivations.

Table 2: Parameters of the analytical model for the pyrite dissolution case.

Parameter	w_0	D	c_0	ν	k	A	Φ	τ_D	τ_R	Da
Unit	m	m ² /s	mol/L	[-]	[unit]	m ² /m ³	[-]	[-]	[-]	[-]
Single pulse $\beta = 0.5$	10^{-2}	10^{-7} ^a	10^{-4} ^b	3.5	$4.8 \cdot 10^{-9}$ ^c	350	0.3	$1.6 \cdot 10^{-5}$	$1.6 \cdot 10^{-2}$	10^{-3}
Several pulses $\beta = 0.5$	10^{-2}	10^{-7}	10^{-4} 10^{-5} 10^{-6} 10^{-7} 10^{-8}	3.5	$4.8 \cdot 10^{-9}$	350	0.3	$4 \cdot 10^{-4}$	$7.5 \cdot 10^{-3}$	$5 \cdot 10^{-2}$

^a(Elberling et al., 1994)^b(Bochet et al., 2020)^c(Yang et al., 2007)**Figure 11:** Simulation of pyrite dissolution by multiple pulses of dissolved oxygen ($\beta = 0.5$). Five pulses with different initial concentrations and irregularly spaced are injected in the domain. a) is the concentration profile in space at normalized time $t \approx 10^{-5}$ (blue), $t \approx 10^{-2}$ (orange), $t \approx 10^{-1}$ (green). b) the normalized mean concentration as a function of normalized time for the CrunchFlow simulation (dots), an equivalent batch system (with initial concentration equal to the mean of injected concentrations Eq. (B.11), continuous line), and an equivalent analytical model (considering one pulse with initial concentration equal to the mean of injected concentrations, Eq. (B.2), dashed line), thus corresponding to $Da = 5 \cdot 10^{-2}$.

5 Conclusions

The effective kinetics of reactive pulses reveal a rich diversity of behaviors driven by the interplay between dilution and non-linear reaction (Fig. 8). In the presence of concentration gradients, diffusion acts to redistribute mass towards lower concentrations, which, when coupled with non-linear reactions, can either enhance or inhibit the reaction efficiency depending on the local reaction order. We have derived approximate analytical solutions that capture these reactive dynamics and predict the different effective kinetic laws as a function of Damköhler number and the reaction order, which are representative of a range of reactive transport systems (Fig. 1, 8 and 9). An important consequence of our results is the emergence of new effective kinetic laws characterized by upscaled orders that can be very different from those of the local kinetics. The coupling of transient concentration gradients and non-linear reactions hence leads to effective kinetics that can be much more non-linear than the batch kinetics (Fig. 6).

To isolate this mechanism and derive approximate analytical solutions for the effective kinetics, we considered here the idealized case of reactive pulses evolving through diffusion and reaction. In complex natural reaction networks, this effect acts together with a range of other processes and therefore it is difficult to understand and quantify. Other important phenomenon known to impact the effective kinetics include the limited access of solutes to reactive surfaces and mixing limitations, due to physical and geochemical heterogeneity at the pore or Darcy scale (Molins et al., 2014; Beckingham et al., 2017; Wen and Li, 2018; Jung and Navarre-Sitchler, 2018a; Valocchi et al., 2019). In multi-components systems, our results are strictly valid when one element is varying in space and time and the others are in excess. In natural systems several elements may be spatially variable and react with different orders leading to more complex behaviour. However, since the effect that we have uncovered leads to orders of magnitude differences between batch and effective reaction rates, it is likely playing a major, and so far unappreciated, role in multi-component systems.

Although we explicitly solve the system for the ideal case of pulses, our general findings are expected to apply qualitatively to different types of concentration landscapes. Indeed, in the presence of concentration inhomogeneities, induced by intermittent reactant release or physical heterogeneity (Fig. 1), diffusion tends to redistribute mass towards lower concentrations, which leads to reaction enhancement or inhibition depending on the local reaction order β as described here. The derived analytical framework is an essential step to integrate a range of biogeochemical reactions in new mixing theories that describe the statistics of concentration gradients (Le Borgne et al., 2017). The lamella mixing theory was successfully used to predict the upscaled kinetics of mixing-driven reactions at pore scale (De Anna et al., 2014b) and Darcy scale (Le Borgne et al., 2014; Bandopadhyay et al., 2018) by coupling the one-dimensional compression-diffusion equation transverse to stretched solute lamellae with bi-molecular reactions in the fluid phase. By solving explicitly the coupling of diffusion and non-linear reactions, the method presented here resolves the main difficulty for the development of a reactive lamella framework to upscale the effective kinetics of a range of non-linear reactions under incomplete mixing conditions, including fluid-solid reactions.

These findings would thus be useful to interpret the result of reactive experiments in which subscale chemical gradients develop due to poor mixing. These analytical results may also be used to guide reactive transport models that cannot fully resolve the scale of concentration gradients, which occurs in many reactive transport problems. Finally, they provide a new framework to understand the effect of concentration gradients on chemical reactions in field applications, in particular to understand the possible longer/smaller persistent time or penetration length of reactive solutes. These findings indeed suggest that the characteristic persistence time of biogeochemical pulses can differ by orders of magnitude from the predictions of models that

548 couple solute residence time with batch kinetics. Reactive pulses are consumed much faster
 549 when the order of the reaction is less than one, whereas they persist for a much longer time
 550 when the order of the reaction is larger than one. These effects are particularly important at
 551 low Damköhler number i.e., for reactions that are slow compared to the characteristic diffusion
 552 time. For orders of reaction larger than three, dilution slows down reaction to the point that a
 553 residual mass persists asymptotically.

554 Acknowledgments

555 CLT and TLB gratefully acknowledge funding by the ERC under the project *ReactiveFronts*
 556 648377. CLT would like to thank also l'Ecole des Docteurs de l'UBL, le Conseil Regional de
 557 Bretagne and OZCAR-RI for supporting this work. TA is supported by a Marie Skłodowska
 558 Curie Individual Fellowship, under the project *ChemicalWalks* 792041. CB acknowledges funding
 559 from Region Bretagne and Rennes Metropole.

560 Appendix A Notations

561 We detail all notations used in the study in table 3.

562 Appendix B Analytical solutions

563 This appendix details the analytical derivations for effective kinetics under coupled diffusion and
 564 non-linear reactions based on the assumption of Gaussian distribution of the reactant (Eq. (13))
 565 for $t \gg Da$ and of negligible diffusion for $t \ll Da$. The validity of these assumptions is discussed
 566 in Appendix C. The cases of low and high Damköhler are detailed separately below.

567 B.1 Low Damköhler number

568 In the limit of low Da , diffusion quickly deforms the pulse into a Gaussian distribution (Eq. (13)),
 569 whose variance evolves diffusively (see Appendix C and Fig. C.3),

$$\sigma^2(t) \approx \frac{t + Da/12}{Da}, \quad (\text{B.1})$$

570 where we have set $\sigma^2(0) = 1/12$ to match the variance of the initial rectangular profile. Inserting
 571 Eq. (B.1) into (14), we obtain

$$M(t) = \left[M_i - \frac{2}{\sqrt{\beta}} \frac{1-\beta}{3-\beta} \left(\frac{2\pi}{Da} \right)^{\frac{1-\beta}{2}} \left[(t + Da)^{\frac{3-\beta}{2}} - Da^{\frac{3-\beta}{2}} \right] \right]^{\frac{1}{1-\beta}}, \quad (\text{B.2})$$

572 with the initial mass $M_i \approx M(0) = 1$. Note that for $\beta = 1, 3$ this solution is singular and is
 573 not valid. For linear kinetics, $\beta = 1$, the concentration profile is exactly Gaussian, and the total
 574 mass decays exponentially. For $\beta = 3$, combining Eq. (14) and Eq. (B.1), and carrying out the
 575 integration explicitly, we obtain

$$M_{\beta=3}(t) = \left[1 + \frac{Da}{\sqrt{3\pi^2}} \log \left(1 + \frac{12t}{Da} \right) \right]^{-1/2}, \quad (\text{B.3})$$

Table 3: Definition of model parameters and units

Parameter	Definition	Units
r	Reaction rate	$\text{mol } L^{-d} T^{-1}$
c	Concentration	$\text{mol } L^{-d}$
c_0	Initial concentration	$\text{mol } L^{-d}$
\bar{c}	Mean concentration	$\text{mol } L^{-d}$
\bar{c}_∞	Normalized residual mean concentration, [-]	
β	non-linear power law exponent	[-]
$\tilde{\beta}$	Power law exponent of the effective kinetic	[-]
k	reaction rate constant	$\text{mol}^{1-\beta} L^{d(\beta-1)} T^{-1}$
D	Diffusion coefficient	$L^2 T^{-1}$
Da	Damköhler number	[-]
L	Characteristic length	L
M	Mass	kg
S	Reference surface	L^2
w_0	Initial width	L
σ	Normalized variance	[-]
t	Time, normalized time	$T, [-]$
t_c	Normalized persistence time	[-]
t_f	Normalized final time, $\beta < 1$	[-]
τ_D	Diffusion characteristic time	T
τ_R	Reaction characteristic time	T
u	Fluid velocity	$L T^{-1}$
V	Volume of the batch	L^3
x	Distance	$\text{mol } L^{-d} T^{-1}$

576 which decays to zero logarithmically as $t \rightarrow \infty$.

577 Since the average concentration is proportional to the total mass (equation (4)), the dimensionless average concentration is equal to the dimensionless mass, $\bar{c}(t) = M(t)$. When $\beta < 1$, the
578 mass reaches zero in a finite time according to Eq. (B.2), given to leading order in Da by
579

$$t_f = \left(\frac{\sqrt{\beta} (3 - \beta)}{2 (1 - \beta)} \right)^{\frac{2}{3-\beta}} \left(\frac{\text{Da}}{2\pi} \right)^{\frac{1-\beta}{3-\beta}}. \quad (\text{B.4})$$

580 For $\beta > 3$, the mass converges from above to an asymptotic minimum value according to
581 Eq. (B.2). To leading order in Da, this gives,

$$\bar{c}_\infty = 1 - \frac{2\text{Da}}{\sqrt{\beta}(\beta - 3)(2\pi)^{\frac{\beta-1}{2}}}. \quad (\text{B.5})$$

582 For $1 < \beta < 3$, Eq. (B.2) follows a power-law decay, which leads to the average concentration,

$$\bar{c}(t) \approx \sqrt{\frac{2\pi}{\text{Da}}} \left(\frac{\sqrt{\beta} (3 - \beta)}{2 (\beta - 1)} \right)^{\frac{1}{\beta-1}} t^{-\frac{3-\beta}{2(\beta-1)}}, \quad (\text{B.6})$$

583 for $t \gg \text{Da}$.

584 Differentiating Eq. (B.6), we find

$$\frac{d}{dt} \bar{c}(t) = -\frac{3 - \beta}{2(\beta - 1)} \frac{\bar{c}(t)}{t}, \quad (\text{B.7})$$

585 Because the average concentration decreases monotonically, $\bar{c}(t)$ is invertible, Solving Eq. (B.6)
586 for time as a function of mean concentration, we have

$$t(\bar{c}) = \left(\frac{2\pi}{\text{Da}} \right)^{\frac{\beta-1}{3-\beta}} \left(\frac{\sqrt{\beta} (3 - \beta)}{2 (\beta - 1)} \right)^{\frac{2}{3-\beta}} \bar{c}^{-\frac{2(\beta-1)}{3-\beta}}. \quad (\text{B.8})$$

587 Thus, the effective kinetics are given by

$$\frac{d}{dt} \bar{c}(t) = \beta^{-\frac{1}{3-\beta}} \left(\frac{\text{Da} (\beta - 1)}{\pi (3 - \beta)} \right)^{\frac{\beta-1}{3-\beta}} \bar{c}^{\frac{1+\beta}{3-\beta}}. \quad (\text{B.9})$$

588 B.2 High Damköhler number

589 We now develop an approximate description for the behavior of the average concentration at
590 high Damköhler. This involves two different regimes.

591 B.2.1 First regime, $t \ll \text{Da}$

592 First, for times $t \ll \text{Da}$, diffusion has not had time to significantly deform the initial condition.
593 Thus, the average concentration evolves approximately according to the batch dynamics,

$$\frac{d\bar{c}(t)}{dt} = -\bar{c}(t)^\beta, \quad (\text{B.10})$$

594 and we obtain

$$\bar{c}(t) = [1 + (\beta - 1)t]^{-\frac{1}{\beta-1}}. \quad (\text{B.11})$$

595 For $\beta < 1$, the average concentration reaches zero during this regime at the time given by
596 Eq. (19).

597 **B.2.2 Second regime, $t \gg \text{Da}$,**

598 For $t > \text{Da}$, the spreading of the pulse by diffusion cannot be neglected. Rearranging Eqs. (14)
599 and (18), we obtain for the variance

$$\frac{d \log \sigma(t)}{dt} = \frac{1}{2\text{Da}\sigma^2(t)} - (\sqrt{\beta} - 1) \frac{d \log M(t)}{dt}. \quad (\text{B.12})$$

600 If the first term on the right hand side of Eq. (B.12) dominates compared to the second term, the
601 evolution of the variance is approximately diffusive. Otherwise, if the second term dominates,
602 the evolution of the variance is driven by the effect of reaction. Inserting Eq. (B.11) into (B.12),
603 the condition for diffusion-dominated growth is thus

$$\sigma(t)^{3-\beta} M(t)^{\beta-1} < \frac{\sqrt{\beta} - 1}{\sqrt{\beta}} \frac{(2\pi)^{\frac{\beta-1}{2}}}{2\text{Da}}. \quad (\text{B.13})$$

604 We start by evaluating this inequality at $t = \text{Da}$, which is the onset of this second regime.
605 Since mass follows the batch dynamics in the first regime (Eq. (B.11)), at $t = \text{Da}$, it is given by

$$M(\text{Da}) = [1 + (\beta - 1)\text{Da}]^{-\frac{1}{\beta-1}}. \quad (\text{B.14})$$

606 We substitute Eq. (B.14) and $\sigma(\text{Da}) = 1/12$ (corresponding to the initial variance of a rectangular
607 pulse, assumed not to change appreciably up to $t = \text{Da}$) in Eq. (B.13), which gives the condition
608 for a dominant diffusive variance growth at $t = \text{Da}$,

$$\frac{2\text{Da}}{(2\pi)^{\frac{\beta-1}{2}}} \frac{\sqrt{\beta} - 1}{\sqrt{\beta}} \frac{12^{-\frac{3-\beta}{2}}}{1 + (\beta - 1)\text{Da}} < 1. \quad (\text{B.15})$$

609 For a given β , the left hand side of Eq. (B.15) is largest for $\text{Da} \rightarrow \infty$. Therefore, if the criterion
610 holds in this limit, it holds for all Da . In this limit, the condition is

$$\frac{2}{\sqrt{\beta}(\sqrt{\beta} + 1)(2\pi)^{\frac{\beta-1}{2}} 12^{\frac{3-\beta}{2}}} < 1. \quad (\text{B.16})$$

611 This holds for $\beta \lesssim 5$, as verified numerically. We focus on such β since higher β are not commonly
612 encountered. Therefore, at $t = \text{Da}$, the variance growth is dominated by diffusion for the range
613 of β that we consider, leading to a variance equal to

$$\sigma^2(t) \approx \sigma^2(\text{Da}) + \frac{t - \text{Da}}{\text{Da}}, \quad (\text{B.17})$$

614 with $\sigma^2(\text{Da}) = 1/12$, and a mass given by the same equation as for the low Da regime, with the
615 initial mass $M_i \approx M(\text{Da})$, see Eq. (B.2). To test whether the criterion of diffusion dominated
616 variance holds true at larger times, we substitute Eq. (B.17) and Eq. (B.2) in Eq. (B.13). This
617 gives the criterion

$$\frac{2\text{Da}}{(2\pi)^{\frac{\beta-1}{2}}} \frac{\sqrt{\beta} - 1}{\sqrt{\beta}} \frac{\left[\frac{1}{12} + \frac{t - \text{Da}}{\text{Da}}\right]^{\frac{3-\beta}{2}}}{M(\text{Da}) - \frac{2}{\sqrt{\beta}} \frac{1-\beta}{3-\beta} \left(\frac{2\pi}{\text{Da}}\right)^{\frac{1-\beta}{2}} \left[(t + \text{Da})^{\frac{3-\beta}{2}} - \text{Da}^{\frac{3-\beta}{2}}\right]} < 1. \quad (\text{B.18})$$

618 It can be verified numerically that this criterion holds true at all times. For $t \rightarrow \infty$, this simplifies
619 into

$$\frac{3 - \beta}{\sqrt{\beta} + 1} < 1, \quad (\text{B.19})$$

620 which is always true for $\beta > 1$. Hence, the variance evolves diffusively at $t = \text{Da}$ and at all later
 621 times, and a regime with reaction-dominated variance growth is never observed. The accuracy
 622 of the growth of the variance according to Eq. (B.17) is discussed in Appendix C.

623 The effective kinetics can thus be derived as follows for different β . For $1 < \beta < 3$, the
 624 effective kinetics remain given by Eq. (B.9), and the average concentration by Eq. (B.6) with
 625 $M_i = M(\text{Da})$ (Eq. (B.14)). For $\beta > 3$, according to Eq. (B.11) after replacing the initial mass
 626 M_i by $M(\text{Da})$, the mass tends to an asymptotic constant value given by

$$M_\infty = \left[M(\text{Da}) + \text{Da} \frac{2}{\sqrt{\beta}} \frac{\beta - 1}{\beta - 3} (2\pi)^{-\frac{\beta-1}{2}} \right]^{-\frac{1}{\beta-1}}. \quad (\text{B.20})$$

627 At sufficiently large Da , we can neglect $M(\text{Da})$ according to Eq. (B.14) because $\text{Da}^{-\frac{1}{\beta-1}} \ll \text{Da}$.
 628 Thus, we obtain the asymptotic value for the average concentration,

$$\bar{c}_\infty \approx \text{Da}^{-\frac{1}{\beta-1}} \sqrt{2\pi} \left(\frac{\sqrt{\beta} \beta - 3}{2 \beta - 1} \right)^{\frac{1}{\beta-1}}. \quad (\text{B.21})$$

629 Appendix C Hypothesis validation

630 In addition to the numerical validation of the analytical derivation for the effective kinetics,
 631 we further test the validity of the assumptions that we use in our analytical derivations. The
 632 Gaussian assumption and the variance growth assumptions are discussed separately below.

633 C.1 Gaussian assumption

634 Here we assess the validity of the Gaussian assumption for different Damköhler numbers at times
 635 corresponding to different regimes. As highlighted by Eq. (13), Gaussian distributions of different
 636 widths σ and maximum value c_{peak} collapse to a single curve when represented according to the
 637 normalized variables x/σ and c/c_{peak} . It is thus convenient to use this normalization to test the
 638 Gaussian assumption. Furthermore, Gaussian curves are uniquely characterized by the power
 639 law scaling

$$\log(c/c_{peak}) \sim (x/\sigma)^{-2}. \quad (\text{C.1})$$

640 Therefore, Gaussian distributions are characterized by a straight line of slope 2 when representing
 641 $\log(|\log(c/c_{peak})|)$ against $\log(|x/\sigma|)$. Hence, any deviation from this slope corresponds to a non-
 642 Gaussian profile.

643 In Fig. C.1, we test the Gaussian assumption in the case of $\beta = 2$ for low and high Damköhler
 644 numbers, respectively $\text{Da} = 10^{-3}$ and $\text{Da} = 10^3$. At low Da , diffusion acts over much smaller time
 645 scales than reaction, and the profiles are Gaussian at all times (Fig. C.1.a and c), consistently
 646 with the hypothesis of Appendix B.1. For high Da , the early time profiles are non Gaussian
 647 and close to the initial square injection (Fig. C.1.b and d). In this regime, we do not assume
 648 Gaussianity but instead the dominance of reaction over diffusion (Appendix B.2.1). At late
 649 times, $t \gg \text{Da}$, the profiles are very close to Gaussian (Fig. C.1.a and C.1.b) and closely follow
 650 the power law scaling of Eq. (C.1) (Fig. C.1.b and d), which is consistent with the assumption
 651 of Appendix B.2.2.

652 In Fig. C.2, we test the Gaussian assumption for the case of $\beta = 0.5$ for low Damköhler
 653 number, $\text{Da} = 10^{-3}$. We do not represent large Da in Figure C.2 because mass reaches zero
 654 before $t = \text{Da}$ in this case and only the first regime where we do not assume Gaussianity
 655 (Appendix B.2.1) is relevant. Again, consistently with the assumption of Appendix B.1, for low

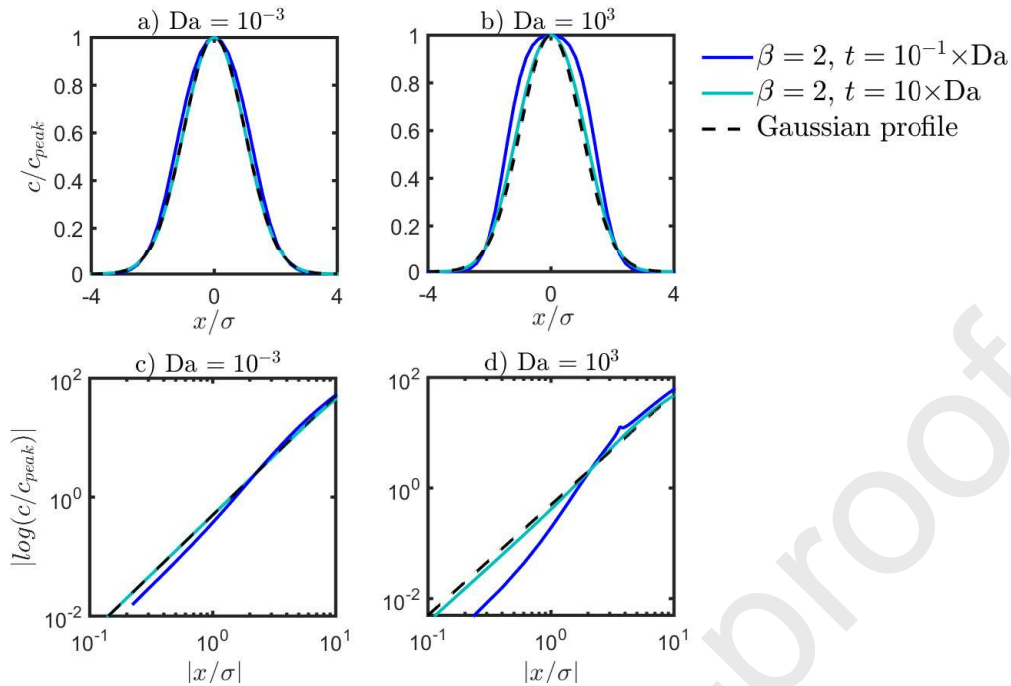


Figure C.1: Test of Gaussianity of reactive pulses from numerical simulations for $\beta = 2$. Comparison of reactive profiles, normalized by their peak values c_{peak} along the y axis and their standard deviation σ along the x axis, with Gaussian profiles at early and late times, respectively $t \approx 10^{-1} \times Da$ and $t \approx 10 \times Da$ for a) $Da = 10^{-3}$, and b) $Da = 10^3$. Test of Gaussian power law scaling (Eq. (C.1)) for the same cases respectively for c) low Da and d) high Da.

656 Da, the profiles are very close to Gaussian at all times (Fig. C.2.a) and closely follows the power
 657 law scaling of Eq. (C.1) (Fig. C.2.b). Results are similar for other reaction orders $\beta < 1$.

658 These results confirm the assumptions that we have made in Appendix B for deriving ap-
 659 proximated analytical solution for the evolution of concentration distributions. For $t \ll Da$, we
 660 do not assume that profiles are Gaussian but we assume that diffusion plays no role and that
 661 the evolution of concentration profiles is dominated by reaction alone. For small Da, this regime
 662 is very short and not considered here. For large Da, this regime is discussed in Appendix B.2.1.
 663 For $t \gg Da$, we assume that profiles are Gaussian, which is consistent with numerical simulations
 664 for all values of Da and β . This regime is discussed in Appendix B.1 and B.2.2.

665 C.2 Variance growth assumption

666 Here, we assess the validity of the assumption that the evolution of the variance is dominated
 667 by the diffusion term in Eq. (B.12). This leads to the prediction that the variance is constant
 668 for $t \ll Da$ and grows diffusively for $t \gg Da$ following Eq. (B.1) for $Da \leq 1$ and Eq. (B.17)
 669 for $Da > 1$. We compare the variance growth in time obtained from numerical simulations with
 670 these predictions for different Damköhler numbers and β in Fig. C.3.

671 In all cases, simulations are found to be in good agreement with analytical solutions. Note
 672 that for $\beta < 1$, the variance computed from numerical simulations starts decreasing at the end
 673 of the simulations, which is not captured by our model (Fig. C.3, a). A short time before the
 674 whole profile reaches zero, concentrations on the sides are reacting faster than they diffuse so

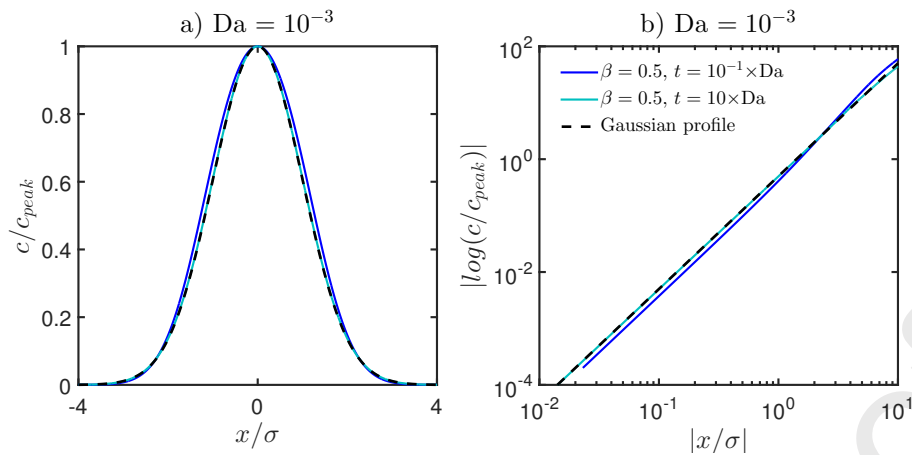


Figure C.2: Test of Gaussianity of reactive pulses from numerical simulations for $\beta = 0.5$. a) Comparison of reactive profiles, normalized by their peak values c_{peak} along the y axis and their standard deviation σ along the x axis, with Gaussian profiles at early and late times, $t \approx 10^{-1} \times Da$ and $t \approx 10 \times Da$ for $Da = 10^{-3}$. The high Da profile is not represented because the mean concentration reaches zero before the times at which we assume Gaussianity, $t = Da$. b) Test of Gaussian power law scaling represented by Eq. (C.1).

675 that the variance starts to decrease before the whole profile reaches zero. This regime of variance
676 decay is thus very short.

677 6 Research data

678 Research Data associated with this article can be accessed at [https://doi.org/10.5281/
679 zenodo.4114532](https://doi.org/10.5281/zenodo.4114532).

680 References

- 681 Aagaard, P. and H. C. Helgeson (1982). “Thermodynamic and kinetic constraints on reaction
682 rates among minerals and aqueous solutions; I, Theoretical considerations”. In: *American
683 journal of Science* 282.3, pp. 237–285.
- 684 Abel, C. D. T., S. K. Sharma, S. A. Mersha, and M. D. Kennedy (2014). “Influence of intermittent
685 infiltration of primary effluent on removal of suspended solids, bulk organic matter, nitrogen
686 and pathogens indicators in a simulated managed aquifer recharge system”. In: *Ecological
687 engineering* 64, pp. 100–107.
- 688 Al-Yamani, W., S. Green, R. Pangilinan, S. Dixon, S. A. Shahid, P. Kemp, and B. Clothier
689 (2019). “Water use of Al Samr (*Acacia tortilis*) forests irrigated with saline groundwater
690 and treated sewage effluent in the hyper-arid deserts of Abu Dhabi”. In: *Agricultural Water
691 Management* 216, pp. 361–364.
- 692 Atchley, A. L., R. M. Maxwell, and A. K. Navarre-Sitchler (2013). “Using streamlines to simulate
693 stochastic reactive transport in heterogeneous aquifers: Kinetic metal release and transport
694 in CO₂ impacted drinking water aquifers”. In: *Advances in water resources* 52, pp. 93–106.

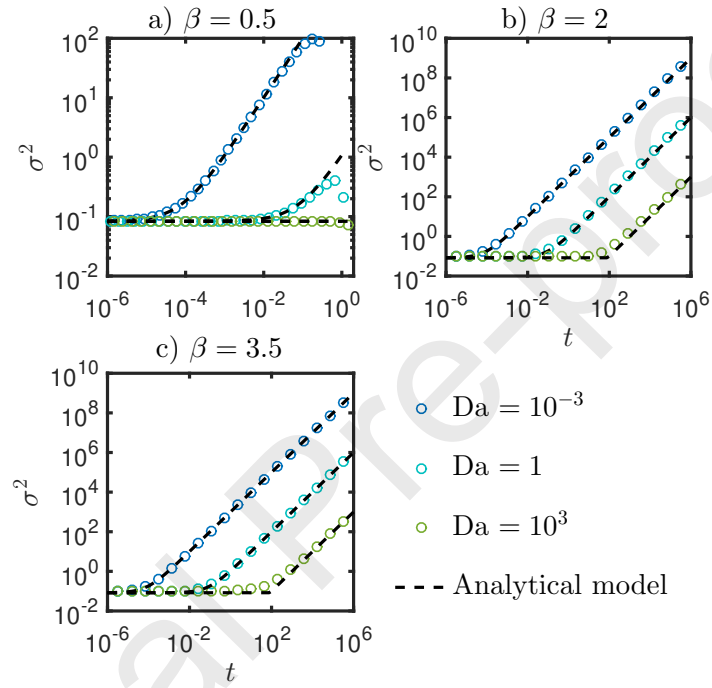


Figure C.3: Test of analytical model for variance growth. Temporal evolution of the reactive pulse variance for a) $\beta = 0.5$, b) $\beta = 2$, c) $\beta = 3.5$, and $Da = 0.001$ (blue circles), $Da = 1$ (turquoise circles), and $Da = 1000$ (green circles). The analytical model predictions, shown by black dashed lines, is given by Eq. (B.1) for $Da \leq 1$ and Eq. (B.17) for $Da \geq 1$

- 695 Atchley, A. L., A. K. Navarre-Sitchler, and R. M. Maxwell (2014). “The effects of physical and
696 geochemical heterogeneities on hydro-geochemical transport and effective reaction rates”. In:
697 *Journal of contaminant hydrology* 165, pp. 53–64.
- 698 Bandopadhyay, A., P. Davy, and T. Le Borgne (2018). “Shear flows accelerate mixing dynamics
699 in hyporheic zones and hillslopes”. In: *Geophysical Research Letters* 45.21, pp. 11–659.
- 700 Battiato, I. and D. M. Tartakovsky (2011). “Applicability regimes for macroscopic models of
701 reactive transport in porous media”. In: *Journal of contaminant hydrology* 120, pp. 18–26.
- 702 Battiato, I., D. M. Tartakovsky, A. M. Tartakovsky, and T. Scheibe (2009). “On breakdown
703 of macroscopic models of mixing-controlled heterogeneous reactions in porous media”. In:
704 *Advances in water resources* 32.11, pp. 1664–1673.
- 705 Beckingham, L. E., E. H. Mitnick, C. I. Steefel, S. Zhang, M. Voltolini, A. M. Swift, L. Yang,
706 D. R. Cole, J. M. Sheets, J. B. Ajo-Franklin, et al. (2016). “Evaluation of mineral reactive
707 surface area estimates for prediction of reactivity of a multi-mineral sediment”. In: *Geochimica
708 et Cosmochimica Acta* 188, pp. 310–329.
- 709 Beckingham, L. E., C. I. Steefel, A. M. Swift, M. Voltolini, L. Yang, L. M. Anovitz, J. M.
710 Sheets, D. R. Cole, T. J. Kneafsey, E. H. Mitnick, et al. (2017). “Evaluation of accessible
711 mineral surface areas for improved prediction of mineral reaction rates in porous media”. In:
712 *Geochimica et Cosmochimica Acta* 205, pp. 31–49.
- 713 Berkowitz, B., A. Cortis, M. Dentz, and H. Scher (2006). “Modeling non-Fickian transport in
714 geological formations as a continuous time random walk”. In: *Reviews of Geophysics* 44.2.
- 715 Bethke, C. (1996). *Geochemical reaction modeling: Concepts and applications*. Oxford University
716 Press on Demand.
- 717 Bleam, W. (2017). “Chapter 9-reduction-oxidation chemistry”. In: *Soil and Environmental Chem-
718 istry*, pp. 445–489.
- 719 Bochet, O., L. Bethencourt, A. Dufresne, J. Farasin, M. Pédrot, T. Labasque, E. Chatton, N.
720 Lavenant, C. Petton, B. W. Abbott, et al. (2020). “Iron-oxidizer hotspots formed by inter-
721 mittent oxic-anoxic fluid mixing in fractured rocks”. In: *Nature Geoscience* 13.2, pp. 149–
722 155.
- 723 Burté, L., C. A. Cravotta III, L. Bethencourt, J. Farasin, M. Pédrot, A. Dufresne, M.-F. Gerard,
724 C. Baranger, T. Le Borgne, and L. Aquilina (2019). “Kinetic study on clogging of a geother-
725 mal pumping well triggered by mixing-induced biogeochemical reactions”. In: *Environmental
726 science & technology* 53.10, pp. 5848–5857.
- 727 Datta, S., B. Mailloux, H.-B. Jung, M. A. Hoque, M. Stute, K. M. Ahmed, and Y. Zheng (2009).
728 “Redox trapping of arsenic during groundwater discharge in sediments from the Meghna river-
729 bank in Bangladesh”. In: *Proceedings of the National Academy of Sciences* 106.40, pp. 16930–
730 16935.
- 731 De Anna, P., J. Jimenez-Martinez, H. Tabuteau, R. Turuban, T. Le Borgne, M. Derrien, and
732 Y. Meheust (2014a). “Mixing and reaction kinetics in porous media: An experimental pore
733 scale quantification”. In: *Environmental Science and Technology* 48.1, pp. 508–516.
- 734 De Anna, P., M. Dentz, A. Tartakovsky, and T. Le Borgne (2014b). “The filamentary structure
735 of mixing fronts and its control on reaction kinetics in porous media flows”. In: *Geophysical
736 Research Letters* 41.13, pp. 4586–4593.
- 737 DePaolo, D. J. and D. R. Cole (2013). “Geochemistry of geologic carbon sequestration: an
738 overview”. In: *Reviews in Mineralogy and Geochemistry* 77.1, pp. 1–14.
- 739 Deng, H., S. Molins, D. Trebotich, C. Steefel, and D. DePaolo (2018). “Pore-scale numerical inves-
740 tigation of the impacts of surface roughness: Upscaling of reaction rates in rough fractures”.
741 In: *Geochimica et Cosmochimica Acta* 239, pp. 374–389.
- 742 Dentz, M., T. Le Borgne, A. Englert, and B. Bijeljic (2011a). “Mixing, spreading and reaction in
743 heterogeneous media: A brief review”. In: *Journal of contaminant hydrology* 120, pp. 1–17.

- 744 Dentz, M., T. Le Borgne, A. Englert, and B. Bijeljic (2011b). “Mixing, spreading and reaction in
745 heterogeneous media: A brief review”. In: *Journal of Contaminant Hydrology* 120-121, pp. 1–
746 17.
- 747 Dutta, T., A. Carles-Brangarí, D. Fernández-García, S. Rubol, J. Tirado-Conde, and X. Sanchez-
748 Vila (2015). “Vadose zone oxygen (O₂) dynamics during drying and wetting cycles: an arti-
749 ficial recharge laboratory experiment”. In: *Journal of Hydrology* 527, pp. 151–159.
- 750 Elberling, B., R. Nicholson, and J. Scharer (1994). “A combined kinetic and diffusion model for
751 pyrite oxidation in tailings: a change in controls with time”. In: *Journal of Hydrology* 157.1-4,
752 pp. 47–60.
- 753 Fenwick, D., C. Scheidt, and J. Caers (2014). “Quantifying asymmetric parameter interactions
754 in sensitivity analysis: application to reservoir modeling”. In: *Mathematical Geosciences* 46.4,
755 pp. 493–511.
- 756 Giammar, D. E., R. G. Bruant Jr, and C. A. Peters (2005). “Forsterite dissolution and magnesite
757 precipitation at conditions relevant for deep saline aquifer storage and sequestration of carbon
758 dioxide”. In: *Chemical Geology* 217.3-4, pp. 257–276.
- 759 Gramling, C. M., C. F. Harvey, and L. C. Meigs (2002). “Reactive transport in porous media:
760 A comparison of model prediction with laboratory visualization”. In: *Environmental science
761 & technology* 36.11, pp. 2508–2514.
- 762 Guo, J., M. Quintard, and F. Laouafa (2015). “Dispersion in porous media with heterogeneous
763 nonlinear reactions”. In: *Transport in Porous Media* 109.3, pp. 541–570.
- 764 Hellmann, R. and D. Tisserand (2006). “Dissolution kinetics as a function of the Gibbs free energy
765 of reaction: An experimental study based on albite feldspar”. In: *Geochimica et Cosmochimica
766 Acta* 70.2, pp. 364–383.
- 767 Hermans, T., F. Nguyen, M. Klepikova, A. Dassargues, and J. Caers (2018). “Uncertainty
768 quantification of medium-term heat storage from short-term geophysical experiments using
769 Bayesian evidential learning”. In: *Water Resources Research* 54.4, pp. 2931–2948.
- 770 Heyman, J., D. R. Lester, R. Turuban, Y. Méheust, and T. Le Borgne (2020). “Stretching and
771 folding sustain microscale chemical gradients in porous media”. In: *Proceedings of the National
772 Academy of Sciences*.
- 773 Hinsinger, P., C. Plassard, C. Tang, and B. Jaillard (2003). “Origins of root-mediated pH changes
774 in the rhizosphere and their responses to environmental constraints: a review”. In: *Plant and
775 soil* 248.1-2, pp. 43–59.
- 776 Hubbard, C. G., S. Black, and M. L. Coleman (2009). “Aqueous geochemistry and oxygen isotope
777 compositions of acid mine drainage from the Río Tinto, SW Spain, highlight inconsistencies
778 in current models”. In: *Chemical Geology* 265.3-4, pp. 321–334.
- 779 Hubert, A., T. Aquino, H. Tabuteau, Y. Méheust, and T. Le Borgne (2020). “Enhanced and non-
780 monotonic effective kinetics of solute pulses under Michaelis–Menten reactions”. In: *Advances
781 in Water Resources* 146, p. 103739.
- 782 Johnson, N. C., B. Thomas, K. Maher, R. J. Rosenbauer, D. Bird, and G. E. Brown Jr (2014).
783 “Olivine dissolution and carbonation under conditions relevant for in situ carbon storage”.
784 In: *Chemical Geology* 373, pp. 93–105.
- 785 Jun, Y.-S., D. E. Giammar, and C. J. Werth (2013). *Impacts of geochemical reactions on geologic
786 carbon sequestration*.
- 787 Jung, H. and A. Navarre-Sitchler (2018a). “Physical heterogeneity control on effective mineral
788 dissolution rates”. In: *Geochimica et Cosmochimica Acta* 227, pp. 246–263.
- 789 — (2018b). “Scale effect on the time dependence of mineral dissolution rates in physically het-
790 erogeneous porous media”. In: *Geochimica et Cosmochimica Acta* 234, pp. 70–83.

- 791 Keiluweit, M., P. S. Nico, M. Kleber, and S. Fendorf (2016). “Are oxygen limitations under
792 recognized regulators of organic carbon turnover in upland soils?” In: *Biogeochemistry* 127.2,
793 pp. 157–171.
- 794 Kirchner, J. W. and C. Neal (2013). “Universal fractal scaling in stream chemistry and its
795 implications for solute transport and water quality trend detection”. In: *Proceedings of the*
796 *National Academy of Sciences* 110.30, pp. 12213–12218.
- 797 Kitanidis, P. K. (1994). “The concept of the dilution index”. In: *Water resources research* 30.7,
798 pp. 2011–2026.
- 799 Kitanidis, P. K. and P. L. McCarty (2012). *Delivery and Mixing in the Subsurface: Processes and*
800 *Design Principles for In Situ Remediation*. Vol. 4. Springer Science & Business Media.
- 801 Largette, L. and R. Pasquier (2016). “A review of the kinetics adsorption models and their
802 application to the adsorption of lead by an activated carbon”. In: *Chemical Engineering*
803 *Research and Design* 109, pp. 495–504.
- 804 Lasaga, A. C., J. M. Soler, J. Ganor, T. E. Burch, and K. L. Nagy (1994). “Chemical weather-
805 ing rate laws and global geochemical cycles”. In: *Geochimica et Cosmochimica Acta* 58.10,
806 pp. 2361–2386.
- 807 Lazareva, O., G. Druschel, and T. Pichler (2015). “Understanding arsenic behavior in carbonate
808 aquifers: Implications for aquifer storage and recovery (ASR)”. In: *Applied Geochemistry* 52,
809 pp. 57–66.
- 810 Le Borgne, T., M. Dentz, and E. Villiermaux (2013). “Stretching, coalescence, and mixing in
811 porous media”. In: *Physical review letters* 110.20, p. 204501.
- 812 Le Borgne, T., T. R. Ginn, and M. Dentz (2014). “Impact of fluid deformation on mixing-induced
813 chemical reactions in heterogeneous flows”. In: *Geophysical Research Letters* 41.22, pp. 7898–
814 7906.
- 815 Le Borgne, T., M. Dentz, and E. Villiermaux (2015). “The lamellar description of mixing in
816 porous media”. In:
- 817 Le Borgne, T., P. D. Huck, M. Dentz, and E. Villiermaux (2017). “Scalar gradients in stirred
818 mixtures and the deconstruction of random fields”. In:
- 819 Li, L., C. I. Steefel, and L. Yang (2008). “Scale dependence of mineral dissolution rates within
820 single pores and fractures”. In: *Geochimica et Cosmochimica Acta* 72.2, pp. 360–377.
- 821 Li, L., K. Maher, A. Navarre-Sitchler, J. Druhan, C. Meile, C. Lawrence, J. Moore, J. Perdrial,
822 P. Sullivan, and A. e. a. Thompson (2017). “Expanding the role of reactive transport models
823 in critical zone processes”. In: *Earth-science reviews* 165, pp. 280–301.
- 824 Llewellyn, G. T., F. Dorman, J. L. Westland, D. Yoxtheimer, P. Grieve, T. Sowers, E. Humston-
825 Fulmer, and S. L. Brantley (2015). “Evaluating a groundwater supply contamination incident
826 attributed to Marcellus Shale gas development”. In: *Proceedings of the National Academy of*
827 *Sciences* 112.20, pp. 6325–6330.
- 828 Magesan, G. N., C. D. A. McLay, and V. V. Lal (1998). “Nitrate leaching from a free-draining
829 volcanic soil irrigated with municipal sewage effluent in New Zealand”. In: *Agriculture, ecosys-*
830 *tems & environment* 70.2-3, pp. 181–187.
- 831 Maher, K. (2011). “The role of fluid residence time and topographic scales in determining chem-
832 ical fluxes from landscapes”. In: *Earth and Planetary Science Letters* 312.1-2, pp. 48–58.
- 833 Maher, K. and C. P. Chamberlain (2014). “Hydrologic regulation of chemical weathering and
834 the geologic carbon cycle”. In: *Science* 343.6178, pp. 1502–1504.
- 835 Maher, K. and A. Navarre-Sitchler (2019). “Reactive transport processes that drive chemical
836 weathering: From making space for water to dismantling continents”. In: *Reviews in Miner-*
837 *alogy and Geochemistry* 85.1, pp. 349–380.
- 838 Maher, K. and K. U. Mayer (2019). “The art of reactive transport model building”. In: *Elements*
839 15.2, pp. 117–118.

- 840 Maher, K., C. I. Steefel, D. J. DePaolo, and B. E. Viani (2006). “The mineral dissolution rate
841 conundrum: Insights from reactive transport modeling of U isotopes and pore fluid chemistry
842 in marine sediments”. In: *Geochimica et Cosmochimica Acta* 70.2, pp. 337–363.
- 843 Malmström, M. E., G. Destouni, S. A. Banwart, and B. H. E. Strömberg (2000). “Resolving the
844 scale-dependence of mineral weathering rates”. In: *Environmental science & technology* 34.7,
845 pp. 1375–1378.
- 846 Malzone, J. M., C. S. Lowry, and A. S. Ward (2016). “Response of the hyporheic zone to transient
847 groundwater fluctuations on the annual and storm event time scales”. In: *Water Resources*
848 *Research* 52.7, pp. 5301–5321.
- 849 McKibben, M. A. and H. L. Barnes (1986). “Oxidation of pyrite in low temperature acidic solu-
850 tions: Rate laws and surface textures”. In: *Geochimica et Cosmochimica Acta* 50.7, pp. 1509–
851 1520.
- 852 Meile, C. and K. Tuncay (2006). “Scale dependence of reaction rates in porous media”. In:
853 *Advances in Water Resources* 29.1, pp. 62–71.
- 854 Molins, S., D. Trebotich, C. I. Steefel, and C. Shen (2012). “An investigation of the effect of
855 pore scale flow on average geochemical reaction rates using direct numerical simulation”. In:
856 *Water Resources Research* 48.3.
- 857 Molins, S., D. Trebotich, L. Yang, J. B. Ajo-Franklin, T. J. Ligoeki, C. Shen, and C. I. Steefel
858 (2014). “Pore-scale controls on calcite dissolution rates from flow-through laboratory and
859 numerical experiments”. In: *Environmental science & technology* 48.13, pp. 7453–7460.
- 860 Moussout, H., H. Ahlafi, M. Aazza, and H. Maghat (2018). “Critical of linear and nonlinear equa-
861 tions of pseudo-first order and pseudo-second order kinetic models”. In: *Karbala International*
862 *Journal of Modern Science* 4.2, pp. 244–254.
- 863 Murphy, S. F., R. B. McCleskey, D. A. Martin, J. H. Writer, and B. A. Ebel (2018). “Fire, flood,
864 and drought: extreme climate events alter flow paths and stream chemistry”. In: *Journal of*
865 *Geophysical Research: Biogeosciences* 123.8, pp. 2513–2526.
- 866 Navarre-Stichler, A. and S. Brantley (2007). “Basalt weathering across scales”. In: *Earth and*
867 *Planetary Science Letters* 261.1-2, pp. 321–334.
- 868 Palandri, J. L. and Y. K. Kharaka (2004). *A compilation of rate parameters of water-mineral*
869 *interaction kinetics for application to geochemical modeling*. Tech. rep. Geological Survey
870 Menlo Park CA.
- 871 Panfilov, M. (2010). “Underground storage of hydrogen: in situ self-organisation and methane
872 generation”. In: *Transport in porous media* 85.3, pp. 841–865.
- 873 Perry, R. H., D. W. Green, and J. O. Maloney (1997). “Perry’s handbook of chemical engineer-
874 ing”. In: *Perry’s Handbook of Chemical Engineering*.
- 875 Plummer, L. N. and T. M. L. Wigley (1976). “The dissolution of calcite in CO₂-saturated solu-
876 tions at 25 C and 1 atmosphere total pressure”. In: *Geochimica et Cosmochimica Acta* 40.2,
877 pp. 191–202.
- 878 Pujades, E., S. Orban P. and Bodeux, P. Archambeau, S. Erpicum, and A. Dassargues (2017).
879 “Underground pumped storage hydropower plants using open pit mines: How do groundwater
880 exchanges influence the efficiency?” In: *Applied energy* 190, pp. 135–146.
- 881 Robati, D. (2013). “Pseudo-second-order kinetic equations for modeling adsorption systems for
882 removal of lead ions using multi-walled carbon nanotube”. In: *Journal of nanostructure in*
883 *Chemistry* 3.1, p. 55.
- 884 Rolle, M. and T. Le Borgne (2019). “Mixing and reactive fronts in the subsurface”. In: *Reviews*
885 *in Mineralogy and Geochemistry* 85.1, pp. 111–142.
- 886 Rudzinski, W. and W. Plazinski (2006). “Kinetics of solute adsorption at solid/solution interfaces:
887 a theoretical development of the empirical pseudo-first and pseudo-second order kinetic rate

- 888 equations, based on applying the statistical rate theory of interfacial transport”. In: *The*
889 *Journal of Physical Chemistry B* 110.33, pp. 16514–16525.
- 890 Salehikhoo, F., L. Li, and S. L. Brantley (2013). “Magnesite dissolution rates at different spatial
891 scales: The role of mineral spatial distribution and flow velocity”. In: *Geochimica et Cos-*
892 *mochimica Acta* 108, pp. 91–106.
- 893 Serrano, S. E. (2001). “Solute transport under non-linear sorption and decay”. In: *Water Research*
894 35.6, pp. 1525–1533.
- 895 — (2003). “Propagation of nonlinear reactive contaminants in porous media”. In: *Water Re-*
896 *sources Research* 39.8.
- 897 Skeel, R. D. and M. Berzins (1990). “A method for the spatial discretization of parabolic equa-
898 tions in one space variable”. In: *SIAM journal on scientific and statistical computing* 11.1,
899 pp. 1–32.
- 900 Song, X., J. Zhang, C. Zhan, Y. Xuan, M. Ye, and C. Xu (2015). “Global sensitivity analysis
901 in hydrological modeling: Review of concepts, methods, theoretical framework, and applica-
902 tions”. In: *Journal of hydrology* 523, pp. 739–757.
- 903 Soulaire, C., S. Roman, A. Kovscek, and H. A. Tchelepi (2017). “Mineral dissolution and
904 wormholing from a pore-scale perspective”. In:
- 905 Steefel, C. I. and A. C. Lasaga (1994). “A coupled model for transport of multiple chemical
906 species and kinetic precipitation/dissolution reactions with application to reactive flow in
907 single phase hydrothermal systems”. In: *American Journal of science* 294.5, pp. 529–592.
- 908 Steefel, C., C. Appelo, B. Arora, D. Jacques, T. Kalbacher, O. Kolditz, V. Lagneau, P. Lichtner,
909 K. U. Mayer, J. Meeussen, et al. (2015). “Reactive transport codes for subsurface environ-
910 mental simulation”. In: *Computational Geosciences* 19.3, pp. 445–478.
- 911 Steefel, C. I., D. J. DePaolo, and P. C. Lichtner (2005). “Reactive transport modeling: An
912 essential tool and a new research approach for the Earth sciences”. In: *Earth and Planetary*
913 *Science Letters* 240.3-4, pp. 539–558.
- 914 Szulczewski, M. L., C. W. MacMinn, H. J. Herzog, and R. Juanes (2012). “Lifetime of car-
915 bon capture and storage as a climate-change mitigation technology”. In: *Proceedings of the*
916 *National Academy of Sciences* 109.14, pp. 5185–5189.
- 917 Trauth, N. and J. H. Fleckenstein (2017). “Single discharge events increase reactive efficiency of
918 the hyporheic zone”. In: *Water Resources Research* 53.1, pp. 779–798.
- 919 Urióstegui, S. H., R. K. Bibby, B. K. Esser, and J. F. Clark (2016). “Quantifying groundwater
920 travel time near managed recharge operations using 35S as an intrinsic tracer”. In: *Journal*
921 *of Hydrology* 543, pp. 145–154.
- 922 Valocchi, A. J., D. Bolster, and C. J. Werth (2019). “Mixing-limited reactions in porous media”.
923 In: *Transport in Porous Media* 130.1, pp. 157–182.
- 924 Van Cappellen, P. and J.-F. Gaillard (2018). “Biogeochemical dynamics in aquatic sediments”.
925 In: *Reactive transport in porous media*, pp. 335–376.
- 926 Villiermaux, E. (2019). “Mixing versus stirring”. In: *Annual Review of Fluid Mechanics* 51,
927 pp. 245–273.
- 928 Wang, L., H. Wen, and L. Li (2018). “Scale dependence of surface complexation capacity and
929 rates in heterogeneous media”. In: *Science of The Total Environment* 635, pp. 1547–1555.
- 930 Weber J., W. J., P. M. McGinley, and L. E. Katz (1991). “Sorptions phenomena in subsurface
931 systems: concepts, models and effects on contaminant fate and transport”. In: *Water research*
932 25.5, pp. 499–528.
- 933 Wen, H. and L. Li (2017a). “An upscaled rate law for magnesite dissolution in heterogeneous
934 porous media”. In: *Geochimica et Cosmochimica Acta* 210, pp. 289–305.
- 935 — (2017b). “An upscaled rate law for magnesite dissolution in heterogeneous porous media”.
936 In: *Geochimica et Cosmochimica Acta* 210, pp. 289–305.

- 937 Wen, H. and L. Li (2018). “An upscaled rate law for mineral dissolution in heterogeneous media:
938 The role of time and length scales”. In: *Geochimica et Cosmochimica Acta* 235, pp. 1–20.
- 939 White, A. F. and S. L. Brantley (2003). “The effect of time on the weathering of silicate minerals:
940 why do weathering rates differ in the laboratory and field?” In: *Chemical Geology* 202.3-4,
941 pp. 479–506.
- 942 Wu, F.-C., R.-L. Tseng, S.-C. Huang, and R.-S. Juang (2009). “Characteristics of pseudo-second-
943 order kinetic model for liquid-phase adsorption: a mini-review”. In: *Chemical Engineering*
944 *Journal* 151.1-3, pp. 1–9.
- 945 Xu, T., S. P. White, K. Pruess, and G. H. Brimhall (2000). “Modeling of pyrite oxidation in
946 saturated and unsaturated subsurface flow systems”. In: *Transport in porous media* 39.1,
947 pp. 25–56.
- 948 Yang, C., J. Samper, J. Molinero, and M. Bonilla (2007). “Modelling geochemical and microbial
949 consumption of dissolved oxygen after backfilling a high level radioactive waste repository”.
950 In: *Journal of Contaminant Hydrology* 93.1-4, pp. 130–148.

Effective kinetics driven by dynamic concentration gradients under coupled transport and reaction

Charlotte Le Traon^{*1}, Tomás Aquino¹, Camille Bouchez¹, Kate Maher², and Tanguy Le Borgne¹

¹Université de Rennes 1, CNRS, Géosciences Rennes UMR 6118, 35042 Rennes, France

²Department of Geological and Environmental Sciences, Braun Hall #118, 450 Serra Mall, Stanford University, Stanford, CA, 94305, USA

March 31, 2021

Abstract

Biogeochemical reaction kinetics are generally **established** from batch reactors where concentrations are uniform. In natural systems, many biogeochemical processes are characterized by spatially and temporally variable concentration gradients that often occur at scales which are not resolved by **field measurements** or biogeochemical and reactive transport models. Yet, it is not clear how these sub-scale chemical gradients affect reaction kinetics compared to batch kinetics. Here we investigate this question by studying the paradigmatic case of localized pulses of solute reacting with a solid or a dissolved species in excess. We consider non-linear biogeochemical reactions, representative of mineral dissolution, adsorption and redox reactions, which we quantify using simplified power-law kinetics. The combined effect of diffusion and reaction leads to effective kinetics that differ quantitatively and qualitatively from the batch kinetics. Depending on the nonlinearity (**reaction order**) of the local kinetics, these effects lead to either enhancement or decrease of the overall reaction rate, and result in a rich variety of reaction dynamics. We derive analytical results for the effective kinetics, which are validated by comparison to direct numerical simulations for a broad range of Damköhler numbers and reaction order. Our findings provide new insights into the interpretation of imperfectly mixed lab experiments, the effective kinetics of field systems characterized by intermittent reactant release and the integration of sub-scale concentration gradients in reactive transport models.

1 Introduction

The kinetics of biogeochemical reactions are used to predict a range of processes, including the weathering of **rock**, the transport and **degradation** contaminants, and the **nutrient cycling** that sustains subsurface microbial life. Given the importance of transport processes in governing the **removal and supply of products and reactants** and the necessity to consider a variety of spatial and temporal scales, reactive transport models are increasingly used to predict processes occurring in the subsurface (e.g., see reviews by Van Cappellen and Gaillard, 2018; Steefel et al., 2005; Li et al., 2017; Maher and

^{*}Corresponding author: charlotte.letraon@univ-rennes1.fr

35) A host of other studies rely on conceptual frameworks that integrate reactive transport principles, with applications ranging from interpretation of global elemental cycles (Lasaga et al., 1994)
36 , to catchment elemental fluxes over synoptic (e.g. Kirchner and Neal, 2013) or geologic timescales
37 (e.g. Maher and Chamberlain, 2014), to nutrient cycling at microsites (e.g. Keiluweit et al., 2016)
38 . In all cases, biogeochemical kinetics have to be represented at an appropriate temporal and spatial
39 scale. However, kinetic models are generally derived from well-mixed batch experiments in the
40 lab . Yet, reaction kinetics can differ by orders of magnitude from homogeneous batch reactors to
41 heterogeneous field systems (White and Brantley, 2003; Meile and Tuncay, 2006; Maher et al., 2006; Navarre-Sitchler
42 . Different hypotheses have been investigated to explain these discrepancies. These include diffusion
43 limitations or geometrical constraints at the pore scale that reduce access of solutes to reactive
44 surfaces compared to fully mixed systems (Molins et al., 2012; Molins et al., 2014; Beckingham et al., 2016; Soula
45 , physical heterogeneity that induces spatially heterogeneous solute fluxes and modifies the effective
46 reactive surfaces (Atchley et al., 2013; Wen and Li, 2017a; Wen and Li, 2018; Jung and Navarre-Sitchler, 2018a;
47 and geochemical heterogeneity, where averaging can also lead to scale effects in effective reaction
48 kinetics (Atchley et al., 2014; Salehikhoo et al., 2013). These studies highlight the role of delayed
49 or heterogeneous access to reactive surfaces at different scales. A complementary question
50 that has received less attention is: what is the impact of heterogeneous and time evolving concentration
51 landscapes on reaction kinetics, when access to reactive surfaces or to other dissolved
52 reactants is not limited?

53 Concentration gradients are created by spatially heterogeneous or transient release of solutes.
54 They can be sustained by stretching induced by flow, whether at pore scale (Heyman et al., 2020)
55 or at Darcy scale (Le Borgne et al., 2017), and are ultimately destroyed by diffusion. In the case
56 of linear kinetics, heterogeneity in concentration fields does not impact the effective kinetics when
57 access to reactive surfaces or other reactants is not limited. However, for non-linear kinetics that
58 imply the local reaction rate is a non-linear function of local solute concentrations, the average
59 reaction rate over a non-homogeneous concentration field is expected to differ from the local
60 kinetics (Battiato et al., 2009; Battiato and Tartakovsky, 2011; Hubert et al., 2020). Such non-
61 linear reaction kinetics play a central role in a broad range of biogeochemical reactions, including
62 dissolution, redox and sorption reactions (Serrano, 2001; Serrano, 2003; Guo et al., 2015). Yet,
63 it is not known how different types of non-linear kinetics may lead to either enhanced or reduced
64 effective kinetics when considering heterogeneous solute plumes.

65 Many physical, climatic, and biological processes result in localized and intermittent release
66 of solutes that generate temporally and spatially variable concentration fields in subsurface environments
67 (Fig. 1). Rain events (Fig. 1.a) leach soil and induce pulses of dissolved chemical
68 compounds into groundwater (Murphy et al., 2018). River stage variations (Fig. 1.b) induce
69 pulses of oxygen-rich water in hyporheic zones and the underlying groundwater systems, leading
70 to chemical disequilibrium and the degradation, fixation or release of contaminants, such
71 as organic carbon, nitrate or arsenic (Datta et al., 2009; Malzone et al., 2016; Trauth and
72 Fleckenstein, 2017; Bandopadhyay et al., 2018). Biological activity in general (Fig. 1.c) , can
73 induce pulses of chemical compounds (e.g. Hinsinger et al., 2003). For instance, roots release
74 dissolved gases and other compounds through daily cycles of respiration and exudation, and via
75 associated fungal and microbial organisms (e.g. Li et al., 2017). Finally engineered injections
76 (Fig. 1.d) create chemical disequilibrium and trigger a range of reactive pulses. This includes
77 managed aquifer recharge (Magesan et al., 1998; Urióstegui et al., 2016; Al-Yamani et al., 2019)
78 , which is often performed by periodically wetting and drying the system (Dutta et al., 2015),
79 leading to biogeochemical reactions such as ammonium-nitrogen reduction and pathogen removal
80 (Abel et al., 2014). Injection of concentrated carbon dioxide into the deep subsurface results
81 in density-driven instabilities, leading to localized high concentrations of reactive CO₂-rich fluid
82 (Szulczewski et al., 2012). Collectively, reactive pulses play an important role in a broad range of
83

84 engineered injections, including soil and groundwater remediation (Kitanidis and McCarty, 2012;
 85 Rolle and Le Borgne, 2019), seasonal energy storage, through heat, hydrogen or underground
 86 pumped storage hydroelectricity (Panfilov, 2010; Pujades et al., 2017; Hermans et al., 2018),
 87 geothermal dipoles (Burté et al., 2019), and injection and storage of water used for fracking
 operations (Llewellyn et al., 2015).

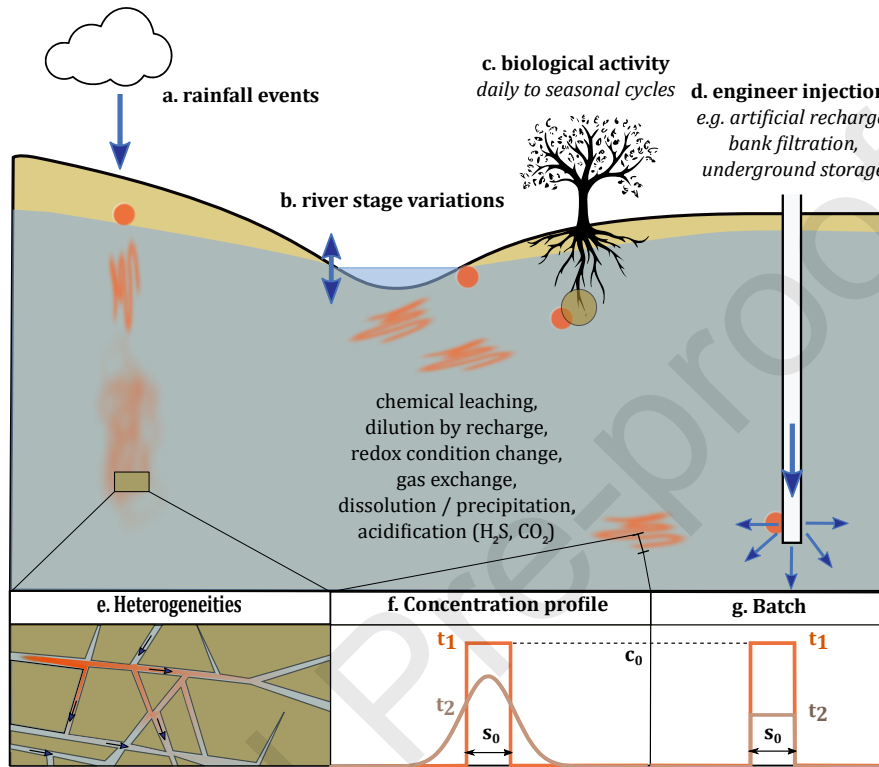


Figure 1: Conceptual representation of biogeochemical pulses in the subsurface. When released, pulses are concentrated and localized (orange dots). As they are transported in the subsurface, they are stretched by velocity gradients and form elongated lamella structures (Le Borgne et al., 2015). Solute concentrations are driven by dilution, which occurs by diffusion along the concentration gradients, and reactions either with minerals or other dissolved solutes. The arrows indicate an injection or an exchange of solute. Four types of processes generating reactive pulses are highlighted: a. soil leaching by rain, b. surface water – groundwater exchanges, c. biological activity (the brown circle represents the root zone), and d. engineered injections. In all these applications, chemical gradients can be enhanced and sustained by physical heterogeneities, as illustrated in inset e. The inset f. illustrates the considered simplified one-dimensional concentration profile that evolve under the action of diffusion and reaction. The effective kinetics of such reactive pulses are compared to batch kinetics that evolve through reaction alone under uniform concentrations (inset g.).

88 Because chemical gradients are enhanced and sustained by physical heterogeneities (Le Borgne
 89 et al., 2013; Heyman et al., 2020) (see inset of Fig. 1), they develop over a range of scales
 90 that cannot be fully resolved by field sampling approaches that average solute (e.g., screened
 91 groundwater wells) or reactive transport models. Hence, effective kinetic models that capture
 92 the effect of sub-scale concentration gradients are required. Macrodispersion theory, where the
 93 dispersive flux is assumed to be proportional to the concentration gradient, tends to strongly
 94

95 underestimate concentration gradients, leading to significant errors when used in reactive trans-
96 port models (Gramling et al., 2002; Dentz et al., 2011a). Non-Fickian dispersion theories have
97 successfully described the asymmetry of solute plumes resulting from trapping in low velocity
98 areas (Berkowitz et al., 2006). However, this framework aims at describing spatial dispersion
99 of solute plumes and does not quantify subscale concentration gradients governed by mixing
100 (Dentz et al., 2011b). Recent mixing theories have provided a new framework to predict the full
101 distribution of concentrations and concentration gradients both at pore scale (Heyman et al., 2020)
102 and at Darcy scale (Le Borgne et al., 2013). In this framework, solute plumes are represented
103 as ensembles of elongated lamellar structures, i.e. solute filaments elongated in one direction
104 and compressed in the other. The latter develop systematically in heterogeneous media both
105 at the pore (De Anna et al., 2014b) and Darcy (Le Borgne et al., 2014) scale. This is due to
106 velocity gradients at different scales that deform solute plumes into such filaments, whose for-
107 mation and merging controls mixing rates (Le Borgne et al., 2015). At the scale of a solute
108 lamella, the effect of stretching on the enhancement of concentration gradients and mixing is
109 quantified explicitly by a change of variable that leads to one-dimensional equation formally
110 identical to a diffusion equation in the direction perpendicular to the lamella (Villiermaux, 2019)
111 . The full distribution of concentration is then predicted from the distribution of stretch-
112 ing rates. While this framework has been successfully used to model mixing-limited reactions
113 (De Anna et al., 2014a; Rolle and Le Borgne, 2019), its coupling with other types of reactions,
114 such as solid-fluid reactions is an outstanding challenge. The key difficulty for this is to first
115 solve analytically the coupling of diffusion transverse to solute lamella with non-linear kinetic
116 laws.

117 Here we use analytical solutions and numerical simulations to establish the effective kinetic
118 laws that result from coupled diffusion and non-linear reactions in spatially and temporally
119 variable concentration gradients. We consider pulses of solute that react either with a homo-
120 geneously distributed solid phase or fluid phase, both in excess with respect to the transported
121 solute. Hence, there is no limitation of access to reactive surfaces or other reactants, which
122 allow use to isolate and formalize the coupling between non-homogeneous concentration distri-
123 butions and non-linear kinetics. Dilution of solute concentration by mixing with the background
124 fluid transfers high concentrations towards lower concentrations (Kitanidis, 1994), which may
125 either reduce or enhance the average kinetics, depending on the reaction order of the local
126 kinetics. Although mixing plays an important role in this problem, it does not act to bring re-
127 actants into contact as extensively studied in the context of mixing-induced reactions, where
128 reactions are limited by the mixing of spatially segregated reactants (see recent reviews of
129 Rolle and Le Borgne, 2019; Valocchi et al., 2019). Instead, we study how changes in concen-
130 tration distributions by mixing may lead to the emergence of effective kinetics that differ from
131 local kinetics. In complex multi-component reactions, this effect acts together with a range of
132 other processes and therefore it is difficult to understand and quantify. Therefore, although we
133 have studied a simplified reaction in order to isolate a particular phenomenon, our results are
134 expected to be relevant to a large range of geochemical systems, where this effect acts together
135 with other known mechanisms, including spatial segregation of reactants either in fluid or in
136 solid phases. In section 2, we present the reactive transport problem. In section 2.1, we define
137 the studied effective quantities. In section 3, we present the numerical and analytical results for
138 a range of Damköhler numbers and non-linear kinetics. In the section 4, we discuss the implica-
139 tions of our findings for different types of reaction, including mineral dissolution, redox reactions
140 and sorption.

2 Reactive transport problem

2.1 Reaction kinetics

We study the reaction of a mobile aqueous species, with concentration c , which reacts with other aqueous species or with a solid surface. The latter are assumed to be in excess and homogeneously distributed, so that the reaction kinetics $r(c)$ only depends on the concentration c through the non-linear rate law:

$$r(c) = kc^\beta, \quad (1)$$

where $\beta > 0$ is the effective order of the reaction and k is the reaction rate constant, which integrates the effect of other species in excess (units $[\text{mol}^{1-\beta} \text{L}^{d(\beta-1)} \text{T}^{-1}]$, where d is the spatial dimension).

In a well-mixed batch reactor, the concentration c is homogeneous in space and depends only on time (see lower right inset of Fig. 1). The concentration decreases everywhere according to the reaction rate (1), so that the kinetic rate law describing the evolution of the mean concentration \bar{c} as a function of time t is given by

$$\frac{d}{dt}\bar{c} = -r(\bar{c}), \quad (2)$$

with $\bar{c} = M/V$, where M is the mass of reactant and V is the volume of the batch reactor.

Although it is simplified, the system isolates the effect of transient concentration gradients on upscaled kinetics. The characterization of this basic yet non-trivial system may thus guide the understanding of more complex biogeochemical systems, where this effect is coupled to other mechanisms, such as heterogeneous reactive surfaces, spatial segregation of multiple elements and mixing limitations. As discussed in section 4, it is relevant for mineral dissolution far-from-equilibrium (Hellmann and Tisserand, 2006; Maher, 2011; Guo et al., 2015), for non-linear sorption kinetics (Weber J. et al., 1991; Perry et al., 1997; Serrano, 2003) and for homogeneous redox reactions where β depends on the stoichiometric coefficients (Bethke, 1996; Blear, 2017). We focus on $\beta \neq 1$, because dilution by mixing has no effect on linear reactions in the sense that the upscaled kinetics are the same as the local kinetics in this case. Indeed, for the linear reaction, $\beta = 1$, mass decay over time is independent of the spatial concentration distribution.

2.2 Reactive pulses

We wish to compare the batch dynamics Eq. (2), to the dynamics of the average concentration under diffusive transport for the same local reaction. Thus, we consider the reactant to be described by a non-homogeneous concentration $c(x, t)$ depending on both position x and time t (see lower middle inset of Fig.1). We assume that the concentration is independent of the other spatial coordinates y and z over a reference surface S . This assumption is taken here for simplicity of analytical derivations, and can be relaxed to consider three dimensional transport processes following the same approach. The concentration is thus assumed to obey the diffusion-reaction equation,

$$\frac{\partial c}{\partial t} - D \frac{\partial^2 c}{\partial x^2} = -r(c), \quad (3)$$

where $D[L^2T^{-1}]$ is the diffusion coefficient, which we assume to be constant. The initial condition is taken as a rectangular pulse identical to the batch conditions, but the pulse is allowed to diffuse in an infinite one-dimensional domain.

At the boundaries, concentration tends to zero. Note that, in natural systems, boundaries limiting diffusive mass transfer would ultimately lead to a homogenization of the domain and a

180 convergence to the batch reaction rates. Our results hence describe the transient regimes before
 181 this happens. For a reference scale L larger than the pulse characteristic size, $L \gg \sqrt{Dt}$, the
 182 mean concentration is,

$$\bar{c} = \frac{M}{LS}. \quad (4)$$

183 The temporal evolution of the mean concentration is obtained by integrating Eq. (3) over space,

$$\frac{d}{dt}\bar{c}(t) = -\frac{k}{L} \int_{-L/2}^{L/2} dx c(x,t)^\beta. \quad (5)$$

184 Note that only the reaction term contributes directly to the change in mass, which can be shown
 185 by integration by parts. However, transport affects the shape of the concentration profile, and
 186 thus indirectly impacts the total mass and the average concentration. This one-dimensional
 187 diffusion-reaction approach is also relevant to understand the effect of plume stretching on reac-
 188 tion kinetics in heterogeneous media. Indeed, solutes transported in the subsurface tend to follow
 189 elongated lamella structures (Le Borgne et al., 2015) where concentrations vary weakly along the
 190 stretching direction and concentration gradients develop mostly in one-dimension transverse to
 191 lamellae (Fig. 1).

192 2.3 Non-dimensional units

193 In order to meaningfully compare the dynamics for different conditions, it is convenient to define
 194 non-dimensional quantities in terms of values characterizing the different physical processes at
 195 play. We define the non-dimensional position as $x_* = x/w_0$, where w_0 is the initial pulse width
 196 , the non-dimensional concentration as $c_* = c/c_0$, where c_0 is the initial concentration, and
 197 the non-dimensional average concentration as $\bar{c}_* = \bar{c}L/(c_0w_0)$. Note that the non-dimensional
 198 initial concentration and average concentration are thus $c_*(0) = \bar{c}_*(0) = 1$. Furthermore, we
 199 define non-dimensional time as t/τ_R , where

$$\tau_R = \frac{1}{kc_0^{\beta-1}} \quad (6)$$

200 is the characteristic reaction time (inverse rate) associated with the initial concentration c_0 . In
 201 the following, we drop the asterisk for notational brevity. All quantities discussed are non-
 202 dimensional in the sense discussed here unless mentioned.

203 In non-dimensional units, the kinetic equation for the batch is,

$$\frac{dc}{dt} = -c^\beta, \quad (7)$$

204 which can be solved with the initial condition $c(0) = 1$ to yield,

$$c(t) = [1 + (\beta - 1)t]^{-\frac{1}{\beta-1}}. \quad (8)$$

205 This solution holds whenever $\beta \neq 1$, that is, for nonlinear reactions. The special case of linear
 206 reactions leads to the classical $c(t) = e^{-t}$ exponential decay.

207 In order to account for the effect of dilution by mixing, we identify the time needed to
 208 homogenize the width of the initial condition as

$$\tau_D = \frac{w_0^2}{2D}, \quad (9)$$

209 corresponding to the time to homogenize a unit distance in nondimensional coordinates. The
 210 relative importance of reaction with respect to dilution is characterized by the dimensionless
 211 Damköhler number

$$\text{Da} = \tau_D / \tau_R. \quad (10)$$

212 Fast reactions relative to dilution correspond to $\text{Da} > 1$, while slow reactions correspond to
 213 $\text{Da} < 1$. In nondimensional terms, the diffusion-reaction equation becomes

$$\frac{\partial c}{\partial t} - \frac{1}{2\text{Da}} \frac{\partial^2 c}{\partial x^2} = -c^\beta. \quad (11)$$

214 Note that, in nondimensional variables, the initial condition is a rectangular pulse of unit width.
 215 The dimensionless total mass obeys

$$\frac{d}{dt} \bar{c}(t) = -\frac{1}{L} \int_{-L/2}^{L/2} dx c(x, t)^\beta. \quad (12)$$

216 All introduced parameters and their units are given in table 3 (Appendix A).

217 2.4

218 2.4 Numerical analysis

219 To explore the different effective reaction regimes, we first solved Eq. (11) numerically using
 220 Matlab's *pdepe* method, a numerical solver for one-dimensional partial differential equations
 221 (Skeel and Berzins, 1990). We use Neumann boundary conditions, i.e. no flux boundary con-
 222 dition, and a rectangular pulse of unit normalized width as initial condition (Fig. 1f). The
 223 domain size is chosen large enough to maintain close to zero concentrations at the domain bound-
 224 aries at the end of the

225 2.5

226 simulation, and the grid discretization is refined to ensure the convergence of the solver. To
 227 analyze the effective kinetics at the pulse scale, that is for averaged concentrations over the
 228 solute pulse, we study the time evolution of the average concentration $\bar{c}(t)$ and the evolution of
 229 the effective reaction rate as a function of the average concentration.

230 We compare these numerical simulations to analytical solutions that we derived using the ap-
 231 proximation discussed in the following section. Furthermore, we test these analytical predictions
 232 for one geochemically relevant example using the multi-component reactive transport model,
 233 CrunchFlow (version 1.0). Boundary and initial conditions for these simulations are described in
 234 the corresponding section. As for Matlab simulations, we use a domain large enough to ensure
 235 that the pulse does not reach the boundary and a grid discretization small enough to ensure
 236 convergence of the results.

237 3

238 2.1 Gaussian approximation for analytical derivations

239 When reactions are described by nonlinear local kinetics, transport and reaction interact in com-
 240 plex ways. Reaction impacts local concentration gradients, which in turn affect diffusive fluxes.

241 The latter leads to changes in the spatial concentration profile, which affects reaction. These
 242 interactions are captured by the diffusion-reaction equation (11). In order to better understand
 243 the interplay between reaction dynamics and dilution, and how it leads to different average ki-
 244 netics compared to a well-mixed batch reactor, we develop an approximate analytical description
 245 of the average concentration, for a range of Damköhler numbers Da and reaction orders β .

246 In non-dimensional units, the initial condition is a rectangular pulse of unit finite width,
 247 identical with the batch conditions. Before diffusion has time to deform the pulse substantially,
 248 which is the case for times much smaller than the characteristic diffusion time τ_D , we expect
 249 the dynamics to be well-approximated by the batch kinetics, so that the average concentration
 250 approximately follows Eq. (8). This corresponds to $t \ll Da$ in nondimensional terms. For
 251 non-dimensional times $t \gtrsim Da$, diffusion has appreciably deformed the initial pulse. To derive
 252 analytical solutions for this problem, we approximate the reactive solute profiles as Gaussian
 253 distributions. This approximation is expected to be highly accurate for low Da when diffusion is
 254 faster at modifying the concentration distribution than reaction. It turns out to be also accurate
 255 in intermediate and high Da ranges (Appendix C), which facilitates an analytical solutions for
 256 the effective kinetics. The concentration distribution of reactive pulses is thus approximated as,

$$c(x, t) = \frac{M(t)}{\sqrt{2\pi\sigma^2(t)}} e^{-\frac{x^2}{2\sigma^2(t)}}, \quad (13)$$

257 where the variance $\sigma^2(t)$ and mass $M(t)$ evolve in time as a function of diffusion and reaction.
 258 Note that in the absence of reaction, the solution corresponds to $M(t) = 1$, and $\sigma^2(t) \propto t/Da$.

259 Inserting Eq. (13) into Eq. (12), we obtain,

$$\frac{d}{dt}M(t) = -\frac{M(t)^\beta}{\sqrt{\beta}} [2\pi\sigma^2(t)]^{\frac{1-\beta}{2}}. \quad (14)$$

260 The Gaussian assumption allows second spatial derivatives in Eq. (11) to be estimated as,

$$\frac{\partial^2 c}{\partial x^2} = \left(-\frac{1}{\sigma^2} + \frac{x^2}{\sigma^4}\right) c, \quad (15)$$

261 hence, at $x = 0$, we have for the maximum concentration,

$$c(0, t) = \frac{M(t)}{\sqrt{2\pi\sigma^2(t)}}, \quad (16)$$

262 and for the second spatial derivative,

$$\frac{\partial^2 c}{\partial x^2} \Big|_{x=0} = -\frac{M(t)}{\sqrt{2\pi}\sigma(t)^3}. \quad (17)$$

263 Inserting Eq. (16) and (17) in Eq. (11) at $x = 0$, we obtain

$$\frac{d}{dt} \frac{M(t)}{\sqrt{2\pi\sigma^2(t)}} = -\frac{M(t)}{2Da\sqrt{2\pi}\sigma(t)^3} - \frac{M(t)^\beta}{(2\pi)^{\beta/2}\sigma(t)^\beta}. \quad (18)$$

264 As discussed in Appendix B, Eq. (14) and (18) provide two independent equations to solve for
 265 the two unknowns $M(t)$ and $\sigma(t)$. Since the average concentration is proportional to the total
 266 mass (equation (4)), the dimensionless average concentration is equal to the dimensionless mass,
 267 $\bar{c}(t) = M(t)$. The accuracy of the Gaussian approximation is discussed in Appendix C.

3 Results

First, numerical simulations for the average concentration as a function of time for different values of β are presented for broad range of Damköhler numbers and reaction orders in order to demonstrate the resulting behavior and departure of the effective kinetics from the batch systems. As expected, for $\beta = 1$, the effective kinetics are equal to the batch kinetics (Fig. 2.b). For the other cases, the results can be generalized as:

- For $\beta < 1$, the average concentration of the pulse decreases faster than in the batch reactor, and the effective reaction rate of the pulse system is globally greater than the batch reactor (Fig. 2a).
- For $\beta > 1$, the average concentration of the pulse decreases more slowly than in the batch reactor and the effective reaction rate of the pulse injected system is globally less than the batch reactor (Fig. 2c-d).

4

Qualitatively, this effect may be understood as follows. For $\beta < 1$, the reaction is more efficient when distributing a given mass in the low concentration range because of the form of the kinetics (Eq. (1)). Dilution by diffusion accelerates the transfer of mass towards lower concentration values and thus enhances the average kinetics compared to the batch case. As a result, the time at which the average concentration goes to zero (Fig. 2.a) decreases with decreasing Da as dilution accelerates the effective kinetics. The opposite effect occurs for $\beta > 1$, leading to a reduction of the effective kinetics compared to batch kinetics. For the extreme case of $\beta > 3$, dilution retards the reaction to such a level that the average concentration converges asymptotically to a nonzero value (Fig. 2.d), with the asymptotic residual concentration increasing with decreasing Da.

The impact of dilution on reaction kinetics may be also understood by plotting the total reaction rate as a function of the average concentration (Fig. 3). For linear kinetics, the effective kinetics are identical to the batch kinetics independent of Da (Fig. 3.b). For low Da and $\beta < 1$, the global reaction rates are always greater than the batch for a given average concentration (Fig. 3.a). For low Da and $\beta > 1$, the global reaction rates are always less than the batch for a given average concentration (Fig. 3.c and Fig. 3.d). The difference between effective reaction kinetics and batch kinetics can reach several orders of magnitude. At low Damköhler numbers (Blue dots in Fig. 3) and quasi-constant average concentration, the variation in the reaction rates is substantial (an increase for $\beta < 1$ and a decrease for $\beta > 1$). This counterintuitive regime is due to the action of diffusion, which distributes mass towards low concentration values, such that while the total reaction rate varies, the overall rate is insufficient to affect the total mass. At high Damköhler numbers (Green dots in Fig. 4) the effective rate first follows a batch-like behavior and then departs towards effective kinetics that are a function on β . In the following, we present our analytical results for the effective kinetics as a function of β .

3.1 Reaction order $\beta < 1$

For $\beta < 1$, the average concentration reaches zero at a finite time t_f (Fig. 4.a). For large Damköhler numbers, diffusion does not have time to induce significant dilution before $t = t_f$. Therefore, this time is identical to the time required to consume the full reactant mass in batch

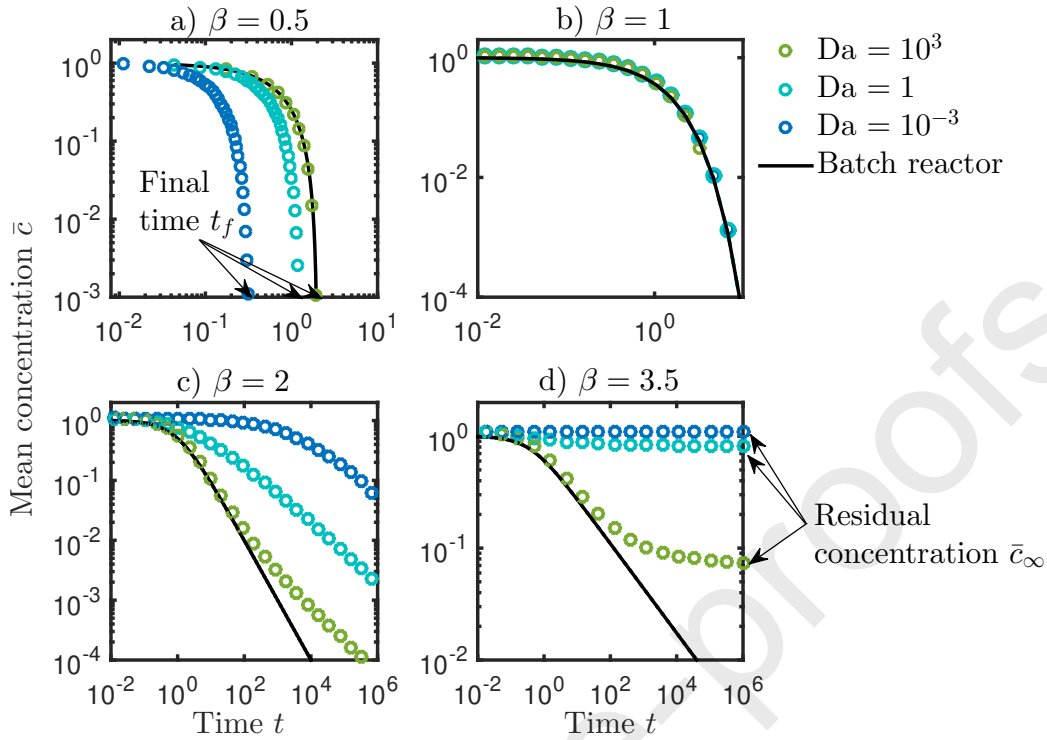


Figure 2: Average concentration in a reactive pulse as a function of time for a) $\beta = 0.5$, b) $\beta = 1$, c) $\beta = 2$ and d) $\beta = 3.5$. Numerical simulations for low, intermediate and high Da numbers (circles) are compared to batch kinetics (black solid line). The final time for full reactant consumption t_f , which occurs for $\beta < 1$, is indicated with arrows in figure a). The residual average concentration \bar{c}_∞ , which occurs for $\beta > 3$, is indicated with arrows in figure d). Note that the y-axis differs between panels to resolve the differences in concentration evolution.

309 reactions (Green dots and line in Fig. 4.a, Appendix B.2.1) :

$$t_f = \frac{1}{1 - \beta}, \text{ for } Da > 1. \quad (19)$$

310 For low Damköhler numbers, using the assumption of a Gaussian concentration distribution, we
 311 obtain a solution for the evolution of the average concentration (Appendix B.1, Eq. (B.2)), in
 312 good agreement with numerical simulations (Blue dots and dashed lines in Fig. 4.a). This leads
 313 to the following estimate of t_f (Appendix B.1, Eq. (B.4)),

$$t_f \sim Da^{\frac{1-\beta}{3-\beta}}, \text{ for } Da < 1. \quad (20)$$

314 This scaling and the convergence to a constant value given by Eq. (19) at large Da are verified
 315 from numerical simulations in Fig. 4.b. The effect of dilution is thus to accelerate the effective
 316 kinetics, with a consumption time up to ten times less than predicted from the batch kinetics
 317 for $Da = 10^{-3}$.

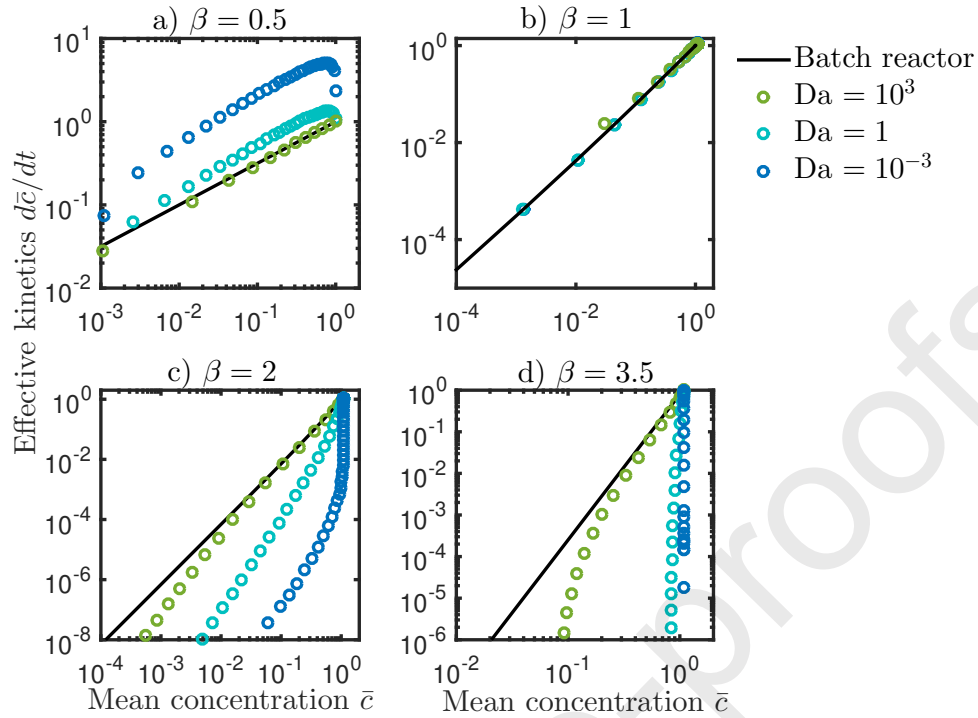


Figure 3: Effective kinetics of reactive pulses quantified as the rate of change of the mean concentration as a function of mean concentration for a) $\beta = 0.5$, b) $\beta = 1$, c) $\beta = 2$ and d) $\beta = 3.5$. Numerical simulations for low, intermediate and high Da numbers (circles) are compared to the batch reactor solution (black solid line). Note that the y-axis differs between panels to resolve the differences in concentration evolution.

3.2 Reaction order $1 < \beta < 3$

For $1 < \beta < 3$, we predict that the departure from the batch kinetics is not only a difference in the magnitude of the reaction but also in its order. The latter is shown by the power law scaling that relates the average reaction rate to the average concentration (dashed lines in Fig. 5), with an exponent that differs from the batch reaction order. For low Damköhler numbers, our solution implies that the average concentration decays in time as a power law (Appendix B.1, Eq. (B.6)),

$$\bar{c}(t) \sim t^{-\frac{3-\beta}{2(\beta-1)}}, \quad (21)$$

and the effective rate r_M follows (Appendix B.1, Eq. (B.9))

$$\frac{d\bar{c}}{dt} \sim \bar{c}^{\tilde{\beta}}, \quad (22)$$

with

the effective reaction order

$$\tilde{\beta},$$

$$\tilde{\beta} = \frac{1+\beta}{3-\beta}. \quad (23)$$

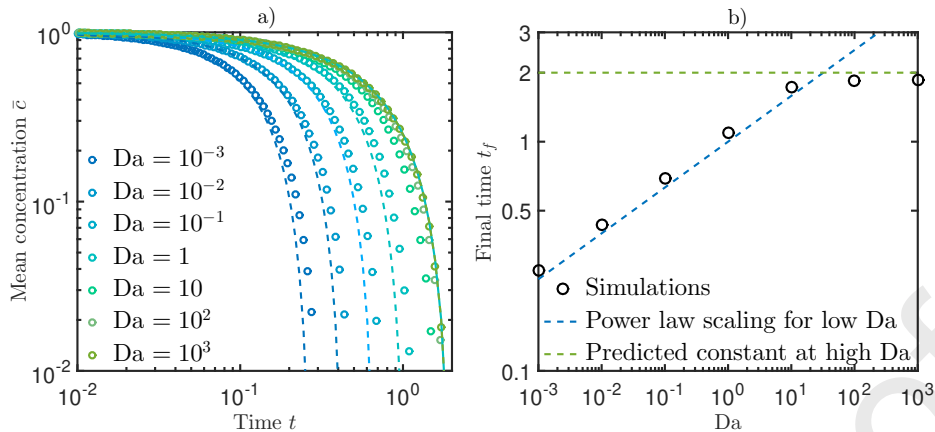


Figure 4: Effect of Damköhler on effective kinetics for $\beta = 0.5$, a) Average concentration as a function of time for several Damköhler numbers. Numerical results (dots) are compared to the analytical solutions of Eq. (B.2) (dashed lines). The batch solution is shown as a continuous line. b) Time t_f at which the mean concentration reaches zero as a function of Damköhler number. Black circles represents simulations, dashed lines represents the analytical predictions of Eq. (19) for low Damköhler numbers and Eq. (20) for high Damköhler number.

329 For high Damköhler numbers, two regimes occur (Fig. 8). The first regime, for $t < Da$, follows
 330 the batch kinetics (Appendix B.2.1). In the second regime, for $t > Da$, (Appendix B.2.2), the
 331 effective kinetics follow the same power law behavior as for low Damköhler number (Fig. 5.a)
 332 defined by Eq. (22).

333 These predictions are consistent with numerical simulations for all Damköhler numbers (Fig. 5.a)
 334 and all local reaction order β (Fig. 5.b). For low to intermediate Damköhler numbers, the ef-
 335 fective kinetics follow the predicted power law kinetics, characterized by the effective reaction
 336 order $\tilde{\beta}$ for the full range of concentrations (Fig. 5.b). For large Damköhler numbers (green dots
 337 in Fig. 5.a) the effective kinetic shows two regimes: a first regime following the batch kinetics
 338 given by Eq. (1) and a second power law regime given by Eq. (22). The difference between the
 339 effective and local reaction orders is largest for large reaction orders (Fig. 6). For $\beta = 1.5$, the
 340 effective order $\tilde{\beta} = 1.7$ is relatively close to the batch reaction order. Above $\beta = 1.5$, the effective
 341 order increases rapidly and is equal to $\tilde{\beta} = 3$ for $\beta = 2$. As β tends to 3, the deviation between
 342 the effective reaction order and the batch reaction order can become very large as the effective
 343 reaction order tends to infinity (Fig. 6).

344 3.3 Reaction order $\beta \geq 3$

345 For $\beta \geq 3$, the pulse reaction is much less efficient compared to a batch reactor, in the sense that
 346 the average reaction rate is smaller than in batch conditions for a given average concentration.
 347 For $\beta > 3$, dilution slows down the reaction so that the average concentration does not reach zero
 348 but converges to an asymptotic minimum value \bar{c}_∞ (Fig. 7). For $\beta = 3$, the average concentration
 349 decays to zero logarithmically as $t \rightarrow \infty$ (Appendix B.1, Eq. (B.3)). Note that this behavior
 350 differs fundamentally from the lower reaction orders discussed above, for which the reaction rate
 351 is always larger than zero and there is no residual concentration, except for $Da = 0$.

352 For low Damköhler numbers, the solution for the evolution of the mean concentration (Ap-

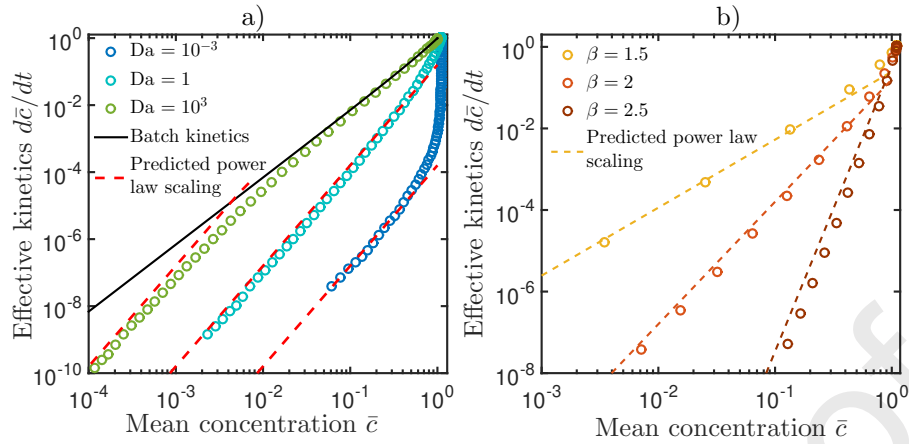


Figure 5: Effective kinetics in terms of mean concentration, a) $\beta = 2$, for Low, intermediate and high Da numbers, b) $Da = 1$ for different β in the range $1 < \beta < 3$. Numerical results (dots) are compared to analytical solutions (dashed lines). The power law behavior predicted by Eq. (22) is shown as a dashed line.

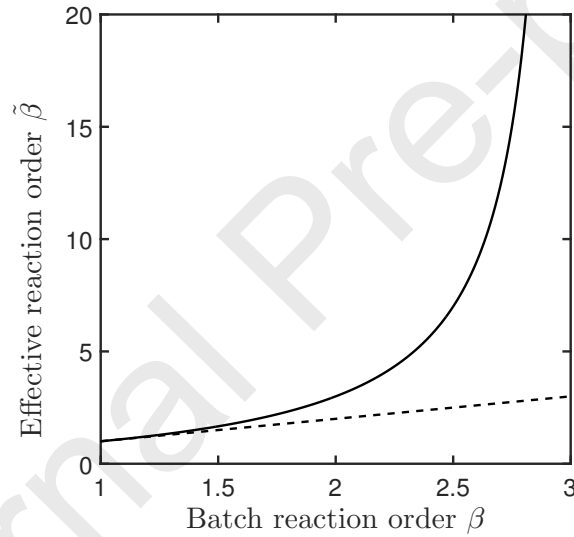


Figure 6: Effective reaction order $\tilde{\beta}$ predicted by Eq. (23) as a function of the batch reaction order for $1 < \beta < 3$ (solid line). The dashed line represents $\tilde{\beta} = \beta$.

pendix B.1, Eq. (B.2)) leads for $\beta > 3$ to an asymptotic value \bar{c}_∞ such that (Eq. (B.5))

$$1 - \bar{c}_\infty \sim Da. \quad (24)$$

As Da tends to zero, the asymptotic residual mean concentration tends to one (Fig. 7), which highlights the inhibiting effect of dilution on mass evolution for $\beta > 3$.

For high Damköhler numbers, the asymptotic residual mean concentration occurs in the

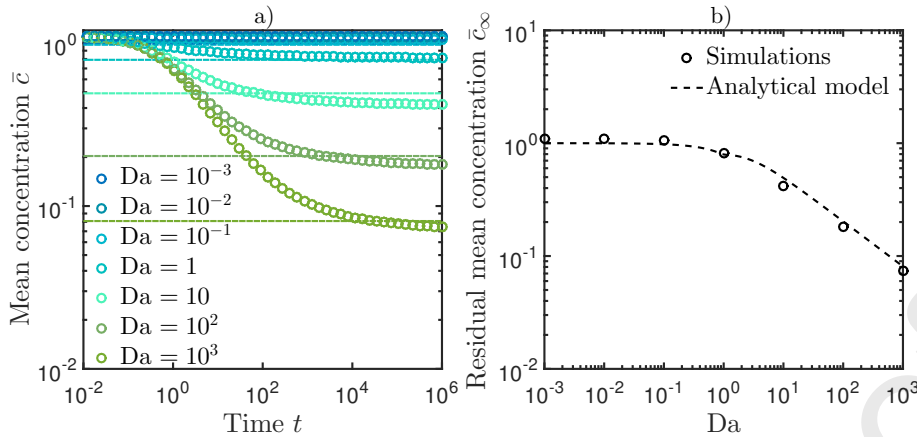


Figure 7: Effect of Damköhler on effective kinetics for $\beta = 3.5$, a) Numerical simulations (circles) as a function of time for different Damköhler number. Analytical model predictions for the asymptotic residual concentration are shown as dashed lines. b) Asymptotic residual mean concentration as a function of Damköhler number. Black circles represents simulations, the dashed black line represents the analytical model corresponding to Eq. (B.5) in Appendix B for low Damköhler numbers and to Eq. (25) for high Damköhler numbers.

357 second regime, leading to an asymptotic minimum value (Appendix B.2.2, Eq. (B.21))

$$\bar{c}_\infty \sim Da^{-\frac{1}{\beta-1}}, \quad (25)$$

358 which again quantifies the inhibiting effect of dilution on reaction as Da increases. These ana-
 359 lytical results closely match numerical simulations (Fig. 7.b).

360 4 Discussion

361 Our findings demonstrate that chemical gradients alter effective reactive kinetics through the
 362 coupling of diffusion and nonlinear reactions. By investigating the evolution of reactive so-
 363 lute pulses, as a paradigm for chemical gradients that evolve over space and time, we have
 364 uncovered a diverse spectrum of effective kinetic dynamics that depend on (1) the reaction non-
 365 linearity (reaction order β) and (2) the relative importance of reaction and dilution quantified
 366 by the Damköhler number Da . A central conclusion of our study is that dynamic chemical
 367 gradients not only change the magnitude of the effective kinetic coefficient but also change the
 368 nature of the non-linearity compared to the local kinetics. This result is in contrast with previ-
 369 ous studies that have studied how diffusive limitation, physical and geochemical heterogeneities
 370 (e.g. Soulaire et al., 2017; Wen and Li, 2017b; Deng et al., 2018), alter the effective kinetic co-
 371 efficients, while keeping the same effective kinetic laws

372 4.1

373 as the local kinetics. While we have focused on simplified reaction kinetics to quantify and
 374 formalize this mechanism, these dynamics are expected to impact a large range of geochemical

375 systems where they are coupled to other processes. In the following, we discuss the relevance
 376 to common classes of biogeochemical reactions based on a synthesis of the results discussed
 377 above. Subsequently, we provide an example for a mineral dissolution reactions where rate
 378 discrepancies are commonly observed. However, the approach is also applicable to other types
 379 of reactions, including redox, precipitation, complexation and adsorption reactions, as discussed
 380 in the following section.

381 4.1 Characteristic persistence time of reactive pulses

382 To illustrate the consequences of the derived effective kinetics across a broad range of β and Da ,
 383 we calculate the persistence time of reactive pulses that quantifies a characteristic time for the
 384 decay of the pulse mass under the effect of reaction. We define this time as the time required
 385 for the pulse mass to reach a given fraction of the initial mass. To compare with the batch
 386 reactor, we divide it by the time it would take for a batch reactor to reach the same fraction of
 387 the initial mass. This normalized persistence time t_c is shown in Fig. 8 as a function of β and
 388 Da . We have taken here the fraction of the initial mass to calculate this time to be equal to
 389 1%. Qualitatively similar results are obtained for other fractions. We have considered the full
 390 range of Damköhler numbers, from $Da = 10^{-3}$ (fast dilution compared to reaction) to $Da = 10^3$
 391 (fast reaction compared to dilution). This covers a range of characteristic reaction times, that
 392 vary broadly depending on the type of reaction, and of transport time scales, which depend on
 393 the pulse size and species diffusion coefficient (Eq. (9)).

394 On the left-hand side of Fig. 8, for $\beta < 1$, reactants disappear on the order of ten times faster
 395 than in the batch in the low Damköhler range, which is consistent with the analytical estimate
 396 of t_f (Fig. 4). For $1 < \beta < 3$, the characteristic persistence time increases sharply with the
 397 non-linear reaction order β , reaching several orders of magnitude increase. This is due to the
 398 emergence of effective reaction orders $\tilde{\beta}$ that become much larger than the batch reaction order
 399 for increasing β (Fig. 6). Within the grey zone, for $\beta > 3$, residual mass persists indefinitely
 400 and the characteristic persistence time tends to infinity. Collectively, these findings imply that
 401 when concentration fields are heterogeneous the commonly used approach of coupling residence
 402 time to batch kinetics may underestimate/overestimate the persistence of reactants by orders of
 403 magnitude.

404 4.2

405 Our main analytical findings in the different quadrants of Fig. 8 provide a framework for
 406 assessing the impact of concentration gradients on effective kinetics for a given type of reaction,
 407 as discussed below.

408 4.2 Geochemical relevance of effective kinetics

409 Our results are strictly valid when the concentration of one element is spatially variable and
 410 the others are in excess in the fluid or in the mineral phase. This simplification isolates and
 411 formalizes the impact of transient concentration gradients on upscaled kinetics. In complex
 412 multi-component reactive system, this effect will act together with other known mechanisms,
 413 such as geochemical and physical heterogeneities, as well as multiple reactions. Although other
 414 processes will also contribute to the effective kinetics, we argue that the new phenomena described
 415 here will likely have a major contribution as it can alter reaction rates over orders of magnitude
 416 and modify the effective orders of reaction. For single step reactions, the reaction order β with
 417 respect to a given chemical species is equal to its stoichiometric coefficient. However, most

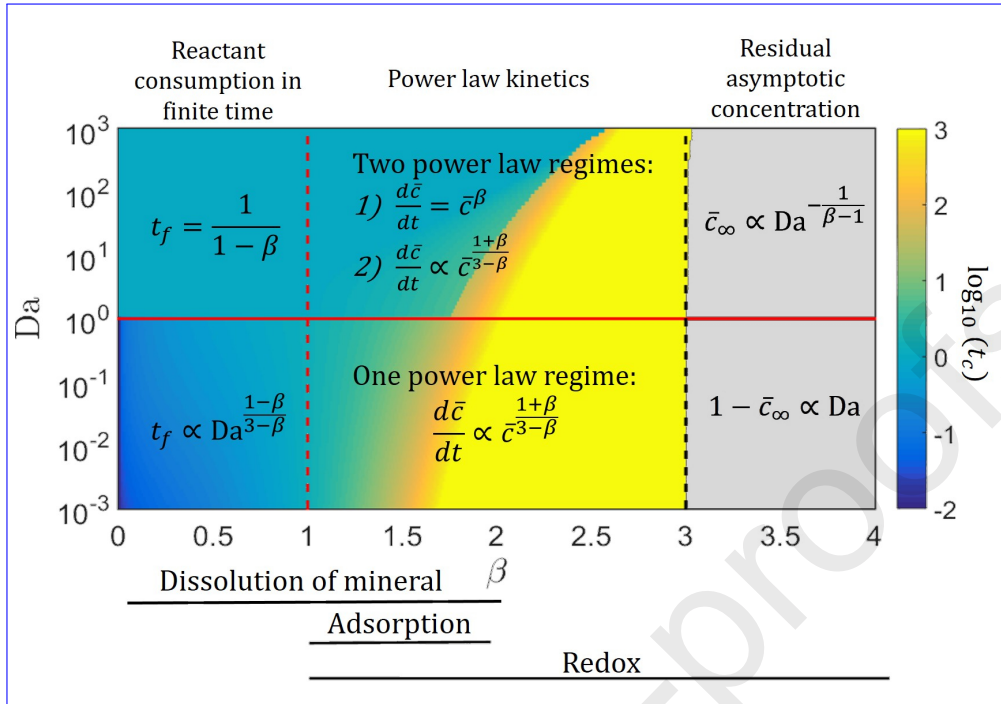


Figure 8: (Da, β) phase diagram of characteristic persistence time t_c and synthesis of main analytical results. The solid red line represents $Da = 1$. The dashed red and black lines correspond respectively to $\beta = 1$ and $\beta = 3$. The color scale represents the time t_c needed for the mean concentration to reach 1% of initial mean concentration for the reactive pulses, normalized by the same time for the batch reactor. The main reaction enhancement occurs for $\beta < 1$ and $Da < 1$ (blue area) while the effective reaction rate is strongly slowed down for $\beta > 1.5$ (yellow area). For $\beta > 3$, residual mass persists indefinitely and the characteristic persistence time may never be reached if the residual mass is larger than 1% (grey area). The typical range of effective reaction orders β for mineral dissolution, adsorption and redox reactions are indicated at the bottom.

418 biogeochemical reactions are complex multi-step reactions such that the rate-limiting step is
 419 unknown and hence most reaction orders are determined empirically and may range from 0 to
 420 5.

421 The lower left hand side of Fig. 8 would be typical of silicate mineral dissolution where
 422 reactions involve multiple steps that can be effectively described by an adaptation of transition
 423 state theory (Aagaard and Helgeson, 1982; Lasaga et al., 1994; Steefel and Lasaga, 1994):

$$r = k \prod_{i=1}^N a_i^n \left(1 - \frac{Q}{K_{eq}}\right)^m, \quad (26)$$

424 where r is the overall rate, k is the

425 intrinsic kinetic constant, a_i the ion activity, N the number of species, Q the ion activity
 426 product for the mineral-water reaction, and K_{eq} the corresponding equilibrium constant. The em-
 427 pirical exponents n and m introduce a non-linearity of the reaction rate with respect to the species
 428 concentration (Hellmann and Tisserand, 2006). Far from equilibrium, $Q \gg K_{eq}$ or $Q \ll K_{eq}$,
 429 and when a single species is limiting, equation (26) can be written as the simplified non-linear ki-
 430 netics that we consider (equation (1)), with $\beta = n$. Effective reaction orders estimated from labo-

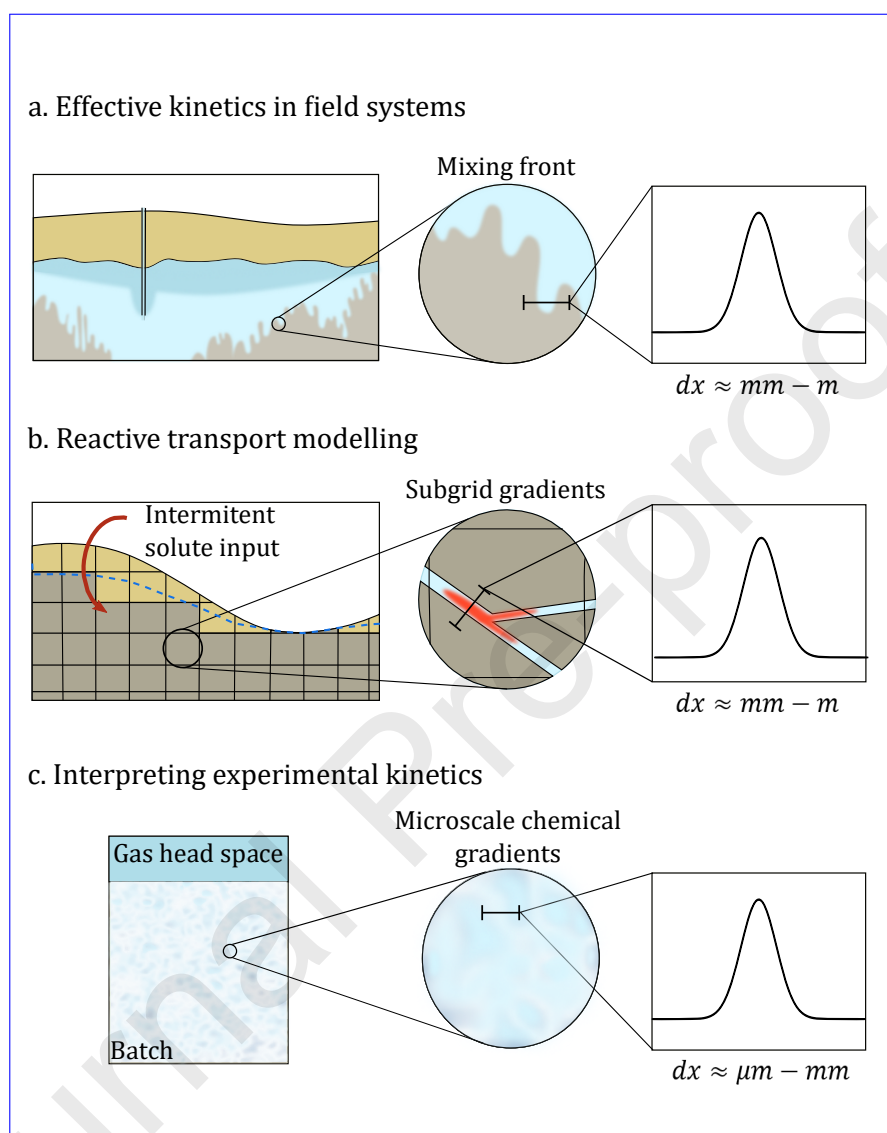


Figure 9: Illustration of different applications where unresolved chemical gradients may alter effective kinetics. a. Effective kinetics in field systems, such as CO_2 injection in the subsurface, where reactive pulses develop in mixing fronts. b. Reactive transport modeling, where subgrid chemical gradients cannot be resolved in models. c. Interpreting experimental kinetics in unmixed batches, where microscale chemical gradients can affect measured kinetics. The typical scales of expected chemical gradients for these applications is indicated as dx . Update the order of subfigures to match new order of section 5.

431 ratory experiments and typically range from $\beta = 0.1$ to 2 (Plummer and Wigley, 1976; Palandri and Kharaka, 2004)
 432 . Such mineral dissolution reactions are typically slow and therefore correspond to the low Da
 433 range. The upper right-hand side region of Fig. 8 may be typical of redox reactions. Metal redox
 434 reactions are typically characterized by $1 \leq \beta \leq 4$, while other redox reactions tend to have lower
 435 orders $1 \leq \beta \leq 2$ (Bethke, 1996). Redox reactions involving organic matter may have orders as
 436 high as $\beta = 5$ (Bleam, 2017). In the middle region of Fig. 8, where t_c transitions rapidly, adsorp-
 437 tion kinetics may be particularly susceptible to the effects observed here. Adsorption reaction
 438 kinetics are generally modelled with first-order or

439 4.3

440 pseudo-second-order kinetics (Rudzinski and Plazinski, 2006; Wu et al., 2009; Robati, 2013; Moussout et al., 2018)
 441 , which correspond to $\beta = 1$ or $\beta = 2$, but higher reaction orders are also observed (Largitte and Pasquier, 2016)
 442 .

443 The first application of our findings is for understanding the behavior of reactive solutes in
 444 field systems (Fig. 9a). As illustrated in Fig. 1, concentration gradients in natural systems can be
 445 driven by a diverse set of processes, ranging from intermittent sources to physical heterogeneity.
 446 For a given transport time, the reaction efficiency may be much faster (for $\beta < 1$) and much
 447 slower (for $\beta > 1$) than anticipated from batch kinetics (Fig. 8). This could lead to a much
 448 deeper penetration of reactive pulses or to a much faster consumption of solutes.

450 4.3

451 A second application is reactive transport modelling; to capture the effect of concentration gradi-
 452 ents on reaction kinetics, reactive transport models should have a spatial resolution finer than the
 453 smallest scale of concentration gradients (Fig. 9 b). This is not possible for catchment scale ap-
 454 plications (e.g. Li et al., 2017) but it is also challenging for modeling column experiments because
 455 chemical gradients often persist at the microscale (Heyman et al., 2020). Hence, our findings may
 456 help defining effective kinetics that quantify the impact of subscale gradients in reactive transport
 457 models. A third application is the interpretation of biogeochemical kinetics measured in experi-
 458 mental systems that are not well mixed, i.e. where chemical gradients persist (Fig. 9c). Geochem-
 459 ical reactions occurring at high temperatures and pressures, such as those associated with geologic
 460 carbon storage (e.g. DePaolo and Cole, 2013; Jun et al., 2013; Beckingham et al., 2016; Beckingham et al., 2017)
 461 , are often studied using batch reactors, where a gas headspace of a constant volume is used to
 462 maintain a constant pressure (Giammar et al., 2005; Johnson et al., 2014). Depending on the
 463 experimental conditions, pressure vessels can be difficult to mix via rocking or internal stirring,
 464 and are often static. Hence, in the absence of mechanical mixing, chemical gradients of differ-
 465 ent origin may develop, including dissolved gas convection, transport limitations and spatially
 466 heterogeneous reaction rates.

467 4.3 Example of the oxidation of pyrite by a pulse of dissolved oxygen

468 To illustrate these effective kinetics for a specific geochemical system, we take the example of
 469 pyrite dissolution by a pulse of dissolved oxygen. The aqueous oxidation of pyrite by oxygen is
 470 an example of geochemical process studied with reactive transport models to address a range
 471 of problems, including aquifer storage and recovery (Lazareva et al., 2015), acid mine drainage

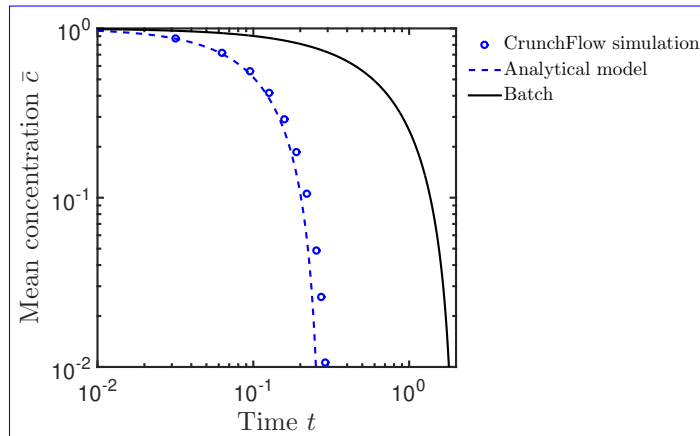
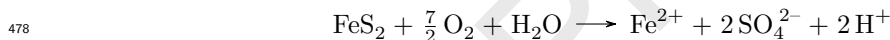


Figure 10: Simulation of pyrite dissolution by a pulse of dissolved oxygen for $Da = 10^{-3}$ ($\beta = 0.5$). Normalized mean concentration is shown as a function of normalized time, following the same definition as above. Results of the CrunchFlow simulation are shown as dots, the analytical model as a dashed line (Eq. B.2) and the batch model as a continuous line (Eq. B.11).

(Hubbard et al., 2009), and radioactive waste migration (Malmström et al., 2000; Yang et al., 2007). Intermittent release of dissolved oxygen, due to rainfall events or river stage variations (Fig. 1.a and 1.b), or flow heterogeneities (Fig. 1.e) often lead to small-scale dissolved oxygen gradients (Xu et al., 2000; Bochet et al., 2020) that are typically not resolved by reactive transport models. The reaction of oxidation of pyrite by oxygen can be written as

477 ,



479 Assuming that the other species are in excess, the kinetic rate law for pyrite oxidation by
480 oxygen may be written with respect to oxygen as (McKibben and Barnes, 1986)

$$481 \quad \frac{1}{3.5} \frac{dc_{\text{O}_2}}{dt} \approx -kc_{\text{O}_2}^{0.5}, \quad (27)$$

482 corresponding to $\beta = 0.5$.

483 For the geochemical system considered here, the kinetics of subscale unresolved oxygen pulses
484 would be faster than predicted by batch kinetics (Fig. 8). For instance, assuming a Damköhler
485 number of 10^{-4} , resulting from a kinetic rate constant of $6.6 \times 10^{-9} \text{ mol/m}^2/\text{s}$ (Yang et al.,
486 2007) and a diffusion coefficient of $10^{-9} \text{ mol/m}^2/\text{s}$ (Jung and Navarre-Sitchler, 2018a), dissolved
487 oxygen would be consumed 10 times faster than it would be in the well-mixed homogeneous
488 system. The more rapid release of both Fe^{2+} and trace metals typically associated with pyrite
489 (i.e., As, Pb, etc.) may have further implications for water quality. Although our results imply
490 that kinetic rates used in reactive transport models of systems with sub-grid scale concentrations
491 will be subject to additional uncertainty, our approach provides a concrete means of evaluating
492 the range of kinetic parameters to enable robust sensitivity analysis or uncertainty quantification
(e.g. Fenwick et al., 2014; Song et al., 2015).

493 We have verified that this geochemical system can be accurately modeled by our framework
494 under the considered assumptions (Fig. 10) using the multi-component reactive transport model
495 CrunchFlow (Steeffel et al., 2015). We first consider the case of a single pulse. The system
496 is composed of pyrite with a porosity of 30% and dissolution kinetic constant $k = 10^{-8.31}$

Table 1: Initial and injection chemistry used in CrunchFlow simulations for a single pulse, pyrite dissolution

Species	Initial condition (mol/L)	Injection condition (mol/L)
Fe ²⁺	10 ⁻⁸	10 ⁻⁸
H ⁺	10 ⁻⁴	10 ⁻⁴
O _{2,aq}	10 ⁻¹¹	10 ⁻⁴
SO ₄ ²⁻	10 ⁻⁸	10 ⁻⁸
Cl ⁻	Equilibrates charge	Equilibrates charge

497 m mol⁻¹ s⁻¹ (Yang et al., 2007). The considered solute species are O_{2,aq}, Fe²⁺, SO₄²⁻, and
 498 H⁺. For the initial condition in the domain prior to injection, the species concentrations are
 499 $c_{O_2} = 10^{-11}$ mol/L, $c_{Fe^{2+}} = 10^{-8}$ mol/L, $c_{SO_4^{2-}} = 10^{-8}$ mol/L, and pH is 4. Chloride is
 500 designated as the charge balancing ion to maintain electroneutrality. In the injected pulse,
 501 concentrations are the same as in the domain except for the oxygen concentration is set as
 502 $c_0 = 10^{-4}$ mol/L (Bochet et al., 2020, Table 1). The simulations were performed at 25°C with a
 503 diffusion coefficient of 10⁻⁷ m² s⁻¹ (Elberling et al., 1994), leading to Da = 10⁻³ (Table 2). The
 504 CrunchFlow simulation is in good agreement with the analytical model (Fig. 10). As predicted,
 505 the average concentration reaches zero much faster than the batch.

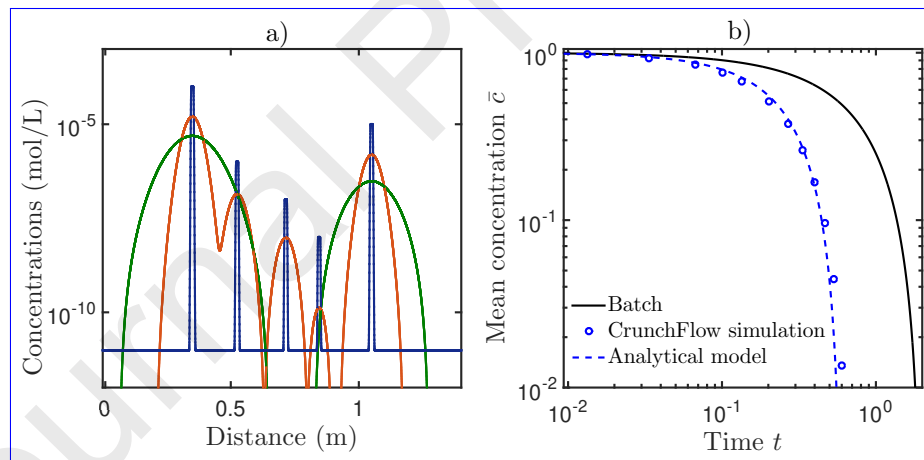
506 In order to evaluate the effect of a non-ideal concentration profile, we performed a CrunchFlow
 507 simulation with five irregularly spaced pulse injections of width 10⁻² m each, with different initial
 508 oxygen concentrations ($\log(c_{O_2}) = -4, -5, -6, -7, -8$) (Table 2). The initial conditions
 509 are the same as in the single pulse case (Table 1) and all the injected concentrations except
 510 oxygen are the same as in the background domain. The equivalent batch is defined with initial
 511 concentration equal to the mean of the pulse initial concentrations. The parameters are adapted
 512 to the single-pulse analytical model with an equivalent pulse width equal to the sum of the
 513 pulse widths, and an equivalent initial concentration set as the mean of injection concentrations,
 514 resulting in Da = 5 10⁻² (Table 2). In this case, the match with the analytical prediction remains
 515 excellent (Fig. 11) even though the concentration distribution is more complex than assumed in
 516 the analytical derivations.

517 5 Conclusions

518 The effective kinetics of reactive pulses reveal a rich diversity of behaviors driven by the interplay
 519 between dilution and non-linear reaction (Fig. 8). In the presence of concentration gradients,
 520 diffusion acts to redistribute mass towards lower concentrations, which, when coupled with non-
 521 linear reactions, can either enhance or inhibit the reaction efficiency depending on the local
 522 reaction order. We have derived approximate analytical solutions that capture these reactive
 523 dynamics and predict the different effective kinetic laws as a function of Damköhler number and
 524 the reaction order, which are representative of a range of reactive transport systems (Fig. 1, 8
 525 and 9). An important consequence of our results is the emergence of new effective kinetic laws
 526 characterized by upscaled orders that can be very different from those of the local kinetics. The
 527 coupling of transient concentration gradients and non-linear reactions hence leads to effective

Table 2: Parameters of the analytical model for the pyrite dissolution case.

Parameter	w_0	D	c_0	ν	k	A	Φ	τ_D	τ_R	Da
Unit	m	m ² /s	mol/L	[-]	[unit]	m ² /m ³	[-]	[-]	[-]	[-]
Single pulse $\beta = 0.5$	10^{-2}	10^{-7a}	10^{-4b}	3.5	$4.8 \cdot 10^{-9c}$	350	0.3	$1.6 \cdot 10^{-5}$	$1.6 \cdot 10^{-2}$	10^{-3}
Several pulses $\beta = 0.5$	10^{-2}	10^{-7}	10^{-4} 10^{-5} 10^{-6} 10^{-7} 10^{-8}	3.5	$4.8 \cdot 10^{-9}$	350	0.3	$4 \cdot 10^{-4}$	$7.5 \cdot 10^{-3}$	$5 \cdot 10^{-2}$

^a(Elberling et al., 1994)^b(Bochet et al., 2020)^c(Yang et al., 2007)**Figure 11:** Simulation of pyrite dissolution by multiple pulses of dissolved oxygen ($\beta = 0.5$). Five pulses with different initial concentrations and irregularly spaced are injected in the domain. a) is the concentration profile in space at normalized time $t \approx 10^{-5}$ (blue), $t \approx 10^{-2}$ (orange), $t \approx 10^{-1}$ (green). b) the normalized mean concentration as a function of normalized time for the CrunchFlow simulation (dots), an equivalent batch system (with initial concentration equal to the mean of injected concentrations Eq. (B.11), continuous line), and an equivalent analytical model (considering one pulse with initial concentration equal to the mean of injected concentrations, Eq. (B.2), dashed line), thus corresponding to $Da = 5 \cdot 10^{-2}$.

528 kinetics that can be much more non-linear than the batch kinetics (Fig. 6).

529 To isolate this mechanism and derive approximate analytical solutions for the effective ki-
530 netics, we considered here the idealized case of reactive pulses evolving through diffusion and
531 reaction. In complex natural reaction networks, this effect acts together with a range of other
532 processes and therefore it is difficult to understand and quantify. Other important phenomenon
533 known to impact the effective kinetics include the limited access of solutes to reactive surfaces
534 and mixing limitations, due to physical and geochemical heterogeneity at the pore or Darcy scale
535 (Molins et al., 2014; Beckingham et al., 2017; Wen and Li, 2018; Jung and Navarre-Sitchler, 2018a; Valocchi et al., 2018).
536 . In multi-components systems, our results are strictly valid when one element is varying in space
537 and time and the others are in excess. In natural systems several elements may be spatially vari-
538 able and react with different orders leading to more complex behaviour. However, since the
539 effect that we have uncovered leads to orders of magnitude differences between batch and effec-
540 tive reaction rates, it is likely playing a major, and so far unappreciated, role in multi-component
541 systems.

542 Although we explicitly solve the system for the ideal case of pulses, our general findings are
543 expected to apply qualitatively to different types of concentration landscapes. Indeed, in the
544 presence of concentration inhomogeneities, induced by intermittent reactant release or physical
545 heterogeneity (Fig. 1), diffusion tends to redistribute mass towards lower concentrations, which
546 leads to reaction enhancement or inhibition depending on the local reaction order β as described
547 here. The derived analytical framework is an essential step to integrate a range of biogeo-
548 chemical reactions in new mixing theories that describe the statistics of concentration gradients
549 (Le Borgne et al., 2017). The lamella mixing theory was successfully used to predict the up-
550 scaled kinetics of mixing-driven reactions at pore scale (De Anna et al., 2014b) and Darcy scale
551 (Le Borgne et al., 2014; Bandopadhyay et al., 2018) by coupling the one-dimensional compression-
552 diffusion equation transverse to stretched solute lamellae with bi-molecular reactions in the fluid
553 phase. By solving explicitly the coupling of diffusion and non-linear reactions, the method pre-
554 sented here resolves the main difficulty for the development of a reactive lamella framework to
555 upscale the effective kinetics of a range of non-linear reactions under incomplete mixing condi-
556 tions, including fluid-solid reactions.

557 These findings would thus be useful to interpret the result of reactive experiments in which
558 subscale chemical gradients develop due to poor mixing. These analytical results may also be
559 used to guide reactive transport models that cannot fully resolve the scale of concentration gra-
560 dients, which occurs in many reactive transport problems. Finally, they provide a new framework
561 to understand the effect of concentration gradients on chemical reactions in field applications,
562 in particular to understand the possible longer/smaller persistent time or penetration length of
563 reactive solutes. These findings indeed suggest that the characteristic persistence time of bio-
564 geochemical pulses can differ by orders of magnitude from the predictions of models that couple
565 solute residence time with batch kinetics. Reactive pulses are consumed much faster when the
566 order of the reaction is less than one, whereas they persist for a much longer time when the order
567 of the reaction is larger than one. These effects are particularly important at low Damköhler
568 number i.e., for reactions that are slow compared to the characteristic diffusion time. For orders
569 of reaction larger than three, dilution slows down reaction to the point that a residual mass
570 persists asymptotically.

571 Acknowledgments

572 CLT and TLB gratefully acknowledge funding by the ERC under the project *ReactiveFronts*
573 648377. CLT would like to thank also l'Ecole des Docteurs de l'UBL, le Conseil Regional de

574 Bretagne and OZCAR-RI for supporting this work. TA is supported by a Marie Skłodowska
 575 Curie Individual Fellowship, under the project *ChemicalWalks* 792041. CB acknowledges funding
 576 from Region Bretagne and Rennes Metropole.

577 Appendix A Notations

578 We detail all notations used in the study in table 3.

579 Appendix B Analytical solutions

580 This appendix details the analytical derivations for effective kinetics under coupled diffusion and
 581 non-linear reactions based on the assumption of Gaussian distribution of the reactant (Eq. (13))
 582 for $t \gg Da$ and of negligible diffusion for $t \ll Da$. The validity of these assumptions is discussed
 583 in Appendix C. The cases of low and high Damköhler are detailed separately below.

584 B.1 Low Damköhler number

585 In the limit of low Da, diffusion quickly deforms the pulse into a Gaussian distribution (Eq. (13)),
 586 whose variance evolves diffusively (see Appendix C and Fig. C.3),

$$\sigma^2(t) \approx \frac{t + Da/12}{Da}, \quad (\text{B.1})$$

587 where we have set $\sigma^2(0) = 1/12$ to match the variance of the initial rectangular profile. Inserting
 588 Eq. (B.1) into (14), we obtain

$$M(t) = \left[M_i - \frac{2}{\sqrt{\beta}} \frac{1-\beta}{3-\beta} \left(\frac{2\pi}{Da} \right)^{\frac{1-\beta}{2}} \left[(t + Da)^{\frac{3-\beta}{2}} - Da^{\frac{3-\beta}{2}} \right] \right]^{\frac{1}{1-\beta}}, \quad (\text{B.2})$$

589 with the initial mass $M_i \approx M(0) = 1$. Note that for $\beta = 1, 3$ this solution is singular and is
 590 not valid. For linear kinetics, $\beta = 1$, the concentration profile is exactly Gaussian, and the total
 591 mass decays exponentially. For $\beta = 3$, combining Eq. (14) and Eq. (B.1), and carrying out the
 592 integration explicitly, we obtain

$$M_{\beta=3}(t) = \left[1 + \frac{Da}{\sqrt{3\pi^2}} \log \left(1 + \frac{12t}{Da} \right) \right]^{-1/2}, \quad (\text{B.3})$$

593 which decays to zero logarithmically as $t \rightarrow \infty$.

594 Since the average concentration is proportional to the total mass (equation (4)), the dimensionless
 595 average concentration is equal to the dimensionless mass, $\bar{c}(t) = M(t)$. When $\beta < 1$, the
 596 mass reaches zero in a finite time according to Eq. (B.2), given to leading order in Da by

$$t_f = \left(\frac{\sqrt{\beta}}{2} \frac{3-\beta}{1-\beta} \right)^{\frac{2}{3-\beta}} \left(\frac{Da}{2\pi} \right)^{\frac{1-\beta}{3-\beta}}. \quad (\text{B.4})$$

597 For $\beta > 3$, the mass converges from above to an asymptotic minimum value according to
 598 Eq. (B.2). To leading order in Da, this gives,

$$\bar{c}_\infty = 1 - \frac{2Da}{\sqrt{\beta}(\beta-3)(2\pi)^{\frac{\beta-1}{2}}}. \quad (\text{B.5})$$

Table 3: Definition of model parameters and units

Parameter	Definition	Units
r	Reaction rate	$\text{mol } L^{-d} T^{-1}$
c	Concentration	$\text{mol } L^{-d}$
c_0	Initial concentration	$\text{mol } L^{-d}$
\bar{c}	Mean concentration	$\text{mol } L^{-d}$
\bar{c}_∞	Normalized residual mean concentration, [-]	
β	non-linear power law exponent	[-]
$\tilde{\beta}$	Power law exponent of the effective kinetic	[-]
k	reaction rate constant	$\text{mol}^{1-\beta} L^{d(\beta-1)} T^{-1}$
D	Diffusion coefficient	$L^2 T^{-1}$
Da	Damköhler number	[-]
L	Characteristic length	L
M	Mass	kg
S	Reference surface	L^2
w_0	Initial width	L
σ	Normalized variance	[-]
t	Time, normalized time	$T, [-]$
t_c	Normalized persistence time	[-]
t_f	Normalized final time, $\beta < 1$	[-]
τ_D	Diffusion characteristic time	T
τ_R	Reaction characteristic time	T
u	Fluid velocity	$L T^{-1}$
V	Volume of the batch	L^3
x	Distance	$\text{mol } L^{-d} T^{-1}$

599 For $1 < \beta < 3$, Eq. (B.2) follows a power-law decay, which leads to the average concentration,

$$\bar{c}(t) \approx \sqrt{\frac{2\pi}{\text{Da}}} \left(\frac{\sqrt{\beta} 3 - \beta}{2 \beta - 1} \right)^{\frac{1}{\beta-1}} t^{-\frac{3-\beta}{2(\beta-1)}}, \quad (\text{B.6})$$

600 for $t \gg \text{Da}$.

601 Differentiating Eq. (B.6), we find

$$\frac{d}{dt} \bar{c}(t) = -\frac{3 - \beta}{2(\beta - 1)} \frac{\bar{c}(t)}{t}, \quad (\text{B.7})$$

602 Because the average concentration decreases monotonically, $\bar{c}(t)$ is invertible, Solving Eq. (B.6)
603 for time as a function of mean concentration, we have

$$t(\bar{c}) = \left(\frac{2\pi}{\text{Da}} \right)^{\frac{\beta-1}{3-\beta}} \left(\frac{\sqrt{\beta} 3 - \beta}{2 \beta - 1} \right)^{\frac{2}{3-\beta}} \bar{c}^{-\frac{2(\beta-1)}{3-\beta}}. \quad (\text{B.8})$$

604 Thus, the effective kinetics are given by

$$\frac{d}{dt} \bar{c}(t) = \beta^{-\frac{1}{3-\beta}} \left(\frac{\text{Da} \beta - 1}{\pi 3 - \beta} \right)^{\frac{\beta-1}{3-\beta}} \bar{c}^{\frac{1+\beta}{3-\beta}}. \quad (\text{B.9})$$

605 B.2 High Damköhler number

606 We now develop an approximate description for the behavior of the average concentration at
607 high Damköhler. This involves two different regimes.

608 B.2.1 First regime, $t \ll \text{Da}$

609 First, for times $t \ll \text{Da}$, diffusion has not had time to significantly deform the initial condition.
610 Thus, the average concentration evolves approximately according to the batch dynamics,

$$\frac{d\bar{c}(t)}{dt} = -\bar{c}(t)^\beta, \quad (\text{B.10})$$

611 and we obtain

$$\bar{c}(t) = [1 + (\beta - 1)t]^{-\frac{1}{\beta-1}}. \quad (\text{B.11})$$

612 For $\beta < 1$, the average concentration reaches zero during this regime at the time given by
613 Eq. (19).

614 B.2.2 Second regime, $t \gg \text{Da}$,

615 For $t > \text{Da}$, the spreading of the pulse by diffusion cannot be neglected. Rearranging Eqs. (14)
616 and (18), we obtain for the variance

$$\frac{d \log \sigma(t)}{dt} = \frac{1}{2\text{Da}\sigma^2(t)} - (\sqrt{\beta} - 1) \frac{d \log M(t)}{dt}. \quad (\text{B.12})$$

617 If the first term on the right hand side of Eq. (B.12) dominates compared to the second term, the
618 evolution of the variance is approximately diffusive. Otherwise, if the second term dominates,

619 the evolution of the variance is driven by the effect of reaction. Inserting Eq. (B.11) into (B.12),
 620 the condition for diffusion-dominated growth is thus

$$\sigma(t)^{3-\beta} M(t)^{\beta-1} < \frac{\sqrt{\beta}-1}{\sqrt{\beta}} \frac{(2\pi)^{\frac{\beta-1}{2}}}{2\text{Da}}. \quad (\text{B.13})$$

621 We start by evaluating this inequality at $t = \text{Da}$, which is the onset of this second regime.
 622 Since mass follows the batch dynamics in the first regime (Eq. (B.11)), at $t = \text{Da}$, it is given by

$$M(\text{Da}) = [1 + (\beta - 1)\text{Da}]^{-\frac{1}{\beta-1}}. \quad (\text{B.14})$$

623 We substitute Eq. (B.14) and $\sigma(\text{Da}) = 1/12$ (corresponding to the initial variance of a rectangular
 624 pulse, assumed not to change appreciably up to $t = \text{Da}$) in Eq. (B.13), which gives the condition
 625 for a dominant diffusive variance growth at $t = \text{Da}$,

$$\frac{2\text{Da}}{(2\pi)^{\frac{\beta-1}{2}}} \frac{\sqrt{\beta}-1}{\sqrt{\beta}} \frac{12^{-\frac{3-\beta}{2}}}{1 + (\beta - 1)\text{Da}} < 1. \quad (\text{B.15})$$

626 For a given β , the left hand side of Eq. (B.15) is largest for $\text{Da} \rightarrow \infty$. Therefore, if the criterion
 627 holds in this limit, it holds for all Da . In this limit, the condition is

$$\frac{2}{\sqrt{\beta}(\sqrt{\beta} + 1)(2\pi)^{\frac{\beta-1}{2}} 12^{\frac{3-\beta}{2}}} < 1. \quad (\text{B.16})$$

628 This holds for $\beta \lesssim 5$, as verified numerically. We focus on such β since higher β are not commonly
 629 encountered. Therefore, at $t = \text{Da}$, the variance growth is dominated by diffusion for the range
 630 of β that we consider, leading to a variance equal to

$$\sigma^2(t) \approx \sigma^2(\text{Da}) + \frac{t - \text{Da}}{\text{Da}}, \quad (\text{B.17})$$

631 with $\sigma^2(\text{Da}) = 1/12$, and a mass given by the same equation as for the low Da regime, with the
 632 initial mass $M_i \approx M(\text{Da})$, see Eq. (B.2). To test whether the criterion of diffusion dominated
 633 variance holds true at larger times, we substitute Eq. (B.17) and Eq. (B.2) in Eq. (B.13). This
 634 gives the criterion

$$\frac{2\text{Da}}{(2\pi)^{\frac{\beta-1}{2}}} \frac{\sqrt{\beta}-1}{\sqrt{\beta}} \frac{\left[\frac{1}{12} + \frac{t-\text{Da}}{\text{Da}}\right]^{\frac{3-\beta}{2}}}{M(\text{Da}) - \frac{2}{\sqrt{\beta}} \frac{1-\beta}{3-\beta} \left(\frac{2\pi}{\text{Da}}\right)^{\frac{1-\beta}{2}} \left[(t + \text{Da})^{\frac{3-\beta}{2}} - \text{Da}^{\frac{3-\beta}{2}}\right]} < 1. \quad (\text{B.18})$$

635 It can be verified numerically that this criterion holds true at all times. For $t \rightarrow \infty$, this simplifies
 636 into

$$\frac{3-\beta}{\sqrt{\beta}+1} < 1, \quad (\text{B.19})$$

637 which is always true for $\beta > 1$. Hence, the variance evolves diffusively at $t = \text{Da}$ and at all later
 638 times, and a regime with reaction-dominated variance growth is never observed. The accuracy
 639 of the growth of the variance according to Eq. (B.17) is discussed in Appendix C.

640 The effective kinetics can thus be derived as follows for different β . For $1 < \beta < 3$, the
 641 effective kinetics remain given by Eq. (B.9), and the average concentration by Eq. (B.6) with
 642 $M_i = M(\text{Da})$ (Eq. (B.14)). For $\beta > 3$, according to Eq. (B.11) after replacing the initial mass
 643 M_i by $M(\text{Da})$, the mass tends to an asymptotic constant value given by

$$M_\infty = \left[M(\text{Da}) + \text{Da} \frac{2}{\sqrt{\beta}} \frac{\beta-1}{\beta-3} (2\pi)^{-\frac{\beta-1}{2}} \right]^{-\frac{1}{\beta-1}}. \quad (\text{B.20})$$

644 At sufficiently large Da , we can neglect $M(Da)$ according to Eq. (B.14) because $Da^{-\frac{1}{\beta-1}} \ll Da$.
 645 Thus, we obtain the asymptotic value for the average concentration,

$$\bar{c}_\infty \approx Da^{-\frac{1}{\beta-1}} \sqrt{2\pi} \left(\frac{\sqrt{\beta} \beta - 3}{2 \beta - 1} \right)^{\frac{1}{\beta-1}}. \quad (\text{B.21})$$

646 Appendix C Hypothesis validation

647 In addition to the numerical validation of the analytical derivation for the effective kinetics,
 648 we further test the validity of the assumptions that we use in our analytical derivations. The
 649 Gaussian assumption and the variance growth assumptions are discussed separately below.

650 C.1 Gaussian assumption

651 Here we assess the validity of the Gaussian assumption for different Damköhler numbers at times
 652 corresponding to different regimes. As highlighted by Eq. (13), Gaussian distributions of different
 653 widths σ and maximum value c_{peak} collapse to a single curve when represented according to the
 654 normalized variables x/σ and c/c_{peak} . It is thus convenient to use this normalization to test the
 655 Gaussian assumption. Furthermore, Gaussian curves are uniquely characterized by the power
 656 law scaling

$$\log(c/c_{peak}) \sim (x/\sigma)^{-2}. \quad (\text{C.1})$$

657 Therefore, Gaussian distributions are characterized by a straight line of slope 2 when representing
 658 $\log(|\log(c/c_{peak})|)$ against $\log(|x/\sigma|)$. Hence, any deviation from this slope corresponds to a non-
 659 Gaussian profile.

660 In Fig. C.1, we test the Gaussian assumption in the case of $\beta = 2$ for low and high Damköhler
 661 numbers, respectively $Da = 10^{-3}$ and $Da = 10^3$. At low Da , diffusion acts over much smaller time
 662 scales than reaction, and the profiles are Gaussian at all times (Fig. C.1.a and c), consistently
 663 with the hypothesis of Appendix B.1. For high Da , the early time profiles are non Gaussian
 664 and close to the initial square injection (Fig. C.1.b and d). In this regime, we do not assume
 665 Gaussianity but instead the dominance of reaction over diffusion (Appendix B.2.1). At late
 666 times, $t \gg Da$, the profiles are very close to Gaussian (Fig. C.1.a and C.1.b) and closely follow
 667 the power law scaling of Eq. (C.1) (Fig. C.1.b and d), which is consistent with the assumption
 668 of Appendix B.2.2.

669 In Fig. C.2, we test the Gaussian assumption for the case of $\beta = 0.5$ for low Damköhler
 670 number, $Da = 10^{-3}$. We do not represent large Da in Figure C.2 because mass reaches zero
 671 before $t = Da$ in this case and only the first regime where we do not assume Gaussianity
 672 (Appendix B.2.1) is relevant. Again, consistently with the assumption of Appendix B.1, for low
 673 Da , the profiles are very close to Gaussian at all times (Fig. C.2.a) and closely follows the power
 674 law scaling of Eq. (C.1) (Fig. C.2.b). Results are similar for other reaction orders $\beta < 1$.

675 These results confirm the assumptions that we have made in Appendix B for deriving ap-
 676 proximated analytical solution for the evolution of concentration distributions. For $t \ll Da$, we
 677 do not assume that profiles are Gaussian but we assume that diffusion plays no role and that
 678 the evolution of concentration profiles is dominated by reaction alone. For small Da , this regime
 679 is very short and not considered here. For large Da , this regime is discussed in Appendix B.2.1.
 680 For $t \gg Da$, we assume that profiles are Gaussian, which is consistent with numerical simulations
 681 for all values of Da and β . This regime is discussed in Appendix B.1 and B.2.2.

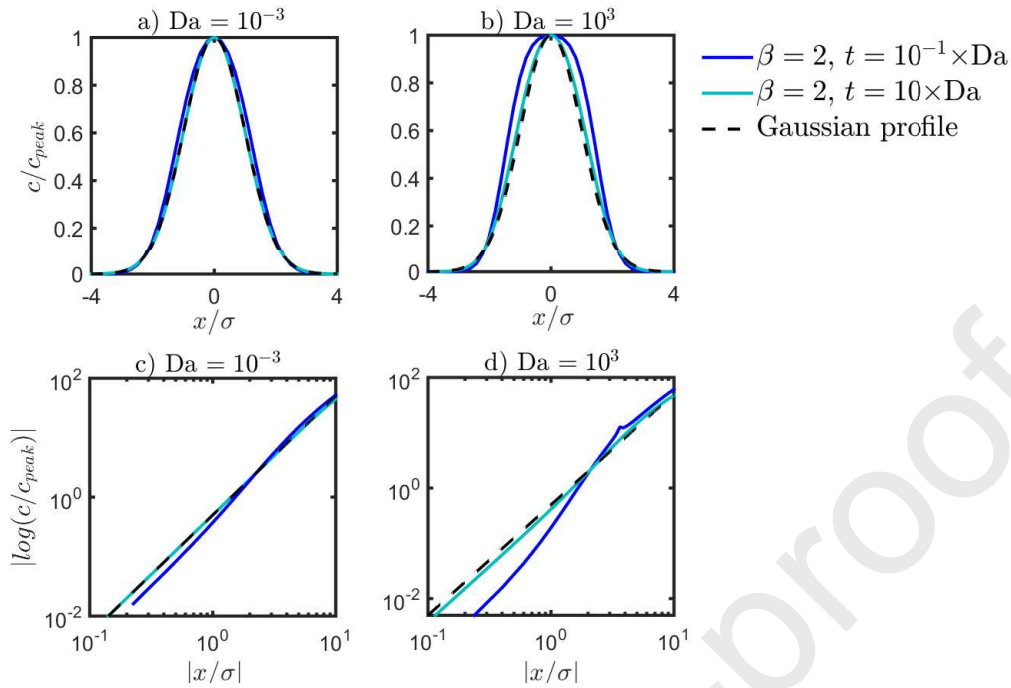


Figure C.1: Test of Gaussianity of reactive pulses from numerical simulations for $\beta = 2$. Comparison of reactive profiles, normalized by their peak values c_{peak} along the y axis and their standard deviation σ along the x axis, with Gaussian profiles at early and late times, respectively $t \approx 10^{-1} \times Da$ and $t \approx 10 \times Da$ for a) $Da = 10^{-3}$, and b) $Da = 10^3$. Test of Gaussian power law scaling (Eq. (C.1)) for the same cases respectively for c) low Da and d) high Da.

C.2 Variance growth assumption

Here, we assess the validity of the assumption that the evolution of the variance is dominated by the diffusion term in Eq. (B.12). This leads to the prediction that the variance is constant for $t \ll Da$ and grows diffusively for $t \gg Da$ following Eq. (B.1) for $Da \leq 1$ and Eq. (B.17) for $Da > 1$. We compare the variance growth in time obtained from numerical simulations with these predictions for different Damköhler numbers and β in Fig. C.3.

In all cases, simulations are found to be in good agreement with analytical solutions. Note that for $\beta < 1$, the variance computed from numerical simulations starts decreasing at the end of the simulations, which is not captured by our model (Fig. C.3, a). A short time before the whole profile reaches zero, concentrations on the sides are reacting faster than they diffuse so that the variance starts to decrease before the whole profile reaches zero. This regime of variance decay is thus very short.

6 Research data

Research Data associated with this article can be accessed at <https://doi.org/10.5281/zenodo.4114532>.

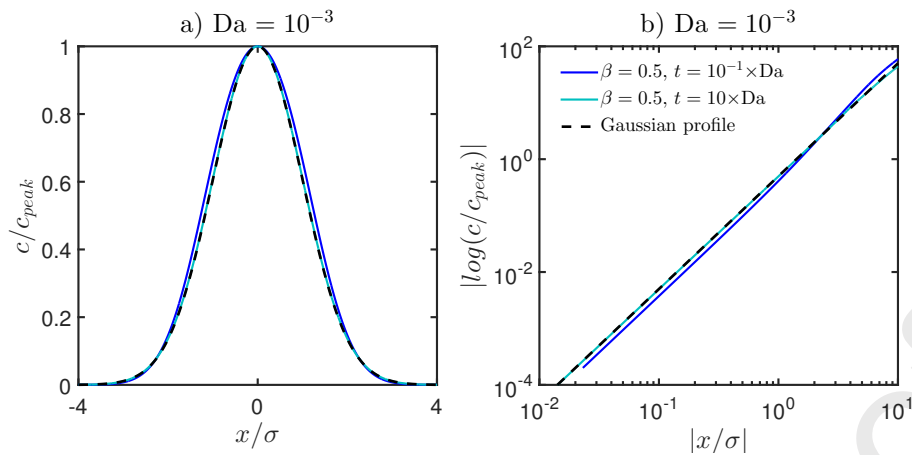


Figure C.2: Test of Gaussianity of reactive pulses from numerical simulations for $\beta = 0.5$. a) Comparison of reactive profiles, normalized by their peak values c_{peak} along the y axis and their standard deviation σ along the x axis, with Gaussian profiles at early and late times, $t \approx 10^{-1} \times Da$ and $t \approx 10 \times Da$ for $Da = 10^{-3}$. The high Da profile is not represented because the mean concentration reaches zero before the times at which we assume Gaussianity, $t = Da$. b) Test of Gaussian power law scaling represented by Eq. (C.1).

References

- 697
- 698 Aagaard, P. and H. C. Helgeson (1982). “Thermodynamic and kinetic constraints on reaction
699 rates among minerals and aqueous solutions; I, Theoretical considerations”. In: *American
700 journal of Science* 282.3, pp. 237–285.
- 701 Abel, C. D. T., S. K. Sharma, S. A. Mersha, and M. D. Kennedy (2014). “Influence of intermittent
702 infiltration of primary effluent on removal of suspended solids, bulk organic matter, nitrogen
703 and pathogens indicators in a simulated managed aquifer recharge system”. In: *Ecological
704 engineering* 64, pp. 100–107.
- 705 Al-Yamani, W., S. Green, R. Pangilinan, S. Dixon, S. A. Shahid, P. Kemp, and B. Clothier
706 (2019). “Water use of Al Samr (*Acacia tortilis*) forests irrigated with saline groundwater
707 and treated sewage effluent in the hyper-arid deserts of Abu Dhabi”. In: *Agricultural Water
708 Management* 216, pp. 361–364.
- 709 Atchley, A. L., R. M. Maxwell, and A. K. Navarre-Sitchler (2013). “Using streamlines to simulate
710 stochastic reactive transport in heterogeneous aquifers: Kinetic metal release and transport
711 in CO₂ impacted drinking water aquifers”. In: *Advances in water resources* 52, pp. 93–106.
- 712 Atchley, A. L., A. K. Navarre-Sitchler, and R. M. Maxwell (2014). “The effects of physical and
713 geochemical heterogeneities on hydro-geochemical transport and effective reaction rates”. In:
714 *Journal of contaminant hydrology* 165, pp. 53–64.
- 715 Bandopadhyay, A., P. Davy, and T. Le Borgne (2018). “Shear flows accelerate mixing dynamics
716 in hyporheic zones and hillslopes”. In: *Geophysical Research Letters* 45.21, pp. 11–659.
- 717 Battiato, I. and D. M. Tartakovsky (2011). “Applicability regimes for macroscopic models of
718 reactive transport in porous media”. In: *Journal of contaminant hydrology* 120, pp. 18–26.
- 719 Battiato, I., D. M. Tartakovsky, A. M. Tartakovsky, and T. Scheibe (2009). “On breakdown
720 of macroscopic models of mixing-controlled heterogeneous reactions in porous media”. In:
721 *Advances in water resources* 32.11, pp. 1664–1673.

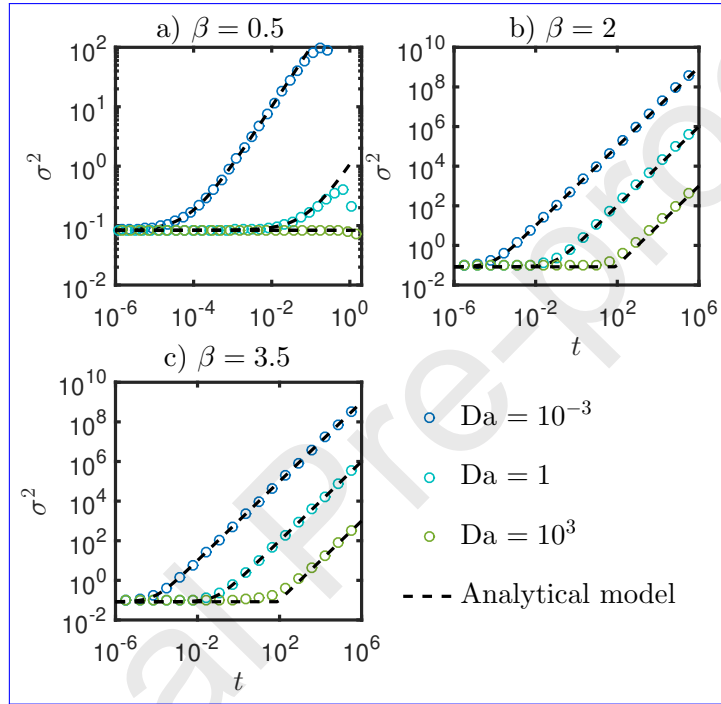


Figure C.3: Test of analytical model for variance growth. Temporal evolution of the reactive pulse variance for a) $\beta = 0.5$, b) $\beta = 2$, c) $\beta = 3.5$, and $Da = 0.001$ (blue circles), $Da = 1$ (turquoise circles), and $Da = 1000$ (green circles). The analytical model predictions, shown by black dashed lines, is given by Eq. (B.1) for $Da \leq 1$ and Eq. (B.17) for $Da \geq 1$

- 722 Beckingham, L. E., E. H. Mitnick, C. I. Steefel, S. Zhang, M. Voltolini, A. M. Swift, L. Yang,
723 D. R. Cole, J. M. Sheets, J. B. Ajo-Franklin, et al. (2016). “Evaluation of mineral reactive
724 surface area estimates for prediction of reactivity of a multi-mineral sediment”. In: *Geochimica
725 et Cosmochimica Acta* 188, pp. 310–329.
- 726 Beckingham, L. E., C. I. Steefel, A. M. Swift, M. Voltolini, L. Yang, L. M. Anovitz, J. M.
727 Sheets, D. R. Cole, T. J. Kneafsey, E. H. Mitnick, et al. (2017). “Evaluation of accessible
728 mineral surface areas for improved prediction of mineral reaction rates in porous media”. In:
729 *Geochimica et Cosmochimica Acta* 205, pp. 31–49.
- 730 Berkowitz, B., A. Cortis, M. Dentz, and H. Scher (2006). “Modeling non-Fickian transport in
731 geological formations as a continuous time random walk”. In: *Reviews of Geophysics* 44.2.
- 732 Bethke, C. (1996). *Geochemical reaction modeling: Concepts and applications*. Oxford University
733 Press on Demand.
- 734 Bleam, W. (2017). “Chapter 9-reduction-oxidation chemistry”. In: *Soil and Environmental Chem-
735 istry*, pp. 445–489.
- 736 Bochet, O., L. Bethencourt, A. Dufresne, J. Farasin, M. Pédrot, T. Labasque, E. Chatton, N.
737 Lavenant, C. Petton, B. W. Abbott, et al. (2020). “Iron-oxidizer hotspots formed by inter-
738 mittent oxic-anoxic fluid mixing in fractured rocks”. In: *Nature Geoscience* 13.2, pp. 149–
739 155.
- 740 Burté, L., C. A. Cravotta III, L. Bethencourt, J. Farasin, M. Pédrot, A. Dufresne, M.-F. Gerard,
741 C. Baranger, T. Le Borgne, and L. Aquilina (2019). “Kinetic study on clogging of a geother-
742 mal pumping well triggered by mixing-induced biogeochemical reactions”. In: *Environmental
743 science & technology* 53.10, pp. 5848–5857.
- 744 Datta, S., B. Mailloux, H.-B. Jung, M. A. Hoque, M. Stute, K. M. Ahmed, and Y. Zheng (2009).
745 “Redox trapping of arsenic during groundwater discharge in sediments from the Meghna river-
746 bank in Bangladesh”. In: *Proceedings of the National Academy of Sciences* 106.40, pp. 16930–
747 16935.
- 748 De Anna, P., J. Jimenez-Martinez, H. Tabuteau, R. Turuban, T. Le Borgne, M. Derrien, and
749 Y. Meheust (2014a). “Mixing and reaction kinetics in porous media: An experimental pore
750 scale quantification”. In: *Environmental Science and Technology* 48.1, pp. 508–516.
- 751 De Anna, P., M. Dentz, A. Tartakovsky, and T. Le Borgne (2014b). “The filamentary structure
752 of mixing fronts and its control on reaction kinetics in porous media flows”. In: *Geophysical
753 Research Letters* 41.13, pp. 4586–4593.
- 754 DePaolo, D. J. and D. R. Cole (2013). “Geochemistry of geologic carbon sequestration: an
755 overview”. In: *Reviews in Mineralogy and Geochemistry* 77.1, pp. 1–14.
- 756 Deng, H., S. Molins, D. Trebotich, C. Steefel, and D. DePaolo (2018). “Pore-scale numerical inves-
757 tigation of the impacts of surface roughness: Upscaling of reaction rates in rough fractures”.
758 In: *Geochimica et Cosmochimica Acta* 239, pp. 374–389.
- 759 Dentz, M., T. Le Borgne, A. Englert, and B. Bijeljic (2011a). “Mixing, spreading and reaction in
760 heterogeneous media: A brief review”. In: *Journal of contaminant hydrology* 120, pp. 1–17.
- 761 — (2011b). “Mixing, spreading and reaction in heterogeneous media: A brief review”. In: *Journal
762 of Contaminant Hydrology* 120-121, pp. 1–17.
- 763 Dutta, T., A. Carles-Brangarí, D. Fernández-García, S. Rubol, J. Tirado-Conde, and X. Sanchez-
764 Vila (2015). “Vadose zone oxygen (O₂) dynamics during drying and wetting cycles: an arti-
765 ficial recharge laboratory experiment”. In: *Journal of Hydrology* 527, pp. 151–159.
- 766 Elberling, B., R. Nicholson, and J. Scharer (1994). “A combined kinetic and diffusion model for
767 pyrite oxidation in tailings: a change in controls with time”. In: *Journal of Hydrology* 157.1-4,
768 pp. 47–60.

- 769 Fenwick, D., C. Scheidt, and J. Caers (2014). “Quantifying asymmetric parameter interactions
770 in sensitivity analysis: application to reservoir modeling”. In: *Mathematical Geosciences* 46.4,
771 pp. 493–511.
- 772 Giammar, D. E., R. G. Bruant Jr, and C. A. Peters (2005). “Forsterite dissolution and magnesite
773 precipitation at conditions relevant for deep saline aquifer storage and sequestration of carbon
774 dioxide”. In: *Chemical Geology* 217.3-4, pp. 257–276.
- 775 Gramling, C. M., C. F. Harvey, and L. C. Meigs (2002). “Reactive transport in porous media:
776 A comparison of model prediction with laboratory visualization”. In: *Environmental science
777 & technology* 36.11, pp. 2508–2514.
- 778 Guo, J., M. Quintard, and F. Laouafa (2015). “Dispersion in porous media with heterogeneous
779 nonlinear reactions”. In: *Transport in Porous Media* 109.3, pp. 541–570.
- 780 Hellmann, R. and D. Tisserand (2006). “Dissolution kinetics as a function of the Gibbs free energy
781 of reaction: An experimental study based on albite feldspar”. In: *Geochimica et Cosmochimica
782 Acta* 70.2, pp. 364–383.
- 783 Hermans, T., F. Nguyen, M. Klepikova, A. Dassargues, and J. Caers (2018). “Uncertainty
784 quantification of medium-term heat storage from short-term geophysical experiments using
785 Bayesian evidential learning”. In: *Water Resources Research* 54.4, pp. 2931–2948.
- 786 Heyman, J., D. R. Lester, R. Turuban, Y. Méheust, and T. Le Borgne (2020). “Stretching and
787 folding sustain microscale chemical gradients in porous media”. In: *Proceedings of the National
788 Academy of Sciences*.
- 789 Hinsinger, P., C. Plassard, C. Tang, and B. Jaillard (2003). “Origins of root-mediated pH changes
790 in the rhizosphere and their responses to environmental constraints: a review”. In: *Plant and
791 soil* 248.1-2, pp. 43–59.
- 792 Hubbard, C. G., S. Black, and M. L. Coleman (2009). “Aqueous geochemistry and oxygen isotope
793 compositions of acid mine drainage from the Río Tinto, SW Spain, highlight inconsistencies
794 in current models”. In: *Chemical Geology* 265.3-4, pp. 321–334.
- 795 Hubert, A., T. Aquino, H. Tabuteau, Y. Méheust, and T. Le Borgne (2020). “Enhanced and non-
796 monotonic effective kinetics of solute pulses under Michaelis–Menten reactions”. In: *Advances
797 in Water Resources* 146, p. 103739.
- 798 Johnson, N. C., B. Thomas, K. Maher, R. J. Rosenbauer, D. Bird, and G. E. Brown Jr (2014).
799 “Olivine dissolution and carbonation under conditions relevant for in situ carbon storage”.
800 In: *Chemical Geology* 373, pp. 93–105.
- 801 Jun, Y.-S., D. E. Giammar, and C. J. Werth (2013). *Impacts of geochemical reactions on geologic
802 carbon sequestration*.
- 803 Jung, H. and A. Navarre-Sitchler (2018a). “Physical heterogeneity control on effective mineral
804 dissolution rates”. In: *Geochimica et Cosmochimica Acta* 227, pp. 246–263.
- 805 — (2018b). “Scale effect on the time dependence of mineral dissolution rates in physically het-
806 erogeneous porous media”. In: *Geochimica et Cosmochimica Acta* 234, pp. 70–83.
- 807 Keiluweit, M., P. S. Nico, M. Kleber, and S. Fendorf (2016). “Are oxygen limitations under
808 recognized regulators of organic carbon turnover in upland soils?” In: *Biogeochemistry* 127.2,
809 pp. 157–171.
- 810 Kirchner, J. W. and C. Neal (2013). “Universal fractal scaling in stream chemistry and its
811 implications for solute transport and water quality trend detection”. In: *Proceedings of the
812 National Academy of Sciences* 110.30, pp. 12213–12218.
- 813 Kitanidis, P. K. (1994). “The concept of the dilution index”. In: *Water resources research* 30.7,
814 pp. 2011–2026.
- 815 Kitanidis, P. K. and P. L. McCarty (2012). *Delivery and Mixing in the Subsurface: Processes and
816 Design Principles for In Situ Remediation*. Vol. 4. Springer Science & Business Media.

- 817 Largette, L. and R. Pasquier (2016). “A review of the kinetics adsorption models and their
818 application to the adsorption of lead by an activated carbon”. In: *Chemical Engineering*
819 *Research and Design* 109, pp. 495–504.
- 820 Lasaga, A. C., J. M. Soler, J. Ganor, T. E. Burch, and K. L. Nagy (1994). “Chemical weather-
821 ing rate laws and global geochemical cycles”. In: *Geochimica et Cosmochimica Acta* 58.10,
822 pp. 2361–2386.
- 823 Lazareva, O., G. Druschel, and T. Pichler (2015). “Understanding arsenic behavior in carbonate
824 aquifers: Implications for aquifer storage and recovery (ASR)”. In: *Applied Geochemistry* 52,
825 pp. 57–66.
- 826 Le Borgne, T., M. Dentz, and E. Villiermaux (2013). “Stretching, coalescence, and mixing in
827 porous media”. In: *Physical review letters* 110.20, p. 204501.
- 828 Le Borgne, T., T. R. Ginn, and M. Dentz (2014). “Impact of fluid deformation on mixing-induced
829 chemical reactions in heterogeneous flows”. In: *Geophysical Research Letters* 41.22, pp. 7898–
830 7906.
- 831 Le Borgne, T., M. Dentz, and E. Villiermaux (2015). “The lamellar description of mixing in
832 porous media”. In:
- 833 Le Borgne, T., P. D. Huck, M. Dentz, and E. Villiermaux (2017). “Scalar gradients in stirred
834 mixtures and the deconstruction of random fields”. In:
- 835 Li, L., C. I. Steefel, and L. Yang (2008). “Scale dependence of mineral dissolution rates within
836 single pores and fractures”. In: *Geochimica et Cosmochimica Acta* 72.2, pp. 360–377.
- 837 Li, L., K. Maher, A. Navarre-Sitchler, J. Druhan, C. Meile, C. Lawrence, J. Moore, J. Perdrial,
838 P. Sullivan, and A. e. a. Thompson (2017). “Expanding the role of reactive transport models
839 in critical zone processes”. In: *Earth-science reviews* 165, pp. 280–301.
- 840 Llewellyn, G. T., F. Dorman, J. L. Westland, D. Yoxtheimer, P. Grieve, T. Sowers, E. Humston-
841 Fulmer, and S. L. Brantley (2015). “Evaluating a groundwater supply contamination incident
842 attributed to Marcellus Shale gas development”. In: *Proceedings of the National Academy of*
843 *Sciences* 112.20, pp. 6325–6330.
- 844 Magesan, G. N., C. D. A. McLay, and V. V. Lal (1998). “Nitrate leaching from a free-draining
845 volcanic soil irrigated with municipal sewage effluent in New Zealand”. In: *Agriculture, ecosys-*
846 *tems & environment* 70.2-3, pp. 181–187.
- 847 Maher, K. (2011). “The role of fluid residence time and topographic scales in determining chem-
848 ical fluxes from landscapes”. In: *Earth and Planetary Science Letters* 312.1-2, pp. 48–58.
- 849 Maher, K. and C. P. Chamberlain (2014). “Hydrologic regulation of chemical weathering and
850 the geologic carbon cycle”. In: *Science* 343.6178, pp. 1502–1504.
- 851 Maher, K. and A. Navarre-Sitchler (2019). “Reactive transport processes that drive chemical
852 weathering: From making space for water to dismantling continents”. In: *Reviews in Miner-*
853 *alogy and Geochemistry* 85.1, pp. 349–380.
- 854 Maher, K. and K. U. Mayer (2019). “The art of reactive transport model building”. In: *Elements*
855 15.2, pp. 117–118.
- 856 Maher, K., C. I. Steefel, D. J. DePaolo, and B. E. Viani (2006). “The mineral dissolution rate
857 conundrum: Insights from reactive transport modeling of U isotopes and pore fluid chemistry
858 in marine sediments”. In: *Geochimica et Cosmochimica Acta* 70.2, pp. 337–363.
- 859 Malmström, M. E., G. Destouni, S. A. Banwart, and B. H. E. Strömberg (2000). “Resolving the
860 scale-dependence of mineral weathering rates”. In: *Environmental science & technology* 34.7,
861 pp. 1375–1378.
- 862 Malzone, J. M., C. S. Lowry, and A. S. Ward (2016). “Response of the hyporheic zone to transient
863 groundwater fluctuations on the annual and storm event time scales”. In: *Water Resources*
864 *Research* 52.7, pp. 5301–5321.

- 865 McKibben, M. A. and H. L. Barnes (1986). “Oxidation of pyrite in low temperature acidic solu-
866 tions: Rate laws and surface textures”. In: *Geochimica et Cosmochimica Acta* 50.7, pp. 1509–
867 1520.
- 868 Meile, C. and K. Tuncay (2006). “Scale dependence of reaction rates in porous media”. In:
869 *Advances in Water Resources* 29.1, pp. 62–71.
- 870 Molins, S., D. Trebotich, C. I. Steefel, and C. Shen (2012). “An investigation of the effect of
871 pore scale flow on average geochemical reaction rates using direct numerical simulation”. In:
872 *Water Resources Research* 48.3.
- 873 Molins, S., D. Trebotich, L. Yang, J. B. Ajo-Franklin, T. J. Ligoeki, C. Shen, and C. I. Steefel
874 (2014). “Pore-scale controls on calcite dissolution rates from flow-through laboratory and
875 numerical experiments”. In: *Environmental science & technology* 48.13, pp. 7453–7460.
- 876 Moussout, H., H. Ahlafi, M. Aazza, and H. Maghat (2018). “Critical of linear and nonlinear equa-
877 tions of pseudo-first order and pseudo-second order kinetic models”. In: *Karbala International*
878 *Journal of Modern Science* 4.2, pp. 244–254.
- 879 Murphy, S. F., R. B. McCleskey, D. A. Martin, J. H. Writer, and B. A. Ebel (2018). “Fire, flood,
880 and drought: extreme climate events alter flow paths and stream chemistry”. In: *Journal of*
881 *Geophysical Research: Biogeosciences* 123.8, pp. 2513–2526.
- 882 Navarre-Sitchler, A. and S. Brantley (2007). “Basalt weathering across scales”. In: *Earth and*
883 *Planetary Science Letters* 261.1-2, pp. 321–334.
- 884 Palandri, J. L. and Y. K. Kharaka (2004). *A compilation of rate parameters of water-mineral*
885 *interaction kinetics for application to geochemical modeling*. Tech. rep. Geological Survey
886 Menlo Park CA.
- 887 Panfilov, M. (2010). “Underground storage of hydrogen: in situ self-organisation and methane
888 generation”. In: *Transport in porous media* 85.3, pp. 841–865.
- 889 Perry, R. H., D. W. Green, and J. O. Maloney (1997). “Perry’s handbook of chemical engineer-
890 ing”. In: *Perry’s Handbook of Chemical Engineering*.
- 891 Plummer, L. N. and T. M. L. Wigley (1976). “The dissolution of calcite in CO₂-saturated solu-
892 tions at 25 C and 1 atmosphere total pressure”. In: *Geochimica et Cosmochimica Acta* 40.2,
893 pp. 191–202.
- 894 Pujades, E., S. Orban P. and Bodeux, P. Archambeau, S. Erpicum, and A. Dassargues (2017).
895 “Underground pumped storage hydropower plants using open pit mines: How do groundwater
896 exchanges influence the efficiency?” In: *Applied energy* 190, pp. 135–146.
- 897 Robati, D. (2013). “Pseudo-second-order kinetic equations for modeling adsorption systems for
898 removal of lead ions using multi-walled carbon nanotube”. In: *Journal of nanostructure in*
899 *Chemistry* 3.1, p. 55.
- 900 Rolle, M. and T. Le Borgne (2019). “Mixing and reactive fronts in the subsurface”. In: *Reviews*
901 *in Mineralogy and Geochemistry* 85.1, pp. 111–142.
- 902 Rudzinski, W. and W. Plazinski (2006). “Kinetics of solute adsorption at solid/solution interfaces:
903 a theoretical development of the empirical pseudo-first and pseudo-second order kinetic rate
904 equations, based on applying the statistical rate theory of interfacial transport”. In: *The*
905 *Journal of Physical Chemistry B* 110.33, pp. 16514–16525.
- 906 Salehikhoo, F., L. Li, and S. L. Brantley (2013). “Magnesite dissolution rates at different spatial
907 scales: The role of mineral spatial distribution and flow velocity”. In: *Geochimica et Cos-*
908 *mochimica Acta* 108, pp. 91–106.
- 909 Serrano, S. E. (2001). “Solute transport under non-linear sorption and decay”. In: *Water Research*
910 35.6, pp. 1525–1533.
- 911 — (2003). “Propagation of nonlinear reactive contaminants in porous media”. In: *Water Re-*
912 *sources Research* 39.8.

- 913 Skeel, R. D. and M. Berzins (1990). “A method for the spatial discretization of parabolic equa-
 914 tions in one space variable”. In: *SIAM journal on scientific and statistical computing* 11.1,
 915 pp. 1–32.
- 916 Song, X., J. Zhang, C. Zhan, Y. Xuan, M. Ye, and C. Xu (2015). “Global sensitivity analysis
 917 in hydrological modeling: Review of concepts, methods, theoretical framework, and applica-
 918 tions”. In: *Journal of hydrology* 523, pp. 739–757.
- 919 Soullaine, C., S. Roman, A. Kovscek, and H. A. Tchelepi (2017). “Mineral dissolution and
 920 wormholing from a pore-scale perspective”. In:
- 921 Steefel, C. I. and A. C. Lasaga (1994). “A coupled model for transport of multiple chemical
 922 species and kinetic precipitation/dissolution reactions with application to reactive flow in
 923 single phase hydrothermal systems”. In: *American Journal of science* 294.5, pp. 529–592.
- 924 Steefel, C., C. Appelo, B. Arora, D. Jacques, T. Kalbacher, O. Kolditz, V. Lagneau, P. Lichtner,
 925 K. U. Mayer, J. Meeussen, et al. (2015). “Reactive transport codes for subsurface environ-
 926 mental simulation”. In: *Computational Geosciences* 19.3, pp. 445–478.
- 927 Steefel, C. I., D. J. DePaolo, and P. C. Lichtner (2005). “Reactive transport modeling: An
 928 essential tool and a new research approach for the Earth sciences”. In: *Earth and Planetary
 929 Science Letters* 240.3-4, pp. 539–558.
- 930 Szulczewski, M. L., C. W. MacMinn, H. J. Herzog, and R. Juanes (2012). “Lifetime of carbon
 931 capture and storage as a climate-change mitigation technology”. In: *Proceedings of the
 932 National Academy of Sciences* 109.14, pp. 5185–5189.
- 933 Trauth, N. and J. H. Fleckenstein (2017). “Single discharge events increase reactive efficiency of
 934 the hyporheic zone”. In: *Water Resources Research* 53.1, pp. 779–798.
- 935 Urióstegui, S. H., R. K. Bibby, B. K. Esser, and J. F. Clark (2016). “Quantifying groundwater
 936 travel time near managed recharge operations using ^{35}S as an intrinsic tracer”. In: *Journal
 937 of Hydrology* 543, pp. 145–154.
- 938 Valocchi, A. J., D. Bolster, and C. J. Werth (2019). “Mixing-limited reactions in porous media”.
 939 In: *Transport in Porous Media* 130.1, pp. 157–182.
- 940 Van Cappellen, P. and J.-F. Gaillard (2018). “Biogeochemical dynamics in aquatic sediments”.
 941 In: *Reactive transport in porous media*, pp. 335–376.
- 942 Villiermaux, E. (2019). “Mixing versus stirring”. In: *Annual Review of Fluid Mechanics* 51,
 943 pp. 245–273.
- 944 Wang, L., H. Wen, and L. Li (2018). “Scale dependence of surface complexation capacity and
 945 rates in heterogeneous media”. In: *Science of The Total Environment* 635, pp. 1547–1555.
- 946 Weber J., W. J., P. M. McGinley, and L. E. Katz (1991). “Sorptions phenomena in subsurface
 947 systems: concepts, models and effects on contaminant fate and transport”. In: *Water research*
 948 25.5, pp. 499–528.
- 949 Wen, H. and L. Li (2017a). “An upscaled rate law for magnesite dissolution in heterogeneous
 950 porous media”. In: *Geochimica et Cosmochimica Acta* 210, pp. 289–305.
- 951 — (2017b). “An upscaled rate law for magnesite dissolution in heterogeneous porous media”.
 952 In: *Geochimica et Cosmochimica Acta* 210, pp. 289–305.
- 953 — (2018). “An upscaled rate law for mineral dissolution in heterogeneous media: The role of
 954 time and length scales”. In: *Geochimica et Cosmochimica Acta* 235, pp. 1–20.
- 955 White, A. F. and S. L. Brantley (2003). “The effect of time on the weathering of silicate minerals:
 956 why do weathering rates differ in the laboratory and field?” In: *Chemical Geology* 202.3-4,
 957 pp. 479–506.
- 958 Wu, F.-C., R.-L. Tseng, S.-C. Huang, and R.-S. Juang (2009). “Characteristics of pseudo-second-
 959 order kinetic model for liquid-phase adsorption: a mini-review”. In: *Chemical Engineering
 960 Journal* 151.1-3, pp. 1–9.

- 961 Xu, T., S. P. White, K. Pruess, and G. H. Brimhall (2000). “Modeling of pyrite oxidation in
962 saturated and unsaturated subsurface flow systems”. In: *Transport in porous media* 39.1,
963 pp. 25–56.
- 964 Yang, C., J. Samper, J. Molinero, and M. Bonilla (2007). “Modelling geochemical and microbial
965 consumption of dissolved oxygen after backfilling a high level radioactive waste repository”.
966 In: *Journal of Contaminant Hydrology* 93.1-4, pp. 130–148.

Journal Pre-proofs

Declaration of interests

The authors declare that they have no known competing financial interests or personal relationships that could have appeared to influence the work reported in this paper.

The authors declare the following financial interests/personal relationships which may be considered as potential competing interests:

Journal Pre-proofs